Detonation Shock Dynamics of Type Ia Supernovae

Scott David Dunkley

Submitted in accordance with the requirements for the degree of
Doctor of Philosophy

The University of Leeds
Department of Applied Mathematics
Department of Mechanical Engineering

August 2013

The candidate confirms that the work submitted is his own, except where work which has formed part of jointly authored publications has been included. The contribution of the candidate and the other authors to this work has been explicitly indicated below. The candidate confirms that appropriate credit has been given within the thesis where reference has been made to the work of others.

- Chapter 2, section 2.4 features graphs and similar text published in a jointly authored paper by Scott D. Dunkley, Gary J. Sharpe and Sam A. E. G. Falle titled 'Detonation Shock Dynamics of Type Ia Supernova', published by the Monthly Notices of the Royal Astronomical Society, 413 in 2013. Chapter 4 features the results which have also been published in this paper. The work was undertaken and written by Scott D. Dunkley under the supervision and aid of Gary J. Sharpe and Sam A. E. G. Falle.

Acknowledgements

I would like to thank my supervisors Gary Sharpe and Sam Falle. Their patience and assistance in allowing me to complete this thesis is greatly appreciated. I would also like to thank Caroline Handley and Alex Hodgson at A.W.E. for useful questions, discussion and help. This work was funded by A.W.E.

Abstract

The wavefront propagation of curved detonation waves in carbon-oxygen cores and helium shells of type Ia supernova progenitors may be predicted via a Detonation Shock Dynamics (DSD) approach. DSD is used typically in engineering to model explosives. A level set implementation is used to evolve the front, using intrinsic quasi-steady, quasi-one-dimensional detonation speed-curvature relationships. The effects of curvature are analysed for a number of models from the literature which originally use the local planar detonation speed, and compared. The differences can be very profound in the low density regions where detonation models are exploited to produce intermediate mass elements. In detonable low density regions, the detonation wave speed tends to be much lower than the planar DSD analysis predicts, while the subsonic driving zone controlling the dynamics is many order of magnitude shorter than its planar version. However, the lower shock temperatures ensure that the complete reaction lengths are orders of magnitude longer when curvature effects are properly accounted. Furthermore, the material cannot be detonated in sufficiently low density regions due to a curvature induced extinction limit. The implications for and need to reassess the nucleosynthesis, intermediate mass element production and even the progenitors of SN Ia detonation models, is discussed.

In the second part of this thesis, an adapted method for evolving the front when the speed function has a curvature component is introduced. A stationary boundary value problem is adapted by considering the non-stationary form. This method is similar in its implementation to the level set form but is more efficient. Its efficiency and error is investigated and compared to the level set method.

Contents

List of Figures

List of Tables

Nomenclature

Abbreviations

CJ - Chapman-Jouget

C-O - Carbon-oxygen

DDT - Detonation to deflagration transition

DSD - Detonation shock dynamics

ENO - Essentially non-oscillatory

FMM - Fast marching method

SN Ia - Type Ia supernova

SNe Ia - Type Ia supernovae

ZND - Zeldovich-von Neumann-Doering

Units

$M_\odot$ - Solar mass ($= 1.99 \times 10^{33}$ g)

Chapter 1

Introduction

1.1 Overview

Supernovae and novae have been viewed by humans for hundreds of years. They were known as 'guest stars' due to their relatively short appearance, after which they were never seen again. The past century has lead to a large increase in the number of discoveries due to improved observational techniques. However, it became clear that not all these events were of the same type. Baade and Zwicky (1934) noted a difference between nova (termed common nova) and giant nova, calling the latter supernovae. They believed supernovae to originate from a star transitioning to an object of lesser mass, later proposed by Zwicky (1938) to be a neutron star. An additional proposal was that supernovae be used as distance indicators due to their uniformity in maximum luminosity and post maximum spectra (Zwicky 1939). The visual magnitude of their light can be used to calculate the distance from them.

Supernovae are classified by their optical spectra near maximum light. Minkowski (1940) observed that a supernova in the barred spiral galaxy NGC 4725 had a different spectrum to other supernovae seen before. Although the absorption and emission bands were not clear, he suspected there to be hydrogen lines present. This led to two classifications of supernovae: type I supernovae which have no Balmer lines of hydrogen present near maximum light and type II which do (Minkowski 1941). Furthermore type I can be subdivided into type Ia, type Ib and type Ic (Wheeler and Harkness 1990). Type Ia have intermediate mass elements (silicon group) after maximum light and heavy (iron group) elements in their late time spectra and are the brightest of the three types. Type Ib have helium lines in their maximum light

spectra and oxygen lines in their late time spectra instead of iron, whereas type Ic are similar to type Ib, but with no helium lines.

Type II supernovae are believed to arise from the gravitational collapse of large ($M \geq 8\ M_{\odot}$, where $M_{\odot}$ is the solar mass unit) non-degenerate cores due to nuclear fusion being unable to counteract gravity (Hoyle and Fowler 1960), which leaving behind a neutron star. Cores are degenerate when they can not be compressed any further (without collapsing), due to the lowest electron energy levels being filled. Type Ib and Ic also arise from the core collapse of large stars, but these ones have shed their hydrogen shells and in the case of type Ic, their helium shells as well (Wheeler and Harkness 1990). Hoyle and Fowler (1960) discovered that type Ia are the result of thermonuclear burning from the fusion of nuclear fuel leading to an explosion in an electron-degenerate core. It is possible the star may be completely disrupted in contrast to Zwicky's (1938) earlier proposal of turning into a neutron star. It is now accepted that type Ia arise from thermonuclear disruption of a white dwarf in a binary system. This can be either a carbon and oxygen (C-O) core close to the Chandrasekhar mass (1.4 $M_{\odot}$) or a low mass ($M < 1.4\ M_{\odot}$) C-O core surrounded by helium known as a sub-Chandrasekhar mass model (e.g. Fink et al. 2010, Nomoto 1982b, Woosley and Weaver 1994). The Chandrasekhar mass is the maximum mass a white dwarf may be, in order to remain stable. Above this, the star collapses under its own gravity.

Type Ia supernovae (SNe Ia) are important in their roles as distance indicators and observations of this type have been used to show that the universe is expanding. Riess et al. (1998) used observations of SNe Ia to update and reduce the uncertainties in the Hubble constant, the deceleration parameter and many other values related to the universe. Supernovae research is a vast field including pre-supernova evolution, the location of the ignition point, the ignition process and the mechanism of wave propagation. The two mechanisms for burning are detonations (Fickett and Davis 1979) or deflagrations. A detonation propagates supersonically, whereas a deflagration propagates subsonically. Both have their agreements and disagreements with observations. Delayed detonations have been proposed to take the advantages of both mechanisms and eliminate their disagreements. In this case, the wave begins as a deflagration then at some time later turns into a detonation. This chapter will discuss the merits of these three mechanisms, how they compare with observations as well as discussing some of the events leading up to the explosion and the observational constraints,

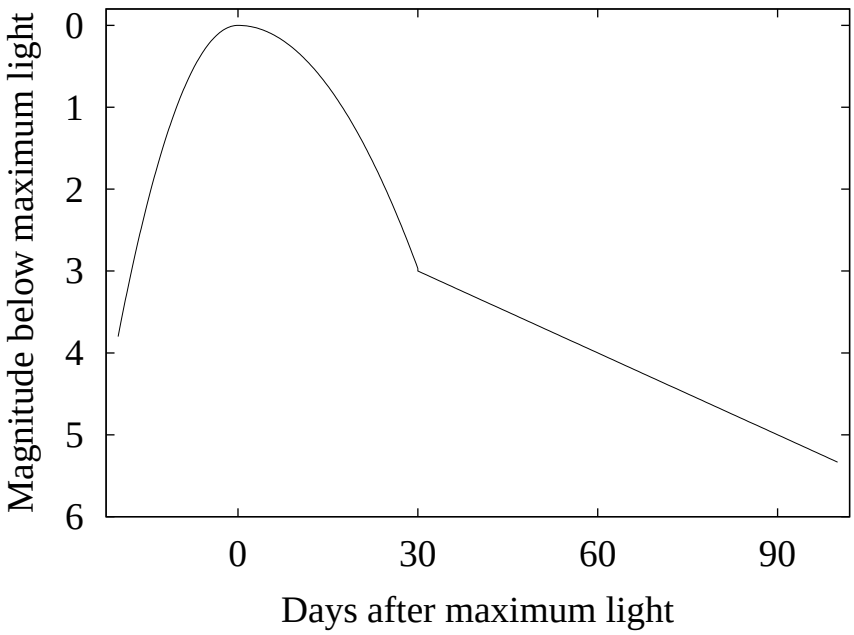

Figure 1.1: A typical light curve for SNe Ia. Wavelengths corresponding to intermediate mass elements are observed at maximum light (the peak). As these outer layers expand and become transparent, eventually the heavier elements near the centre of the star can be observed.

which any proposed model must satisfy.

1.2 Observational Constraints

Figure 1.1 shows a typical light curve for a SN Ia. Maximum light can be reached relatively quickly. Riess et al. (1999) find it takes approximately 20 days for a typical supernova of this type to reach maximum light. Type Ia supernovae have no hydrogen lines in their spectra which classifies them as type I and have silicon lines in their spectra at maximum light which further classifies them as Ia (Wheeler and Harkness 1990). There are also other intermediate mass elements such as calcium, magnesium, sulphur, oxygen and silicon at maximum light, which indicate these elements are present in the outer layers of the ejecta (Filippenko 1997). Although not usually present in the ejecta, recently it has been discovered there may even be unburned carbon (Folatelli et al. 2012). After maximum light has been reached, there is then a decline taking approximately one month as the outer layers expand and become transparent, then the tail falls off exponentially at one magnitude per month (Riess et al. 1999). The light observed here is from the heavier elements created near the centre of the star during the explosion. The light curve is powered by the energy (photons) released due

to ^{56}Ni as it radioactively β-decays to ^{56}Fe via ^{56}Ni $\rightarrow^{56}$ Co $\rightarrow^{56}$ Fe (Colgate and McKee 1969). Approximately 0.4 to 0.9 $M_\odot$ of ^{56}Ni needs to be produced in a model to agree with the observed light curves, although there are more luminous events such as SN 1991T synthesising 1 $M_\odot$ and sub-luminous events such as SN 1991bg producing 0.1 $M_\odot$ (Stritzinger et al. 2006). The different lines in the spectra have varying associated expansion velocities of the ejecta up to 22 000 km s^{-1}, which decrease with time (Garavini et al. 2007). Intermediate mass elements can have velocities greater than 18 000 km s^{-1} (Stehle et al. 2005).

1.3 Evolution

Nuclear reactions inside the core of a star generate heat by fusing hydrogen into helium, releasing energy. This period of a star's life is known as its main sequence stage. The star is in hydrostatic equilibrium as pressure from this heat, which flows outwards through radiation and convection, counteracts the gravitational force which could collapse the star. The larger a star is, the shorter its main sequence lifespan due to the greater comsumption rate of the hydrogen fuel. When this fuel is used up in the core, where thermonuclear fusion happens, the pressure falls and the core contracts due to gravity, ending its main sequence stage. Energy is released from the contraction of the core and heats up the shell, allowing the hydrogen here to continue fusing to produce helium. The initial mass of the star determines how long the core can keep contracting and when electron degeneracy prevents any further contractions taking place. Stars with an initial mass less than 0.2 $M_\odot$ do not go onto the next stage and will become helium white dwarfs. This is because low mass stars are fully convective and mix the helium throughout the star, not amassing an inert core of helium (Laughlin, Bodenheimer and Adams 1997). For stars with a greater mass, the helium in the core is compressed due to the core's gravity. Helium is produced faster in this shell than in a main sequence star of equivalent mass, increasing its luminosity and temperature. Consequently, the star expands, increasing its surface area. The effect of a larger surface area is stronger than the increase in luminosity and the effective temperature decreases. These larger stars are known as a red giant, due its light being shifted towards the red end of the visible spectrum. The hydrogen in the shell continues to burn to helium, which is absorbed into the core, shrinking it further as the gravitational force increases. Initial masses between approximately 0.2 and 0.5 $M_\odot$

can not initiate fusion in the helium core and eventually become helium white dwarfs as well (Laughlin, Bodenheimer and Adams 1997). Stars with a mass between 0.5 and 8 $M_\odot$ can experience helium fusion in their core. The continuing contractions of these larger stars can heat the core up to approximately 10^8 K. Carbon is produced from three helium-4 nuclei in what is known as the triple-alpha process. When carbon is present, this allows alpha processes to occur. Carbon and helium nuclei fuse together to create oxygen and thus the core now consists of carbon and oxygen. Stars below a mass of 8 $M_\odot$ will never be able to heat up their carbon and oxygen cores and eventually they eject their outer layers, becoming a C-O white dwarf if the remaining mass is less than the Chandrasekhar limit (1.4 $M_\odot$). High mass stars (greater than 8 $M_\odot$) can continue a sequence of fusing lighter elements to heavier ones with the aid of further core contractions. Such stars have an onion-like structure with hydrogen at its outermost layers and heavier elements towards the centre. Iron is eventually formed at the centre and since an iron core will absorb energy, fusion stops. The star is unable to counteract gravity, even with a degenerate core, and it collapses, giving rise to a supernova (e.g. type II) and eventually the formation of a neutron star or black hole.

The average mass of new C-O white dwarfs is approximately 0.6 $M_\odot$ (Kepler et al. 2007). This favours SNe Ia occurring in binary systems as the white dwarf can accrete matter from its companion to approach the Chandrasekhar limit and explode, or ignite when helium forms around it. The larger of the two stars becomes a white dwarf first. When the smaller of the two eventually becomes a red giant, the outer matter consisting of hydrogen can be transferred to the white dwarf. Stars have an area of gravitational influence known as its Roche lobe. A red giant's expansion can cause matter outside of this region to escape. The hydrogen surrounding the white dwarf will fuse to create helium.

Other origins for SNe Ia have been suggested, including the merging of oxygen and neon white dwarfs (Tutukov and Yungel'son 1992) or two C-O white dwarfs (Webbink 1984). This explains why no hydrogen is present. Two merging white dwarfs would also explain how they increase their mass. SNe Ia are however uniform in their observations and the variability in the parameters of the problem such as two different masses merging, angular momentum etc., implies the results should not be as uniform. It is possible that two merging C-O white dwarfs may not give rise to SNe Ia and will collapse instead (Nomoto and Iben 1985). More recent observations of the closest type Ia supernova in 25 years (at the time of observation) have

confirmed they can originate from a thermonuclear explosion of a C-O white dwarf, although the companion star was in the main sequence stage (Nugent et al. 2011). It is evident that there is no single path to producing SNe Ia, however the debate about the evolution path is beyond the scope of this thesis. The discussion will be focused on the general consensus model - that of a binary system.

1.4 Ignition

The temperature of the core rises due to compression as its mass continues to increase towards the Chandrasekhar limit. Degeneracy pressure is not affected by an increase in temperature and therefore the star can not expand to cool. Neutrino emission arising from plasmon decay balances the increasing heat, thus avoiding an explosion. The neutrinos can leave the star without interacting with the surrounding atoms, and carry away the heat. When the central density is approximately 2×10^9 g cm^{-3}, the rate of neutrino emission drops (Woosley and Weaver 1986). The neutrino emission is no longer sufficient to take away the heat and a thermonuclear runaway starts. A convective period with the hot material rising to the edge of the core for approximately 1000 years then takes place with the timescale for thermonuclear burning dropping as the core temperatures increases (Hillebrandt and Niemeyer 2000).

Paczyński (1972) was the first to argue that the Urca processes in convective cores would temporarily stabilise the runaway and delay an explosion. The Urca process works to remove heat from near the centre of the core. An electron is captured by a nucleus and then is carried outwards to the edge of the star via convection. A beta decay then occurs, releasing the electron which gives out energy near the edge. A neutrino is also emitted, carrying away further energy. Eventually the timescale for thermonuclear burning is equal to the timescale for convective turnover (the time taken for material to rise from the bottom of a convective cell to the top) when the temperature is 7×10^8 K (Woosley and Weaver 1986). When the temperature has risen to 1.5×10^9 K, the convective process is now too slow in comparison and carbon and oxygen are effectively burning in place (Hillebrandt and Niemeyer 2000). A reaction zone forms between the burned and unburnt material and a flame appears.

Where this flame originates is a subject of much debate. The evolution beforehand of the thermonuclear runaway can determine the flame's shape and where it starts. Burning blobs

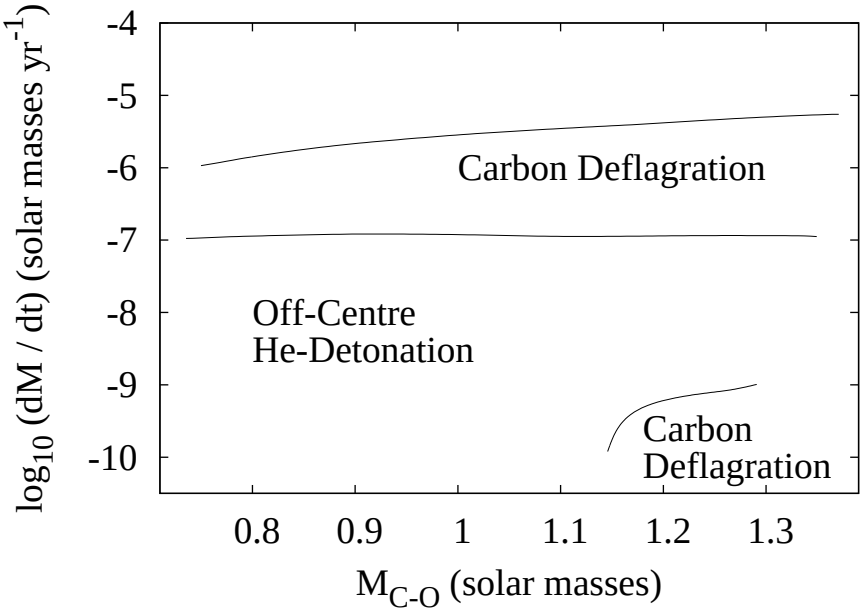

Figure 1.2: Triggering mechanism as a function of the accretion rate (dM/dt) and initial core mass ($M_{\mathrm{C-O}}$)(Nomoto 1982a).

may float and move far out from the centre of the core before becoming a flame (Garcia-Senz and Woosley 1995). High resolution three-dimensional simulations show that an off-centre ignition point is favoured in a range of 40-75 km (and even more probable nearer 50 km) from the centre if ignition takes place in the core (Nonaka et al. 2012). The nature of the flame is also a vast area of research. It may proceed as a deflagration, a detonation or a combination of both (delayed detonations), as will be discussed below.

1.5 Explosion Types

The main explosion types are deflagrations, detonations and delayed detonations. Deflagrations travel subsonically, whereas detonations travel supersonically with respect to the material ahead (Fickett and Davis 1979). Typically these usually refer to chemical reaction-driven processes, but in the case of SNe Ia, the reactions are nuclear driven. The type of explosion and where it occurs depends upon the C-O core mass and accretion rate of matter from a companion (figure 1.2, Nomoto 1982a). Slow and intermediate accretion rates lead to an off-centre helium detonation, whilst slow and rapid accretion rates lead to a carbon deflagration. Intermediate accretion rates for an off-centre helium detonation can produce a

'double' detonation, where the detonation also propagates through the C-O core and disrupts the entire star (Nomoto 1982b). When the accretion rate is slow, the important parameter is the initial mass of the core. Each type has its own advantages and disadvantages in agreeing with the observational constraints (section 1.2). These are next reviewed and discussed.

1.5.1 Deflagrations

Deflagrations are subsonic waves. A deflagration sends a shock ahead of it. When this shock reaches the surface of the star, it is reflected as a rarefaction wave, which expands and cools the outer regions of a star. A well known example of a one-dimensional 'fast' deflagration model is the W7 by Nomoto, Thielemann and Yokoi (1984). They choose a flame speed based on time-dependent mixing-length theory of convection which results in an explosion energy of approximately 10^{51} ergs s^{-1}. The deflagration eventually reaches 30% of the sound speed. The W7 model's spectra and light curves agree well with that of observed SNe Ia. The authors remark however that there is an overproduction of neutron-rich iron group elements in the centre. Using faster flame speeds increases this overproduction further as there is less time for the expanding outer matter to cool (Jeffery and Sutherland 1985). Khokhlov, Mueller and Hoeflich (1993) have based the flame speed directly on the sound speed with a value of 30%. However, they find the velocity range of the intermediate mass elements in the ejecta too low to agree with observations (approximately 1000 km s^{-1}) and attribute their disagreement with the W7 model to Nomoto's implicit numerical scheme with large time steps. If the flame speed is too low ('slow' deflagrations) then sufficient energy is not released (Nomoto, Sugimoto and Neo 1976).

In two dimensional models, the flame speed remains too low and to overcome this, Niemeyer and Woosley (1997) suggest multipoint ignition and active turbulent combustion. A multi-point ignition would increase the energy release. Thermal expansion in active turbulent combustion would cause the flame to feed back onto itself, thus creating more turbulence. Niemeyer and Woosley's (1997) suggestion contrasts with the more recent research of Nonaka et al. (2012), whose high resolution three-dimensional simulations show a single-point ignition is more likely. More energy is released in three-dimensional simulations compared to two-dimensions as the flame surface area has more instabilities from the extra degree of freedom (Roepke, Woosley and Hillebrandt 2007). Khokhlov (1995) investigated a three-

dimensional model and found that the star remains gravitationally bound and concluded that slow deflagrations would not cause SNe Ia explosions and that 'delayed detonation' scenarios are more likely. This conclusion is supported further by Gamezo et al. (2003) who also performed numerical simulations of three-dimensional models. They find material near the centre of the star is unburnt or partially burnt (intermediate mass elements). Such material according to observation is found in the outer layers of SNe Ia. They comment that a detonation arising from a deflagration would resolve this discrepancy. Indeed, from three-dimensional simulations of deflagrations, even a 'best-choice pure deflagration model' has its problems and a detonation is needed at a later time (Roepke et al. 2007).

The problem with deflagrations besides the flame travelling too slowly (to give the observed speeds and energy, although this is better in three-dimensions) is the question of the physics explaining the flame speed. Assuming a laminar flame speed seems unrealistic as instabilities can increase the flame speed. Acceleration of the flame can arise from the Rayleigh-Taylor instability (Sharp 1984) due to the density contrast between the hot buoyant burnt matter and cold fuel. Burning bubbles which resemble mushrooms in shape rise into the fuel. The flame interacts with turbulent eddies and becomes more wrinkled and torn, increasing its surface area and accelerating it. The turbulence can follow Kolmogorov-scaling (the smallest scales) at a late time during the deflagration which requires high resolution to simulate due to the small scales involved (Ciaraldi-Schoolman et al. 2009).

1.5.2 Detonations

The first hydrodynamic simulation of a white dwarf was by Arnett (1969) in one-dimension, who assumed detonation as the burning mode. He found expansion velocities up to 20 000 km s^{-1} and a significant amount of ^{56}Ni produced. While this satisfies the criteria that the model produces enough ^{56}Ni, pure detonation models of Chandrasekhar mass white dwarfs fail to satisfy the other criteria of high-velocity intermediate mass elements in the outer layers. At the densities involved, the detonation burns the C-O completely to iron group elements. The density needs to be less than about 10^7 g cm^{-3} for a detonation to begin producing intermediate mass elements, as then the length of the detonation reaction zone becomes comparable to the size of the star (Khokhlov 1989).

This is exploited in low density sub-Chandrasekhar mass detonation models. These models

may be the cause of SNe Ia more often than their Chandrasekhar mass counterparts (Ruiter, Belczynski and Fryer 2009). These models do not reach the Chandrasekhar mass and thus the core can not ignite by itself. Nomoto (1982b) investigated three models and found that two of them produce double detonation waves for intermediate accretion rates (4×10^{-8} $M_\odot$ yr^{-1} $\geq dM/dt \geq 10^{-9}$ $M_\odot$ yr^{-1}) with small amounts of intermediate mass elements. A detonation is produced in the helium which can drive a shock into the core providing the accretion rate is high enough, igniting the core and disrupting the star. Carbon ignition can also happen when the shock converges at the core centre (Woosley and Weaver 1994). Spherical symmetry however seems unlikely due to the presence of a companion causing asymmetry. The nuclear reaction rates are very sensitive to temperature and density. Nomoto's (1982b) models were examined by Wiggins and Falle (1997) in two dimensions as a detonation starting at one point. The faster He detonation was found to overtake the slower C-O detonation leading to the formation of cusps. Similar scenarios have been investigated in two dimensions with the C-O detonation occurring off-centre (Livne and Glasner 1991; Fink et al. 2010). Benz (1997) investigated such a scenario in three dimensions and found that core ignition was only missed by less than 15% for all but one case. The core detonated for the highest resolution. The nuclear reactions are very sensitive to temperature and density, which means that even small differences in the maximum temperatures due to different numerical resolutions can be significant. Sub-Chandrasekhar models are not without their disadvantages like other models, and can predict high-velocity Ni and He in their outer ejecta instead of intermediate mass elements at maximum light and are also too blue (Nugent et al. 1997). Even so, Sim et al. (2010) find these models give good agreement with observations despite having light curves that fade too quickly after maximum light. This can be attributed to uncertainties in the radiative transfer simulations (used to obtain light curves from models) and improving this aspect can lead to better agreement for sub-Chandrasekhar mass models.

1.5.3 Delayed Detonations

A detonation can also form from an accelerating flame known as a deflagration-detonation transition (DDT, Lee 1977). Khokhlov (1991) applied this idea to supernovae in a delayed detonation model and found intermediate mass element production and high velocities in good agreement with observations. A deflagration wave starts near the centre of the core

and propagates outwards, decreasing the density due to expansion. This deflagration wave then undergoes a DDT some time later at a lower density where the detonation reaction zone length can be comparable to the size of the star. Roepke, Woosley and Hillebrandt (2007) find that although detonations may occur in two dimensional simulations, three dimensional models fail to detonate. This is due to the models being asymmetrical and therefore less of a focusing effect arising from collision of material. They find a detonation will only occur for fuel temperatures greater than approximately 1.9×10^9 K and densities greater than 10^7 g cm^{-3}, but concede their investigation of the parameter space is incomplete and the collision region requires higher resolution. Therefore they do not rule out detonations completely.

A pulsational delayed detonation is a variant on the delayed detonation model. The flame is quenched during the expansion and fails to unbind the star (Arnett and Livne 1994a). A detonation then starts due to compressional heating as it contracts during a pulse (Arnett and Livne 1994b). This would increase the density of the star as well. There is a large amount of intermediate mass element production but little Ni production (Hoeflich and Khokhlov 1996). Plewa (2007) considers a slightly different scenario where a deflagration fails and then regions form which ignite as detonations due to a shock-to-detonation transition.

The disadvantage of the delayed detonation scenario is a lack in the understanding of the physics where the DDT happens in white dwarfs (and the earlier problem of flame-turbulence interactions). Similar to deflagrations where the flame speed is a free parameter chosen to give good agreement with observations, here the density at which the DDT happens is the parameter. Woosley (2007) explained this through a semi-analytic representation. He lists some criteria that must be satisfied in order for a deflagration to transition to a detonation. The first is that the carbon and oxygen burning flames must be separate spatially. If this is not the case, the burnt material is too hot and the fuel-burnt material mixture is too combustible. The burning region is then too narrow and the flame can not broaden which would lead to a detonation. Secondly, the largest turbulent eddies must be near the sound speed. They must not be too subsonic as it is the energy of these eddies which helps the detonation form. Finally, the fuel and burnt material mixture must be as large as the largest eddies, i.e. the flame width is at the integral length scale. The detonation will form most likely where several flames merge. These criteria may be satisfied for densities in the range of $(0.5 - 1.5) \times 10^7$ g cm^{-3}, which interestingly is the density chosen to give good agreement in

artificially parameterised models. Piro and Chang (2008) suggest it could be to do with the end of the convective region in the core. Below a density of $3 \times 10^7 - 1 \times 10^8$ g cm^{-3} , the star is 'quiet' with no turbulence there at the end of its convective stage just before ignition.

1.6 Summary

Detonations, deflagrations and delayed detonations have been discussed and the advantages and disadvantages of each mentioned. Detonations, whilst giving good agreement with respect to the expansion velocities, produce little intermediate mass elements. This problem has progressed towards a solution in some way with that of double detonation and sub-Chandrasekhar models. These however have their associated problems. Conversely, deflagrations have lower expansion velocities and greater production of intermediate mass elements. Even then, with a flame speed too high (or low), too much Ni is produced (or the star is bound). Combining both detonations and deflagrations into the delayed detonation model seems to give the best results. Even then however, there is uncertainty as to how the DDT occurs. Wheeler and Harkness (1990) in their summary of SNe Ia remark how a 'dampened-detonation' model may be the solution to the problems of both pure detonations and deflagrations. Considering the effects of curvature is one way a detonation may be 'dampened' (Sharpe 2001) but these have yet to be applied to models.

Whether the model is one, two or three dimensional plays an important role. The results can be different for more realistic two and three dimensional models. In the case of deflagrations, the flame speeds are still too low (although better agreement), even in two or more dimensions. Treating the explosion as asymmetric instead of spherically symmetric can lead to cusps forming due to the density-dependent speed differences, affecting the nucleosynthesis for detonations (Wiggins and Falle 1997). These higher dimensions, however, will result in increased computational times. This can be avoided by decreasing the resolution. However, this can affect the results. This may be the difference between a core detonating and not due to the sensitivity of nuclear reactions (Benz 1997).

A nuclear network describes the creation or destruction of nuclei. This involves a system of coupled ODES (Arnett 1996). Benz (1997) discusses the requirement of a reduced nuclear network. Usually this is not a problem as the majority of the computational time is spent

dealing with the hydrodynamics. Having high burning rates however, means the time steps become small and then a large amount of time is spent using the equation of state and updating the temperature. A reduced nuclear network, which saves computational effort is sufficient for correct reproduction of energy generation if one is not interested in detailed chemical compositions to obtain light curves and spectra.

The problem is highly multiscale in nature, adding to the computational complexity. Detonations in SNe Ia consists of a carbon, oxygen and silicon burning stage (Khokhlov 1989; Sharpe 1999). The length of this carbon burning stage can be less than 1 cm whereas a typical white dwarf radius is over 10^8 cm. It is not feasible to resolve such scales computationally. This is acceptable when one assumes that the detonation propagates at the planar speed and shock jump conditions can be applied. However, the dynamics and wave structure are nonlinearly coupled for detonations which are pathological, curved or have time-dependence in the reaction zone. Therefore one must fully resolve the driving part of the reaction zone to compute the solution (Aslam, Bdzil and Hill 1998; Bdzil and Stewart 2007; Sharpe and Braithwraite 2005). In the context of SNe Ia, curvature effects, especially at lower densities, can affect the speed and burning (Sharpe 2001). The driving zone determines the dynamics and if this occurs on scales which are small compared to the grid spacing, then a subgrid model is needed to resolve the behaviour.

Attempts have been made at such subgrid modelling of SNe Ia detonations by assuming that the detonation propagates at the planar detonation speed which depends only on the local density ahead of the wave. The literature in this chapter assumes planar detonation propagation. Wiggins and Falle (1997) have investigated Nomoto's (1982b) double detonation models in two dimensions using the method of geometrical optics. However, the planar speed assumption is only consistent with the steady planar limit. This requires the reactions to complete to generate the energy required to drive the front at planar speeds. Hence this assumption must break down for the low density regions where detonations can produce intermediate mass elements via incomplete silicon burning.

Similar issues to those described above arise in engineering applications of so-called non-ideal explosives, which has led to the development of a set of subgrid models known collectively as Detonation Shock Dynamics (DSD) (Stewart 1998; Bdzil and Stewart 2007). DSD allows one to pre-compute the wave dynamics taking into account the effect of wavefront curvature.

Using a suitable front tracking method, one can then investigate the effects of curvature in a detonation (as a function of its density and curvature since the speed has been pre-computed). Level set methods (Sethian 1999) have been applied to detonations using DSD (Aslam, Bdzil and Stewart 1996). Sharpe (2001) has pre-computed the detonation speeds as a function of density and curvature for SNe Ia for a reduced nuclear network. Despite the profound effect of curvature at low densities, currently no attempt has been made to apply DSD to SNe Ia. Fink et al. (2010) present some preliminary results of a novel, but ad-hoc, iterative method for taking into account incomplete burning. Townsley et al. (2009) employ a simple three-stage nuclear reaction mechanism. Even with such a reduced mechanism, a subgrid model will still be required for the first and second reactions (carbon and oxygen burning respectively) due to the disparity in length scales with the star size. Furthermore, such reduced models may have quite different curved detonation dynamics than predicted by detailed nuclear reaction models.

The purpose of this thesis is to develop and apply DSD subgrid models for computing detonation in full star SN Ia simulations using detonation speed - curvature relationships for a range of densities in C-O and He. Firstly, the relevant theory behind detonations is discussed for planar and curved detonations. A simple example of how one obtains a detonation speed - curvature relation is shown. This theory is then discussed in the context of SNe Ia. A suitable front tracking method is explained and relevant test problems used for validation. The DSD predictions are compared to those assuming planar detonation speeds for a number of detonation models and the implication of the nucleosynthesis discussed. This thesis is not concerned with the ignition problem, whether the explosion is a detonation or deflagration, nor where the DDT happens. While valid questions, these are research areas in their own right. However, the effects of this research on these areas will be discussed where appropriate. The second part of this thesis introduces a new method for front tracking with curvature-dependent speeds based on the stationary formulation of level set methods.

Chapter 2

Detonations

2.1 Introduction

In this chapter the relevant theory behind both planar and curved detonations is explained. There is then an example to demonstrate how one can compute the detonation speed - curvature curves for the ideal gas equation. Finally planar and curved detonations are discussed in the context of SNe Ia.

A detonation wave propagates at supersonic velocities with respect to the (unburnt) fuel ahead. Most of the energy is transferred by mass flow in strong compression waves. The detonation front compresses and heats matter, initiating reactions (chemical reactions in explosives, nuclear reactions in supernovae) that support the wave. The equations that represent a detonation are the Euler equations with the addition of an equation describing the progress of the reaction with a reaction rate. One can perform a direct numerical simulation (DNS) to obtain the evolving wave front. The dynamics of the front may be determined by structures which are smaller than the grid spacing. This results in the DNS being not well resolved and inaccurate. A subgrid model is therefore required.

DSD is a subgrid theory to describe a detonation wave with small curvature (Bdzil and Stewart 2007). The speed is given by

$$D_n = D_{\text{planar}} - \alpha(\kappa), \tag{2.1}$$

where D_n is the local detonation velocity in the shock normal direction, n, D_{planar} is the planar detonation velocity, κ is the curvature and $\alpha(\kappa)$ is a property of the material. This

is known as a detonation speed - curvature ($D_n - \kappa$) relation or curve. Using the equations that represent curved detonations, a 'master equation' can be derived, relating the curvature of the front and the heat released (Yao and Stewart 1998; Bdzil and Stewart 2007). When the correct D_n and κ are chosen, the master equation has a solution. This is checked by integrating the flow behind the detonation front. If the incorrect D_n or κ is chosen, then an incorrect solution to the master equation is obtained at some point in the flow. Each point on the $D_n - \kappa$ curve represents a 'snapshot' of the flow speed and curvature. One does not need to resolve the details of the flow in later calculations as this is taken into account through correctly solving the master equation. The following flow and front dynamics are decoupled. All that is required is an appropriate front tracking algorithm for the evolving detonation front according to the $D_n - \kappa$ curve or curves.

2.2 Detonation Theory

2.2.1 ZND Theory

The Zeldovich-von Neumann-Doering (ZND) model of detonation theory is based on the Euler equations of hydrodynamics in a reactive medium. Transport effects (diffusion, heat conduction, radiation and viscosity) are neglected. Local thermodynamic equilibrium of all thermodynamic variables is assumed apart from the chemical (or nuclear) composition. A reaction zone follows the detonation front. The equations (from Fickett and Davis 1979) are

$$\frac{D\rho}{Dt} + \rho\nabla\cdot\mathbf{u} = 0, \tag{2.2}$$

$$\rho\frac{D\mathbf{u}}{Dt} + \nabla\cdot p = 0, \tag{2.3}$$

$$\frac{De}{Dt} + p\frac{D\rho^{-1}}{Dt} = 0, \tag{2.4}$$

where e is the internal energy per unit mass, p is the pressure, ρ is the density and $\mathbf{u}$ is the fluid velocity. The progress of the reaction is governed by

$$\frac{D\lambda}{Dt} = W(p,\rho,\lambda), \tag{2.5}$$

where λ is the reaction progress variable and W is the reaction rate, and the material derivative is given by

$$\frac{D}{Dt} \equiv \frac{\partial}{\partial t} + \mathbf{u} \cdot \nabla. \tag{2.6}$$

The theory assumes the flow is planar, one-dimensional, in a frame moving with a shock, and is steady, i.e. no time dependence. The transformation is $u_n = u - D_n$, where u_n is the velocity in the shock frame, u the velocity in the laboratory frame and D_n is the detonation front velocity. The coordinate in the shock frame is x_n. Equations 2.2 to 2.5 are Galilean invariant and therefore in the shock frame are unchanged in form. Removing time derivatives (as steady), dropping the n subscript on all variables, and as the partial derivatives become ordinary derivatives, the equations become

$$\begin{aligned} u\frac{d\rho}{dx} + \rho\frac{du}{dx} &= 0, & (2.7)\\ u\frac{du}{dx} + \frac{1}{\rho}\frac{dp}{dx} &= 0, & (2.8)\\ \frac{de}{dx} - \frac{p}{\rho^2}\frac{d\rho}{dx} &= 0, & (2.9)\\ u\frac{d\lambda}{dx} &= W(p, \rho, \lambda). & (2.10) \end{aligned}$$

The first equation is $d(\rho u)/dx = 0$. Integrating this gives $\rho u =$ constant. This constant is simply $\rho_0 u_0$ ahead of the shock, where the zero subscripts refers to conditions ahead of the shock. This gives the conservation of mass as

$$\rho u = \rho_0 D_n. \tag{2.11}$$

Multiplying the first equation by ρ, then as ρu is a constant from the above equation, this can be integrated. Using the initial conditions gives the constant on the right hand side as $p_0 + \rho_0 D_n^2$. Thus the conservation of momentum is

$$p + \rho u^2 = p_0 + \rho_0 D_n^2. \tag{2.12}$$

Adding the second equation to the third gives $d(e + p/\rho + u^2/2)/dx = 0$. Similarly as be-

fore, integrating and using the initial conditions gives the conservation of energy (Bernoulli's equation) as

$$e + \frac{p}{\rho} + \frac{u^2}{2} = e_0 + \frac{p_0}{\rho_0} + \frac{D_n^2}{2}. \tag{2.13}$$

Equation 2.11 can be used in equation 2.12 to eliminate u to give

$$R = (\rho_0 D_n)^2 - (p - p_0)/(v_0 - v) = 0 \tag{2.14}$$

where v represents the specific volume $v = \rho^{-1}$, and R is the Rayleigh line representing conservation of momentum. A Rayleigh line is a straight line passing through the points (v_0, p_0) with slope $-(\rho_0 D_n)^2$. Eliminating both D_n and u from equation (2.13) leads to

$$H = e(p, v, \lambda) - e(p_0, v_0, \lambda_0) - 0.5(p + p_0)(v_0 - v) = 0, \tag{2.15}$$

where H is the Hugoniot curve representing conservation of energy. These equations, H and R, along with the conservation of mass, are valid throughout the structure for no curvature.

Figure 2.1 shows the Hugoniot curves for unburnt ($\lambda = 0$, H_0) and completely burnt ($\lambda = 1$, H_1) material. Between these two curves there are partial reaction Hugoniot curves for $0 < \lambda < 1$. The reaction starts immediately behind the shock (the von Neumann spike), where the unburnt Hugoniot curve and a Rayleigh line intersect. The reaction proceeds down the Rayleigh line until the completely burnt Hugoniot curve is reached. Two possible Rayleigh lines are shown, one of which is tangent to the H_1 curve and the other intersecting at two points. A Rayleigh line which does not intersect the H_1 curve is unphysical due to not satisfying the conservation conditions. When the detonation speed is such that the Rayleigh curve is tangent to H_1 (labelled O), the detonation is known as a Chapman-Jouget (CJ) detonation. This value of the detonation speed represents the minimum possible self-sustaining speed. There are two types of sound speed. The equilibrium sound speed, c_e, which is the speed of low-frequency acoustic waves and only relevant if the reactions are in equilibrium. The other is the speed of high-frequency waves, known as the frozen sound speed, c_f. The chemical composition can be assumed to be frozen as the waves are travelling fast. The equilibrium sound speed is less than the frozen sound speed. The flow at the end of the reaction zone for a CJ detonation is equilibrium sonic ($c_e^2 - u^2 = 0$ in the shock

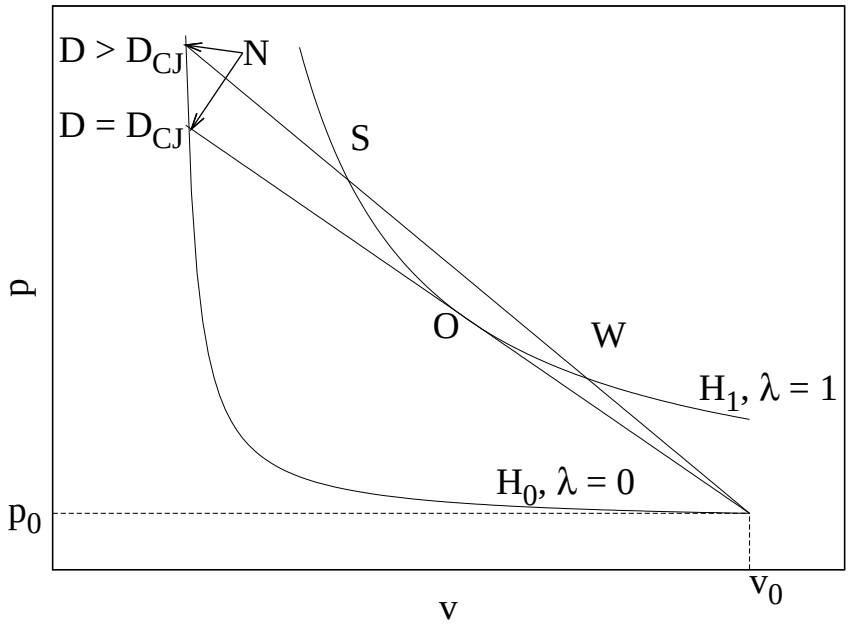

Figure 2.1: Hugoniot curves and possible Rayleigh lines for a detonation. The pressure is p and v is the specific volume. The unburnt Hugoniot, H_0 is in the unburnt state ($\lambda = 0$) with initial pressure p_0 and initial specific volume v_0. Immediately at the detonation, the state jumps to the von Neumann spike, N. S represents the strong intersection and W the weak intersection for a Rayleigh line where the detonation velocity, D, is greater than the CJ velocity, D_{CJ}, with the completely burnt ($\lambda = 1$, H_1) Hugoniot. When the detonation velocity is at D_{CJ}, the Rayleigh line is tangent to H_1 at point O.

frame). When the detonation speed is greater than this there are two possible intersections, strong (labelled S) and weak (labelled W). The flow behind the detonation front for a strong intersection is subsonic ($c_f^2 - u^2 > 0$ in the shock frame) and there is a greater increase in pressure and density than in a weak detonation. A disturbance behind the front can overtake it. If the reactions are all exothermic then there is no path to the weak intersection. When endothermic or dissipative effects are present, the partial reaction Hugoniot curves can cross and it is possible for the weak intersection to be reached. Behind a weak detonation, the flow is supersonic ($c_f^2 - u^2 < 0$ in the shock frame) and a disturbance can not overtake the front. A detonation in this case is of the pathological (e.g. mole decrement) or eigenvalue (e.g. second reaction endothermic such as Si burning in SNe Ia) type. There is a unique value of the detonation speed which allows this and depends upon the rate function, unlike the CJ case, where the final state only depends on the equation of state.

2.3 Curved Detonations

Unlike the planar detonations of ZND theory, spherically expanding waves will have curvature of the front. The effect of curvature is similar to that of endothermic reactions in that they both have an internal frozen sonic point. Although the reaction may still be exothermic throughout. Consequently, the detonation speed is also a unique solution of the eigenvalue problem. However, unlike the previous case where the detonation speed is greater than the CJ speed, here the detonation speed is lower since the sonic point lies within the reaction zone and some of the heat is released behind the sonic point. Temperatures are lower due to the lower speeds (shock strength) and the reaction rates are also lower. This leads to the overall length of the reaction zone increasing. Behind the sonic point, due to the region being supersonic, reactions can not influence anything upstream, including the front. This means there is an effective reaction zone length between the front and sonic point which controls the front dynamics. As the curvature increases, the sonic point moves further into the reaction zone and more of the energy is released behind it, causing the detonation velocity to decrease.

2.3.0.1 $D_n - \kappa$ relations

Stewart and Yao (1998) investigated simple irreversible one reaction systems with the planar detonation being CJ and showed that a $D_n - \kappa$ relation generally has a 'Z' shape (figure 2.2). The curve has two turning points, one associated with extinction of the detonation when the curvature becomes too great (labelled extinction) and the other due to ignition of a shock as the front becomes flat (labelled ignition). The curve consists of an upper, middle and lower branch. The speed of the shock on the lower branch is travelling close to the sound speed and is hence non-reactive. The middle branch is unstable as the detonation speed accelerates as the curvature increases and there is no path to it from either branch. The quasi-one dimensional approximation also breaks down on the middle branch due to the length of the reaction zone between the shock and the sonic point which can affect the front becoming comparable to the radius of curvature (Sharpe 2000a). This middle branch is therefore not relevant to detonation propagation. Building on this, Sharpe investigated curvature effects for detonations where the planar detonation is of the pathological type with two consecutive reactions (Sharpe 2000a) and one reversible reaction (Sharpe 2000b). Qualitatively these were

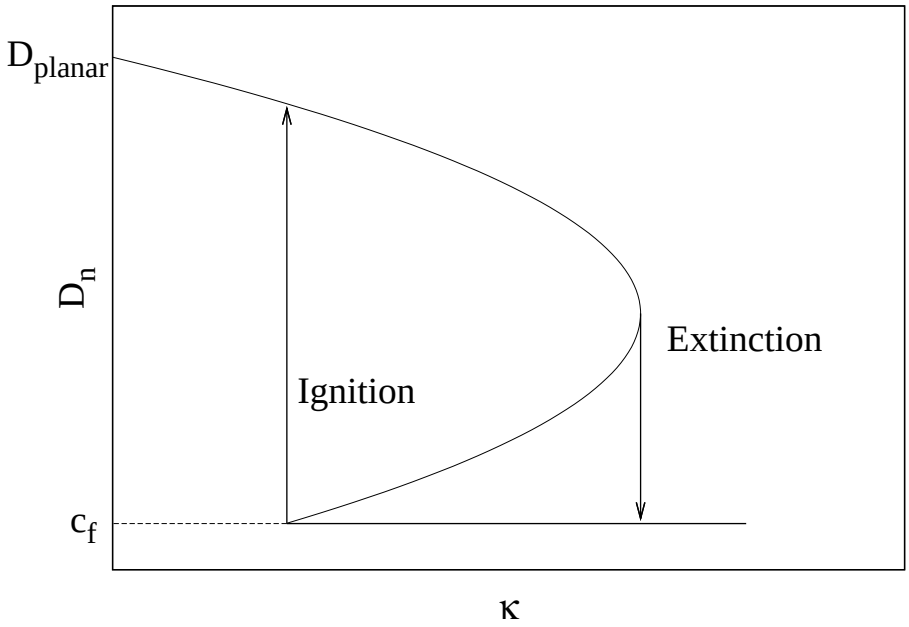

Figure 2.2: A typical $D_n - \kappa$ relation. As the curvature, κ, increases, the detonation speed, D_n, drops, until an extinction point is reached. The speed then jumps to the frozen sound speed, c_f. If the shock is initially inert, as the curvature decreases, a point is reached where the shock ignites.

found to be the same as one-reaction systems where the planar wave is CJ.

Realistically, the transition between branches as the wave evolves would not be a jump, i.e. these transitions occur over a finite time scale. However, the existence of the branch extinction and transitions are due to extreme sensitivity of induction times on the shock speed (and hence shock temperature), such that these transitions usually occur via self-accelerating shock-reaction zone coupling or decoupling effects and hence tend to be rapid. As a first approximation it is therefore reasonable to treat the transitions between solution branches as instantaneous on the time scales of interest.

The quasi-one-dimensional equations for when weak curvature to $O(\kappa)$ is taken into account and transverse variations taken to be zero in the frame of the shock are

$$\frac{d(\rho u)}{dx} = -j\rho\frac{(u+D_n)}{R_s}\,, \tag{2.16}$$

$$u\frac{du}{dx} + \frac{1}{\rho}\frac{dp}{dx} = 0\,, \tag{2.17}$$

$$\frac{de}{dx} - \frac{p}{\rho^2}\frac{d\rho}{dx} = 0\,, \tag{2.18}$$

$$u\frac{d\lambda}{dx} = W, \tag{2.19}$$

where $j = 0$, 1 or 2 for planar, cylindrical and spherical geometry respectively (Yao and Stewart 1996). The curvature is given by $\kappa = j/R_s$. To see why the first equation has the extra term, consider the conservation of mass equation in cylindrical geometry, in the laboratory frame, which is

$$\frac{\partial\rho}{\partial t} + \frac{1}{x_l}\frac{\partial(x_l\rho u_l)}{\partial x_l} = 0, \tag{2.20}$$

where the l subscript denotes variables in the laboratory frame. As $u = u_l - D_n$ and for a detonation front at R_s, $x_l = x + R_s$, and in a frame with the shock ($\partial/\partial t = \partial/\partial t - D_n\partial/\partial x$) time derivatives can be disregarded, then

$$\frac{d(\rho u)}{dx} = -\frac{\rho(u+D_n)}{x+R_s}, \tag{2.21}$$

or

$$\frac{d(\rho u)}{dx} = -\frac{\rho(u+D_n)}{R_s\left(\frac{x}{R_s}+1\right)}. \tag{2.22}$$

If $R_s \gg x$ then the above simplifies to equation 2.16 with $j = 1$. Similarly, the conservation of mass equation in spherical geometry is

$$\frac{\partial\rho}{\partial t} + \frac{1}{x_l^2}\frac{\partial(\rho x_l^2 u_l)}{\partial x_l} = 0. \tag{2.23}$$

Using the equations for u_l and x_l and again disregarding time derivatives, this gives

$$\frac{d(\rho u)}{dx} = -\frac{2\rho(u+D_n)}{R_s(\frac{x}{R_s}+1)}, \tag{2.24}$$

which will similarly simplify to equation 2.16 with $j = 2$. Note if $\kappa = 0$ then these equations reduce to the equations of steady planar ZND detonation. These equations 2.16 to 2.19 can be reduced to two coupled ordinary differential equations for a specified equation of state. Taking equation 2.18, and as $e = e(\rho, p, \lambda)$, then using the chain rule

$$\frac{\partial e}{\partial \rho}\frac{d\rho}{dx} + \frac{\partial e}{\partial p}\frac{dp}{dx} + \frac{\partial e}{\partial \lambda}\frac{d\lambda}{dx} = \frac{p}{\rho^2}\frac{d\rho}{dx}. \tag{2.25}$$

Rearranging this gives

$$\frac{dp}{dx} = \frac{1}{\partial e/\partial p}\left[\left(\frac{p}{\rho^2} - \frac{\partial e}{\partial \rho}\right)\frac{d\rho}{dx} - \frac{\partial e}{\partial \lambda}\frac{d\lambda}{dx}\right]. \tag{2.26}$$

Using this in equation (2.17)

$$u\frac{du}{dx} + \frac{1}{\rho\partial e/\partial p}\left[\left(\frac{p}{\rho^2} - \frac{\partial e}{\partial \rho}\right)\frac{d\rho}{dx} - \frac{\partial e}{\partial \lambda}\frac{d\lambda}{dx}\right] = 0. \tag{2.27}$$

Equation 2.16 is used to eliminate $d\rho/dx$ and simplified, leading to

$$\left(u^2 - \frac{\frac{p}{\rho^2} - \frac{\partial e}{\partial \rho}}{\partial e/\partial p}\right)\frac{du}{dx} - \left(\frac{\frac{p}{\rho^2} - \frac{\partial e}{\partial \rho}}{\partial e/\partial p}\right)\frac{j(u + D_n)}{R_s} - \frac{u\frac{\partial e}{\partial \lambda}\frac{d\lambda}{dx}}{\rho\partial e/\partial p} = 0. \tag{2.28}$$

The adiabatic frozen sound speed is

$$c_f^2 = \left(\frac{\partial p}{\partial \rho}\right)_{s,\lambda}, \tag{2.29}$$

where s is the entropy. As

$$de = Tds + \frac{p}{\rho^2}d\rho, \tag{2.30}$$

and entropy is constant, then

$$\left(\frac{\partial e}{\partial \rho}\right)_{s,\lambda} d\rho + \left(\frac{\partial e}{\partial p}\right)_{s,\lambda} dp = \frac{p}{\rho^2}d\rho, \tag{2.31}$$

and rearranging this and using the adiabatic frozen sound speed definition gives

$$c_f^2 = \frac{\frac{p}{\rho^2} - \frac{\partial e}{\partial \rho}}{\partial e/\partial p}. \tag{2.32}$$

Equation 2.28 becomes

$$\frac{du}{dx} = \frac{\phi}{\eta}, \tag{2.33}$$

where

$$\eta = c_f^2 - u^2, \tag{2.34}$$

is the sonic parameter and

$$\phi = -c_f^2 j \frac{(u + D_n)}{R_s} - \frac{u \frac{\partial e}{\partial \lambda} \frac{d\lambda}{dx}}{\rho \partial e / \partial p}, \tag{2.35}$$

is the thermicity. The other ordinary differential equation with which this is coupled, is

$$\frac{d\lambda}{dx} = \frac{W}{u}. \tag{2.36}$$

There is a frozen sonic point ($\eta = 0$) located within the reaction zone of the detonation wave. Equation (2.33) can then only be satisfied if $\phi = 0$ at this point as well, otherwise the derivative diverges and the solution breaks down. These pair of conditions are known as the generalised CJ conditions. One can therefore choose a trial value of κ or D_n with the other fixed. If D_n (or κ) is too low then a frozen sonic point is reached with $\phi \neq 0$. If D_n (or κ) is too high then the flow is subsonic ($\eta > 0$) at the point where $\phi = 0$ is reached. This places limits on the upper and lower values of D_n (or κ) and bisection can be used to find the correct value to the desired accuracy.

2.3.0.2 $D_n - \kappa$ Relation for Ideal Gas

A simple example on how to obtain a $D_n - \kappa$ relation for an ideal gas is next shown. Yao and Stewart (1996) show how equations (2.16) to (2.19) can be reduced to two ordinary differential equations for an ideal gas equation of state given by

$$e = \frac{p}{(\gamma - 1)\rho} - Q\lambda\,, \tag{2.37}$$

where γ is the ratio of specific heats and Q is the heat release. An Arrhenius form reaction rate is used

$$W = k(1-\lambda)\exp[-E_A/(p/\rho)], \tag{2.38}$$

where k is a rate constant, E_A is the activation energy. The equations are dimensionless with

$$c_f^2 = \frac{\bar{c_f^2}}{\bar{D_{CJ}^2}}, \quad E_A = \frac{\bar{E_A}}{\bar{D_{CJ}^2}}, \quad k = \frac{\bar{k}\bar{l_{\frac{1}{2}}}}{\bar{D_{CJ}}}, \quad \kappa = \bar{\kappa}\bar{l_{\frac{1}{2}}}, \quad p = \frac{\bar{p}}{\bar{\rho_0}\bar{D_{CJ}^2}},$$

$$Q = \frac{\bar{Q}}{\bar{D_{CJ}^2}}, \quad \rho = \frac{\bar{\rho}}{\bar{\rho_0}}, \quad D_n = \frac{\bar{D_n}}{\bar{D_{CJ}}}, \quad u = \frac{\bar{u}}{\bar{D_{CJ}}}, \quad x = \frac{\bar{x}}{\bar{l_{\frac{1}{2}}}}, \tag{2.39}$$

where $\bar{l_{\frac{1}{2}}}$ is the steady planar half-reaction-zone length ($\lambda = \frac{1}{2}$) and a bar denotes a dimensional quantity. The form of equations (2.16) to (2.19) are unchanged. This gives the frozen sound speed as

$$c_f^2 = \frac{\gamma p}{\rho}. \tag{2.40}$$

Combining equations (2.17) and (2.18), integrating and simplifying gives Bernoulli's equation

$$\frac{\gamma p}{(\gamma-1)\rho} - Q\lambda + \frac{1}{2}u^2 = \frac{\gamma p_0}{(\gamma-1)} + \frac{1}{2}D_n^2. \tag{2.41}$$

Using equations (2.40) and (2.41), this gives a new expression for the sound speed

$$c_f^2 = \gamma p_0 + (\gamma-1)\left[\frac{(D_n^2-u^2)}{2} + Q\lambda\right]. \tag{2.42}$$

Equations (2.16) to (2.19) can then be reduced to two coupled ordinary differential equations

$$\frac{du}{dx} = \frac{\phi}{\eta}, \tag{2.43}$$

$$\frac{d\lambda}{dx} = \frac{k(1-\lambda)\exp(-\gamma E_A/c_f^2)}{u}, \tag{2.44}$$

where the thermicity, ϕ, is given by

$$\phi = kQ(1-\lambda)\exp(-\gamma E_A/c_f^2)(\gamma-1) - c_f^2\kappa(u+D_n), \tag{2.45}$$

and η is the sonic parameter given by equation 2.34.

To find k, a steady detonation travelling at the planar speed is considered. Conservasation of mass, momentum and energy are obtained by substituting and integrating equations 2.16 to 2.18 amongst themselves with $\kappa = 0$ and the initial conditions $\rho_0 = 1$ and $D_n = -1$, to give

$$\begin{aligned} \rho u &= -1, && (2.46)\\ p + \rho u^2 &= p_0 + 1, && (2.47)\\ \frac{\gamma p}{(\gamma-1)\rho} + \frac{1}{2}u^2 &= \frac{\gamma p_0}{\gamma - 1} + Q\lambda + \frac{1}{2}. && (2.48) \end{aligned}$$

The above equations allow ρ, p and λ to be written in terms of u,

$$\begin{aligned} \rho &= -\frac{1}{u}, && (2.49)\\ p &= p_0 + 1 + u, && (2.50)\\ \lambda &= -\frac{(u+1)\left[(\gamma+1)u + 2\gamma p_0 + \gamma - 1\right]}{2Q(\gamma-1)}, && (2.51) \end{aligned}$$

and thus

$$c_f^2 = -\gamma(p_0 + 1 + u)u. \quad (2.52)$$

The frozen sonic value of u_{sonic} is then

$$c_f^2 - u^2 = -\gamma(p_0 + 1 + u_{\text{sonic}})u_{\text{sonic}} - u_{\text{sonic}}^2 = 0, \quad (2.53)$$

which gives

$$u_{sonic} = \frac{-\gamma(p_0+1)}{\gamma+1}. \quad (2.54)$$

An alternative form to equation 2.51 is then

$$u = u_{sonic} \pm \frac{\sqrt{(1-\gamma p_0)^2 - 2Q(\gamma^2-1)\lambda}}{\gamma+1}. \tag{2.55}$$

The solution with the plus sign corresponds to a subsonic (strong) branch and the minus sign corresponds to a supersonic (weak) branch. A solution can only pass from one to the other at a frozen sonic point. A CJ detonation is frozen subsonic throughout ($u < c_f$ always). Therefore the relevant branch is always subsonic. Using equation 2.55 at the shock ($\lambda = 0$) gives

$$u_{\text{shock}} = \frac{1 - 2\gamma p_0 - \gamma}{\gamma+1}, \tag{2.56}$$

immediately behind the shock and $u_{\text{half reaction}}$ at $\lambda = \frac{1}{2}$ can also be found. As $\lambda = 1$ at the end of the reaction zone then using equations (2.51) and (2.54), this gives Q for a CJ detonation as

$$Q = \frac{(1-\gamma p_0)^2}{2(\gamma^2-1)}. \tag{2.57}$$

Using equation (2.43) with $\kappa = 0$ as planar gives

$$\frac{du}{dx} = \frac{kQ(1-\lambda)(\gamma-1)\exp(-\gamma E_A/c_f^2)}{c_f^2 - u^2}, \tag{2.58}$$

where c_f^2 is given by equation (2.52) and λ by equation (2.51). This gives k as

$$k = \int_{u_{\text{shock}}}^{u_{\text{half reaction}}} -\frac{c_f^2 - u^2}{Q(1-\lambda)(\gamma-1)} \exp(\gamma E_A/c_f^2) du, \tag{2.59}$$

which can be integrated numerically.

Following the bisection procedure outlined, D_n is fixed and then iteration to find κ is performed until the turning point. The values chosen are $p_0 = 0.02$ and 0.04, with $E_A = 0$, 0.25 and 0.5 for each. The results are shown in figure 2.3. When $E_A = 0$ there is no turning point and the curve continues until the frozen sound speed is almost reached. Using equation 2.40 this gives 0.15 and 0.21 for $p_0 = 0.02$ and 0.04 respectively. When E_A is increased, an extinction point appears. This extinction point decreases with increasing E_A. Increasing the pressure results in increasing the extinction curvature.

If one were interested in calculating a one-dimensional evolving detonation front for this example, then numerically solving $dR_s/dt = D_n(\kappa)$, where R_s is the shock radius, is straight

forward. The curvature of the shock can be calculated simply from $\kappa = j/R_s$ where j is the geometry of the problem (1 for circular, 2 for spherical). The detonation speed can then be found out by interpolation (e.g. linear) onto a $D_n - \kappa$ curve. If the density is variable, then a family of curves for various densities can be generated and $D_n = D_n(\kappa, \rho_0)$. Interpolation (e.g. bilinear) can be used on this surface. Higher dimensions require more sophisticated techniques and these will be discussed later.

2.4 Detonations in SNe Ia

In this section the relevant properties of detonations in the C-O core and He shells are discussed. The density profile for one of the models to be investigated is shown in figure 2.4. Detonation waves in C-O consist of a carbon burning stage (C) being the thinnest, an oxygen burning stage (O) and then a silicon burning stage (Si) which is the thickest. Initially carbon starts burning with itself, producing neon and helium nuclei (alpha particles) which can be expressed as ^{12}C(^{12}C,^{4}He)^{20}Ne, and protons and sodium, which can transform to magnesium, expressed as ^{12}C(^{12}C,p)^{23}Na(p,γ)^{24}Mg, where p is a proton and γ is a photon (Khokhlov 1989). Silicon begins to appear from the produced elements reacting with the free protons, neutrons and alpha particles. Oxygen starts to burn at a later time, and more silicon is produced. For silicon, the wave is pathological for densities greater than 2×10^7 g cm^{-3} due to endothermic burning (Khokhlov 1989; Sharpe 1999). The silicon then transforms relatively slowly to Ni. Helium burns mostly to Ni for densities $\geq 5 \times 10^6$ g cm^{-3} and for densities below, a thermally neutral relaxation layer follows the burning layer (Khokhlov 1989). The leading reaction is $3^4\text{He} \rightarrow {}^{12}\text{C}$. The molar fractions of intermediate elements produced during the burning of He to Ni is extremely small.

The results presented here employed an α-network for the nuclear reactions (α in this context is different from that in the $D_n - \kappa$ curve context), consisting of 13 species linked by 27 reactions with the reaction rates taken from Fryxell et al. (1989). A description of the equation of state is summarised from Timmes and Arnett (1999), who investigated five approximations to this equation in a range of scenarios such as a supernova, and a hydrogen gas cloud collapsing. There can be many calls to the equation of state routine where integrals need to be solved and roots computed, so approximations may be used to speed up the

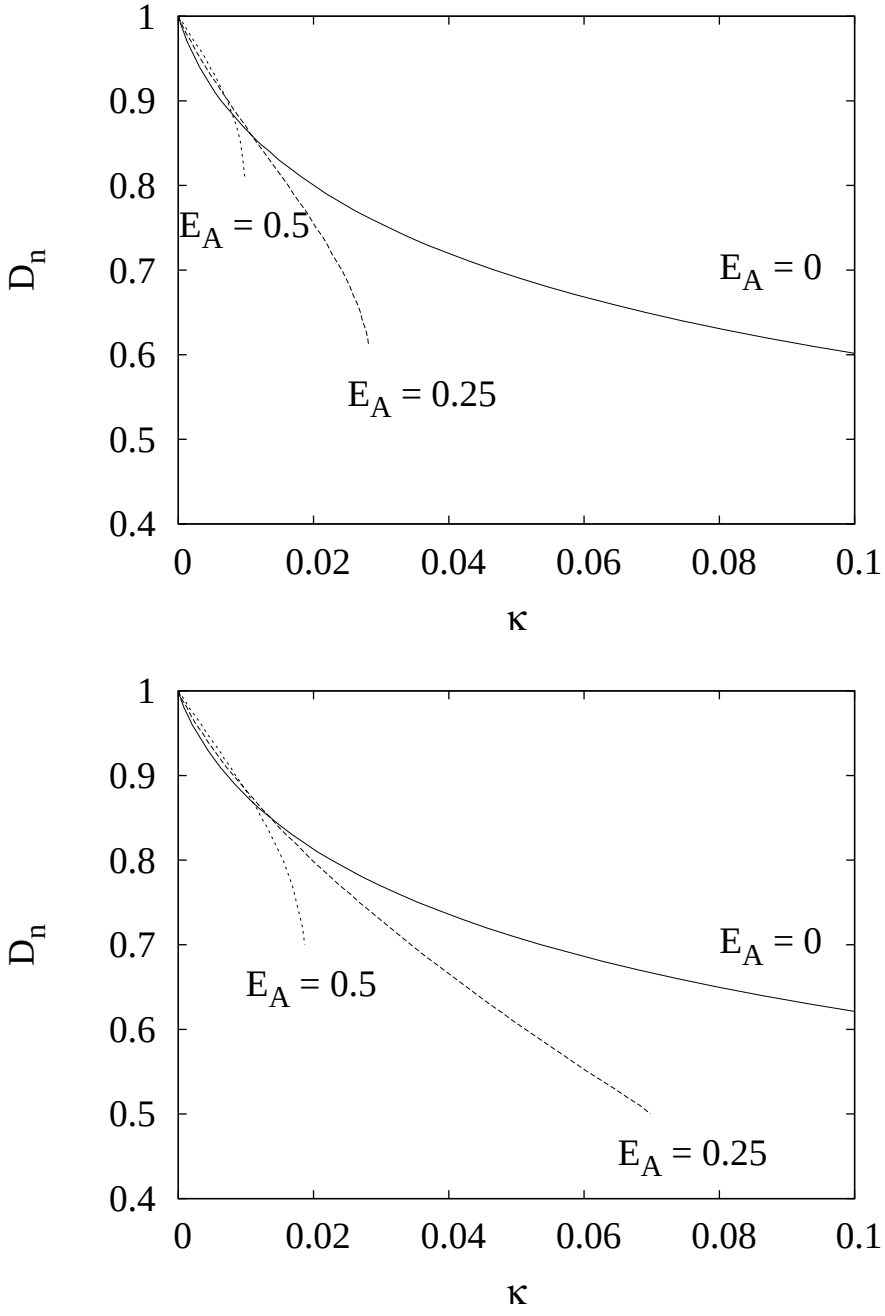

Figure 2.3: $D_n - \kappa$ curves for an ideal gas with $p_0 = 0.02$ (top) and 0.04 (bottom) for various activation energies as labelled.

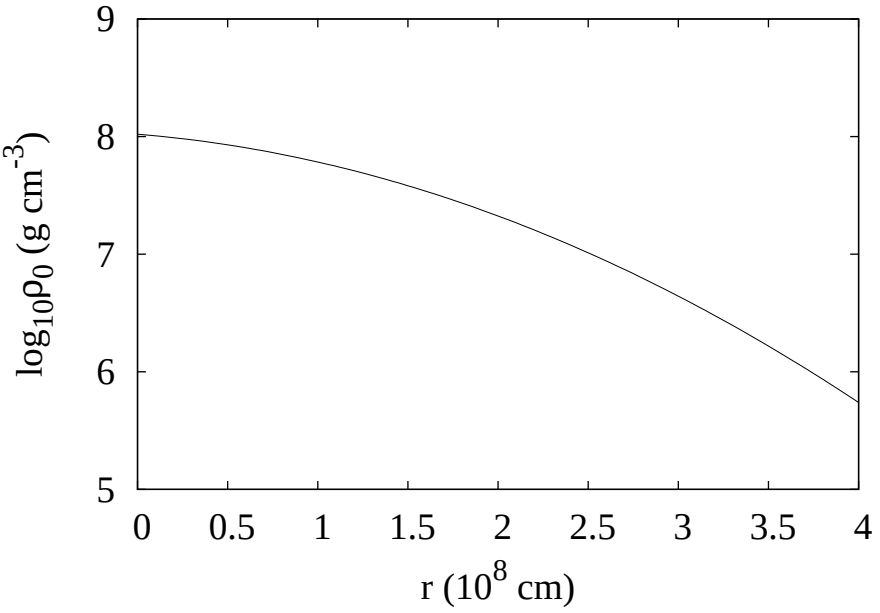

Figure 2.4: Density profile for Nomoto's (1982b) case A with a polynomial fitted by Wiggins (1993). The helium shell starts at $r = 3.136 \times 10^8$ cm ($\log_{10} \rho_0 = 6.53$ g cm^{-3}).

computation. The advantage here with DSD is the equation of state only needs to be used for the $D_n - \kappa$ curves and these can then be applied to models. The equation of state consists of contributions from radiation, non-degenerate ions and arbitrarily degenerate and relativistic electrons and electron-positron pairs. The pressure and equation of state is thus

$$p = p_{\rm radiation} + p_{\rm ions} + p_{\rm electrons} + p_{\rm positrons}, \tag{2.60}$$

$$e = e_{\rm radiation} + e_{\rm ions} + e_{\rm electrons} + e_{\rm positrons}. \tag{2.61}$$

The radiation terms arise from a blackbody in local thermodynamic equlibrium

$$p_{\rm radiation} = \frac{aT^4}{3}, \tag{2.62}$$

$$e_{\rm radiation} = \frac{3p_{\rm radiation}}{\rho}, \tag{2.63}$$

where $a = 4\sigma/c$, σ is the Stefan-Boltzmann constant (5.67×10^{-5} erg cm^{-2} s^{-1} K^{-4}) and c is the speed of light (3×10^{10} cm s^{-1}). The ions are non-degenerate and at a high temperature, thus their behaviour approximates an ideal gas . The ion terms are then

$$p_{\rm ions} = N_{\rm ions} kT, \tag{2.64}$$

$$e_{\rm ions} = \frac{3p_{\rm ions}}{2\rho}, \tag{2.65}$$

where $N_{\rm ions} = N_A/\bar{A}$ is the ion number density, k is Boltzmann's constant (1.38×10^{-16} erg K^{-1}), N_A is Avogadro's constant (6.02×10^{23} mol^{-1}) and $\bar{A}$ is the mean number of nucleons per isotope. The last two terms are from the consideration of a non-interacting Fermi gas. The expressions for these are

$$p_{\rm electrons} = \frac{16\pi\sqrt{2}}{3h^3} m_e^4 c^5 \beta^{5/2} \left[F_{3/2}(\eta,\beta) + \frac{1}{2}\beta F_{5/2}(\eta,\beta) \right], \tag{2.66}$$

$$p_{\rm positrons} = \frac{16\pi\sqrt{2}}{3h^3} m_e^4 c^5 \beta^{5/2} \left[F_{3/2}(-\eta-2/\beta,\beta) + \frac{1}{2}\beta F_{5/2}(-\eta-2/\beta,\beta) \right], \tag{2.67}$$

$$e_{\rm electrons} = \frac{8\pi\sqrt{2}}{\rho h^3} m_e^4 c^5 \beta^{5/2} \left[F_{3/2}(\eta,\beta) + \beta F_{5/2}(\eta,\beta) \right], \tag{2.68}$$

$$e_{\rm positrons} = \frac{8\pi\sqrt{2}}{\rho h} m_e^4 c^5 \beta^{5/2} \left[F_{3/2}(-\eta-2/\beta,\beta) + \beta F_{5/2}(-\eta-2/\beta,\beta) \right] + \frac{2 m_e c^2 N_{\rm positrons}}{\rho}, \tag{2.69}$$

where the number density of the positrons is given by

$$N_{\rm positrons} = \frac{8\pi\sqrt{2}}{h^3} m_e^3 c^3 \beta^{3/2} \left[F_{1/2}(-\eta-2/\beta,\beta) + \beta F_{3/2}(-\eta-2/\beta,\beta) \right], \tag{2.70}$$

h is Planck's constant (6.63×10^{-27} cm^2 g s^{-1}), m_e is the rest mass of an electron (9.11×10^{-28} g), $\beta = kT/(m_e c^2)$ is a relativity parameter, η is the normalised chemical potential energy for the electrons and $F_k(\eta,\beta)$ is the Fermi-Dirac integral given by

$$F_k(\eta,\beta) = \int_0^\infty \frac{x^k (1+0.5\beta x)^{1/2}}{\exp(x-\eta)+1} dx. \tag{2.71}$$

A temperature of 10^8 K and 50 per cent C and 50 per cent O composition for the core was assumed. Sharpe's (2001) results stop at the turning point of O burning and therefore the C burning stage was not presented. The results presented here include the C burning

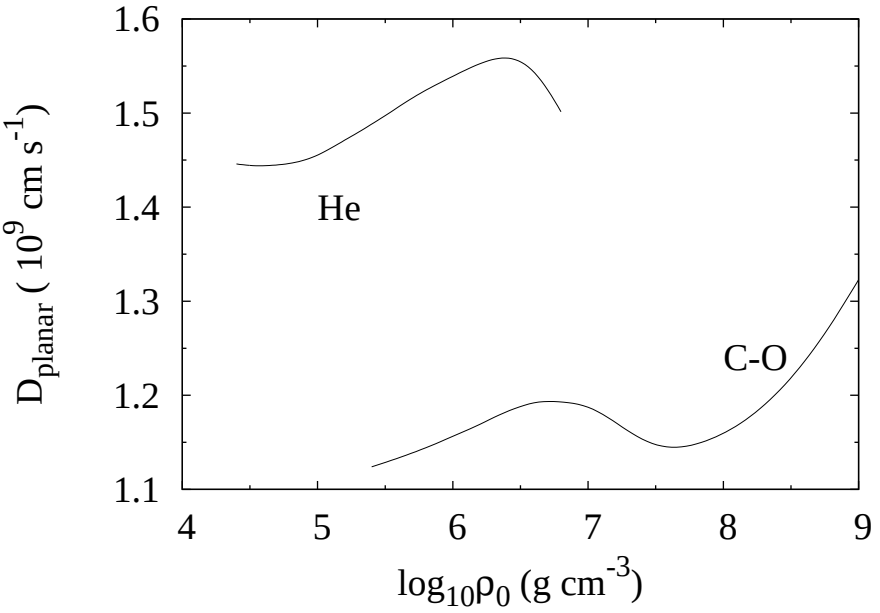

Figure 2.5: Speed for planar detonations as functions of initial density for C-O and He (Sharpe 2001).

stage. Sharpe computed the $D_n - \kappa$ curves in a similar way to the example for the ideal gas in the previous section. However, the equation of state here is more complex and the number of reactions is greater. The method is the same but the expressions for the thermicity, frozen sound speed and other values will vary due to the different physics. As before, the thermicity consists of a term proportional to the curvature, but also another term proportional to the rate of nuclear energy release.

Messoudi et al. (2007) used a full reaction network of 331 species with 3262 reactions and compared the curve they obtain for $\rho_0 = 5 \times 10^6$ g cm^{-3} with that of a 13 species and 18 reactions α-network. They find the full reaction network gives higher detonation velocities, greater Si residue and Ni production. Messoudi et al. (2007) also find the extinction curvature of the C branch an order of magnitude higher for this specific density. Although their reaction network is more complete, there will be a greater computational cost. However, while the choice of reaction network may quantitatively affect the predictions, it will be a minor effect compared to the very large qualitative difference between taking into account curvature compared to without.

2.4.1 Planar Detonations

The planar detonation speed, $D_{\rm planar}$, as a function of initial density (i.e. corresponding to the local density just ahead of the shock front) for both C-O and He can be seen in figure 2.5. For densities between 3×10^6 and 2×10^7 g cm^{-3}, the C-O detonation speed drops as Si burning produces less energy due to the equilibrium composition becoming enriched with light and intermediate mass elements (Gamezo et al. 1999). For higher densities, the wave is of the pathological type with endothermic Si burning taking place such that the sonic point is located at the end of O burning (Sharpe 1999). The planar detonation speed in He is higher than that in C-O.

The dependence of the reaction zone length scale, $l_{\rm planar}$, on initial density is shown for both species in figure 2.6. The C-O reaction zone length is longer than that in He for a given initial density. However, the length scales can be seen to increase by orders of magnitude as the density drops. The reaction zone length becomes comparable to the size of the star (10^8 cm) at $\rho_0 = 10^7$ g cm^{-3} and $\rho_0 = 6 \times 10^6$ g cm^{-3} for C-O and He respectively. For pathological C-O detonations at higher densities, the effective reaction lengths (distance between the sonic point and the shock) is shown and hence a rapid drop in length occurs at $\rho_o = 2 \times 10^7$ g cm^{-3} due to the jump in the sonic point position.

2.4.2 Curved Detonations

Figures 2.7 and 2.8 show the response of the detonation speed in the normal direction to curvature in C-O for a variety of initial densities. The dashed line represents the full solution curves of the quasi-one-dimensional, quasi-steady equations (Sharpe 2001). However, only the stable branches with negative slope are physically relevant and hence the solid lines show the evolutionary path corresponding to an expanding detonation front. For high densities the detonation speed does not drop very much with increasing curvature (e.g. only by ~ 3 per cent for a density of 10^9 g cm^{-3}, figure 2.7 top) before the extinction curvature is reached (corresponding to a turning point in the $D_n - \kappa$ curves). As discussed previously, at these densities the planar ($\kappa = 0$) wave is pathological and the sonic point remains near the end of O burning up to extinction. For the low initial densities of interest here, the $D_n - \kappa$ curves are multi-branched (e.g. figures 2.7 bottom and 2.8, corresponding to densities of 10^7 and 10^6 g cm^{-3} respectively). The high speed branch (labelled Si in figures 2.7 and 2.8) corresponds

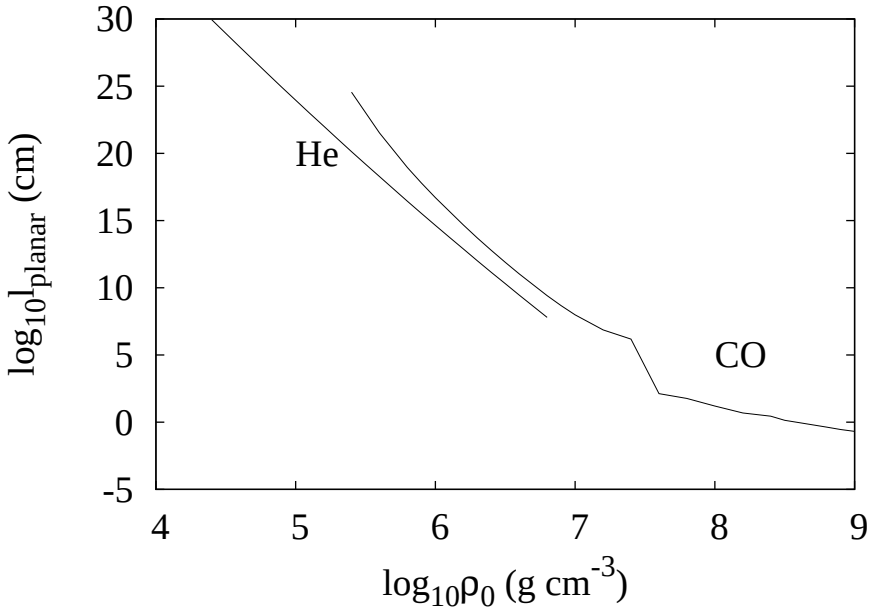

Figure 2.6: Distance between shock and the sonic point for planar detonations as functions of initial density for C-O and He (Sharpe 2001).

to very weakly curved (near planar) detonation propagation with the sonic point occurring near the end of Si burning, the middle branch (labelled O) corresponds to detonation driven only by C and O burning and the low speed branch corresponds to the subsonic driving zone consisting only of the C burning stage. Each of these branches may have its own extinction point, beyond which the solution switches to the next branch. Only when the extinction of the low speed branch is reached, does the curvature induce complete detonation failure. Thus in low densities, detonation speeds much lower than the CJ value can be sustained.

The effective reaction zone length (distance between the shock and frozen sonic point) l, in a C-O detonation as a function of curvature for the three initial densities 10^6, 10^7 and 10^9 g cm^{-3} are shown in figures 2.9 and 2.10. The effective reaction length generally decreases with increasing curvature as the frozen sonic point moves further towards the front. The effective reaction length increases slightly near turning points. This is because the change in the detonation speed is large compared to the change in curvature. The drop in detonation speed results in longer reaction length scales due to lower temperatures and reaction rates, whereas the curvature reduces it due to moving the frozen sonic point. It is the former which dominates close to a turning point. The jump in the location of the frozen sonic point between the branches with increasing curvature results in the driving zone reaction lengths

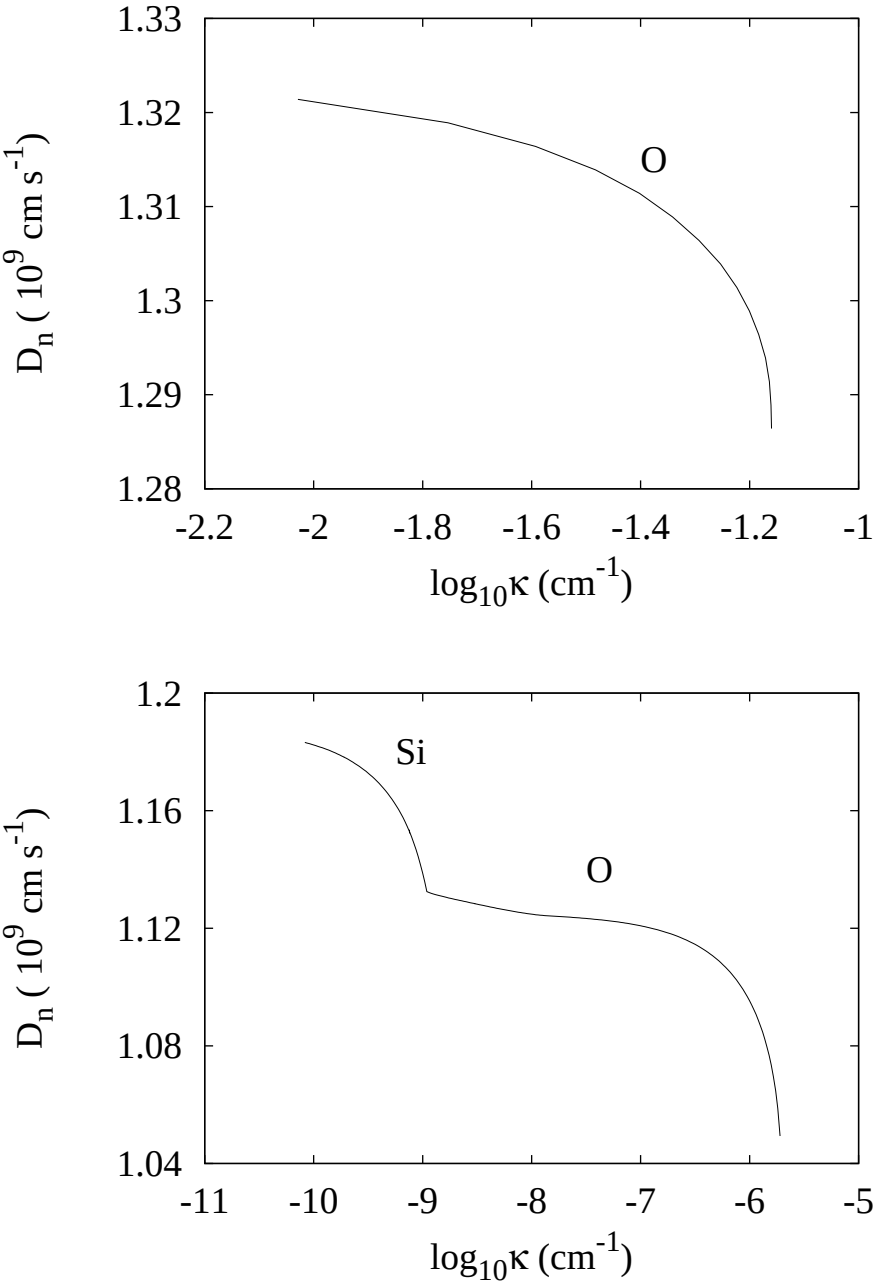

Figure 2.7: $D_n - \kappa$ curves for curved C-O detonations and initial C-O densities 10^9 (top) and (bottom) 10^7 g cm^{-3} (Sharpe 2001).

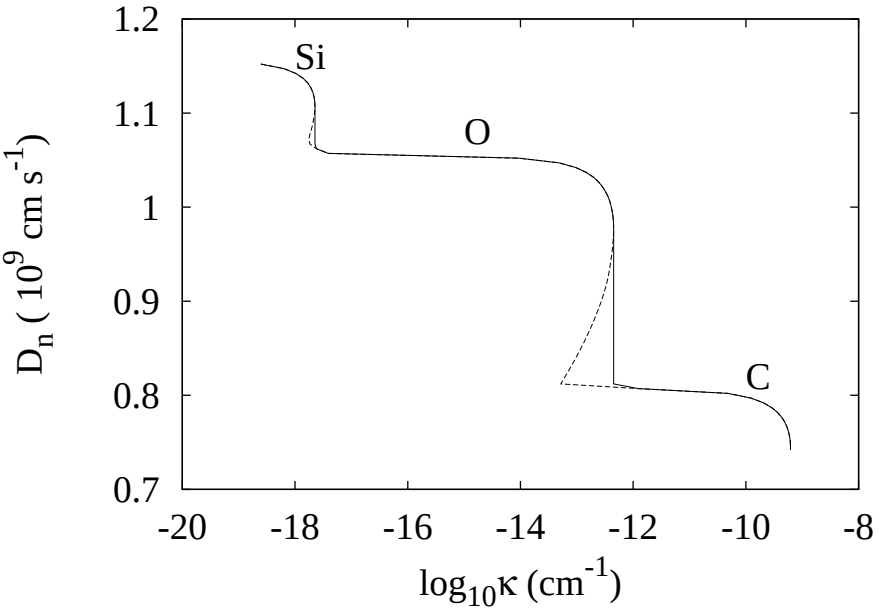

Figure 2.8: $D_n - \kappa$ curve for initial C-O density 10^6 g cm^{-3}. The solid line is the evolution path of an expanding front (Sharpe 2001).

on the different branches being typically orders of magnitude different. The overall reaction length of the wave would increase as the curvature increases due to lower shock temperatures and reaction rates. However, this has no effect on the front dynamics due to being downstream of the frozen sonic point.

Figure 2.11 shows the value of the extinction curvature of each branch as a function of initial density. The higher the initial density, the larger the curvature required for the detonation to fail due to the rapidly decreasing reaction length scales. For densities less than 1.11×10^7 g cm^{-3}, the detonation only fails when the C branch extinction curvature is reached. For a detonation propagating through a C-O core, one would in general expect the radius of curvature of the shock front to be of the order of the C-O radius or of the density scale height (both $\sim 10^8$ cm) or less, corresponding to curvatures of the order of 10^{-8} cm^{-1} or more. However, figure 2.11 shows that for densities less than about 1.8×10^6 g cm^{-3}, the detonation will be extinguished whenever such curvatures are encountered. Hence it would be unlikely that a detonation could be established or maintained in C-O regions where the density is less than this value and clearly this has important implications for SN Ia detonation models involving low density regions.

Shown in figure 2.11 is the detonation speed at the turning point i.e. the extinction

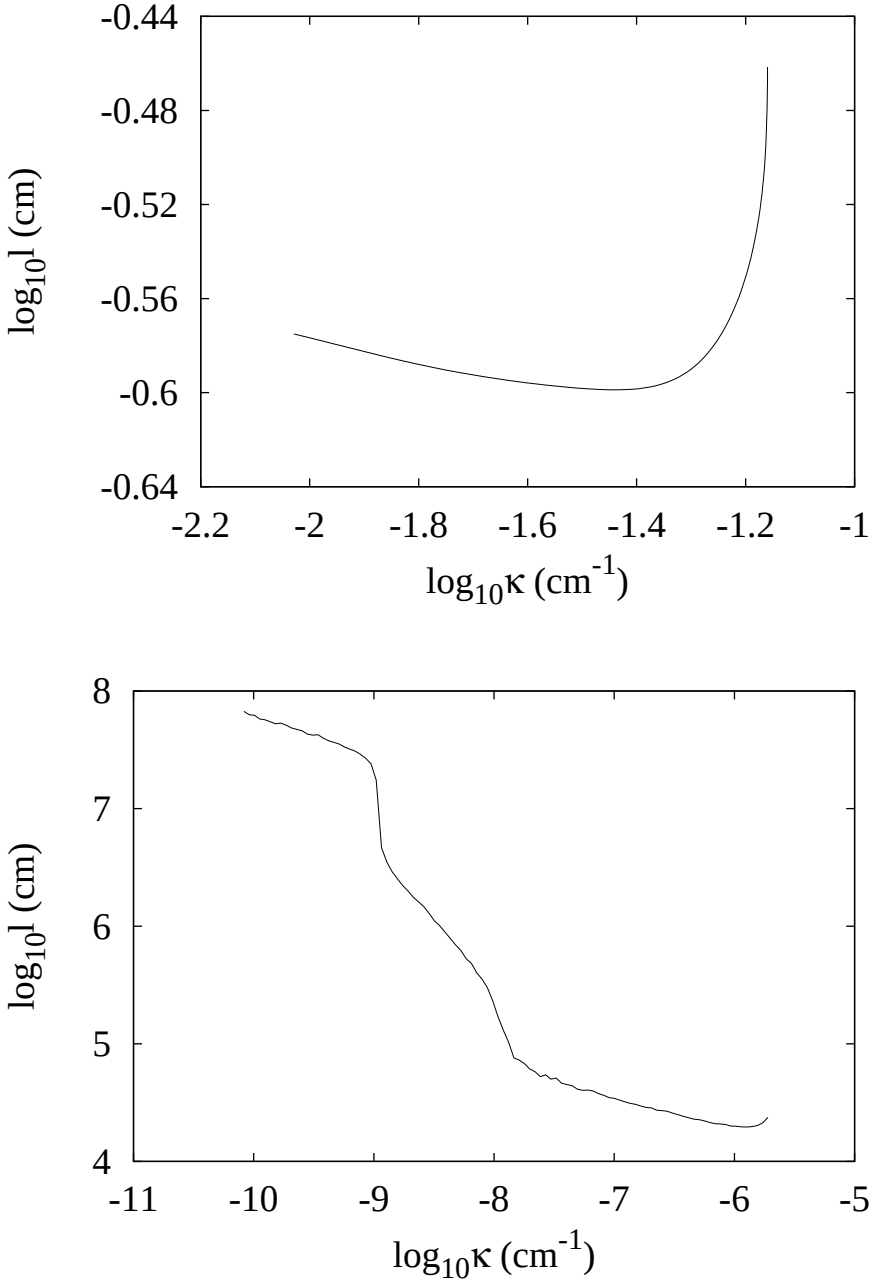

Figure 2.9: Driving zone reaction lengths (distance from shock to the sonic point) for curved C-O detonations as a function of shock front curvature, for initial densities of 10^9 (top) and 10^7 (bottom) g cm^{-3}.

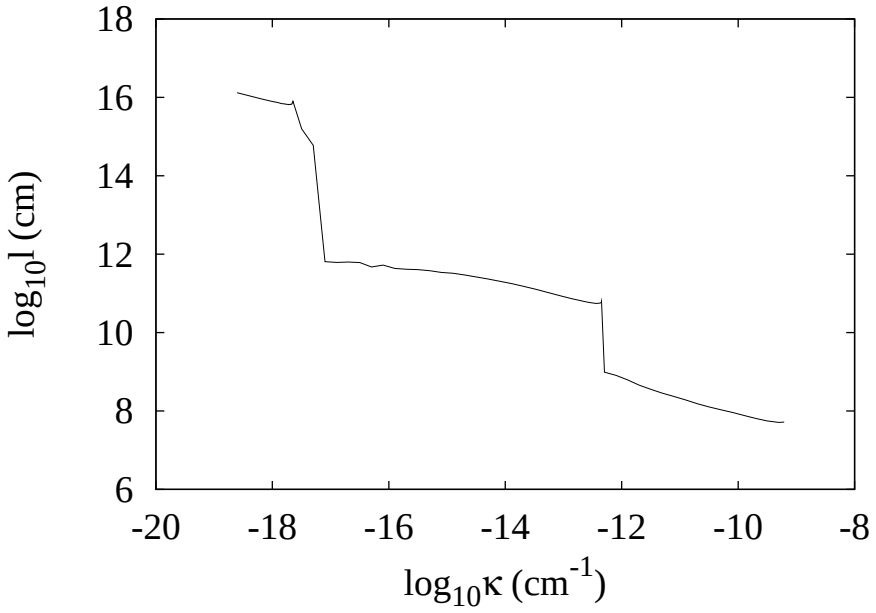

Figure 2.10: Driving zone reaction length (distance from shock to sonic point) as a function of shock front curvature for an initial density of 10^6 g cm^{-3}.

curvature, relative to the corresponding planar speed, $D_n/D_{\rm planar}$, attained at the turning points of the three branches. The difference in detonation speed between the O and C branches is greater than from the Si to O branches. Therefore when the sonic point drops to the C branch, one would expect curvature effects to be at their greatest in comparison to the planar propagation.

Finally figure 2.12 shows the driving zone reaction lengths for each branch as measured at the turning point. The Si branch reaction lengths are the largest and if the sonic point is located here, the reaction length would be comparable or larger than the density scale height. At a density of about 6.75×10^6 g cm^{-3} the reaction length is already 10^8 cm. Therefore, as the turning point is approached on the Si branch, the quasi-one-dimensional, quasi-steady assumptions of the $D_n - \kappa$ analysis begins to break down. The driving lengths of the O branches are orders of magnitudes smaller than on the Si branch and those of the C branch much smaller still. Hence the $D_n - \kappa$ theory assumptions are more self-consistent for propagation on these branches. However, these lengths begin to increase rapidly as the turning point of a branch is approached. Even the C branch will have reaction lengths larger than the core radius for low enough densities (less than about 8.8×10^5 g cm^{-3}) near its turning point. Hence when applying DSD to SN Ia explosions, it will be important to check

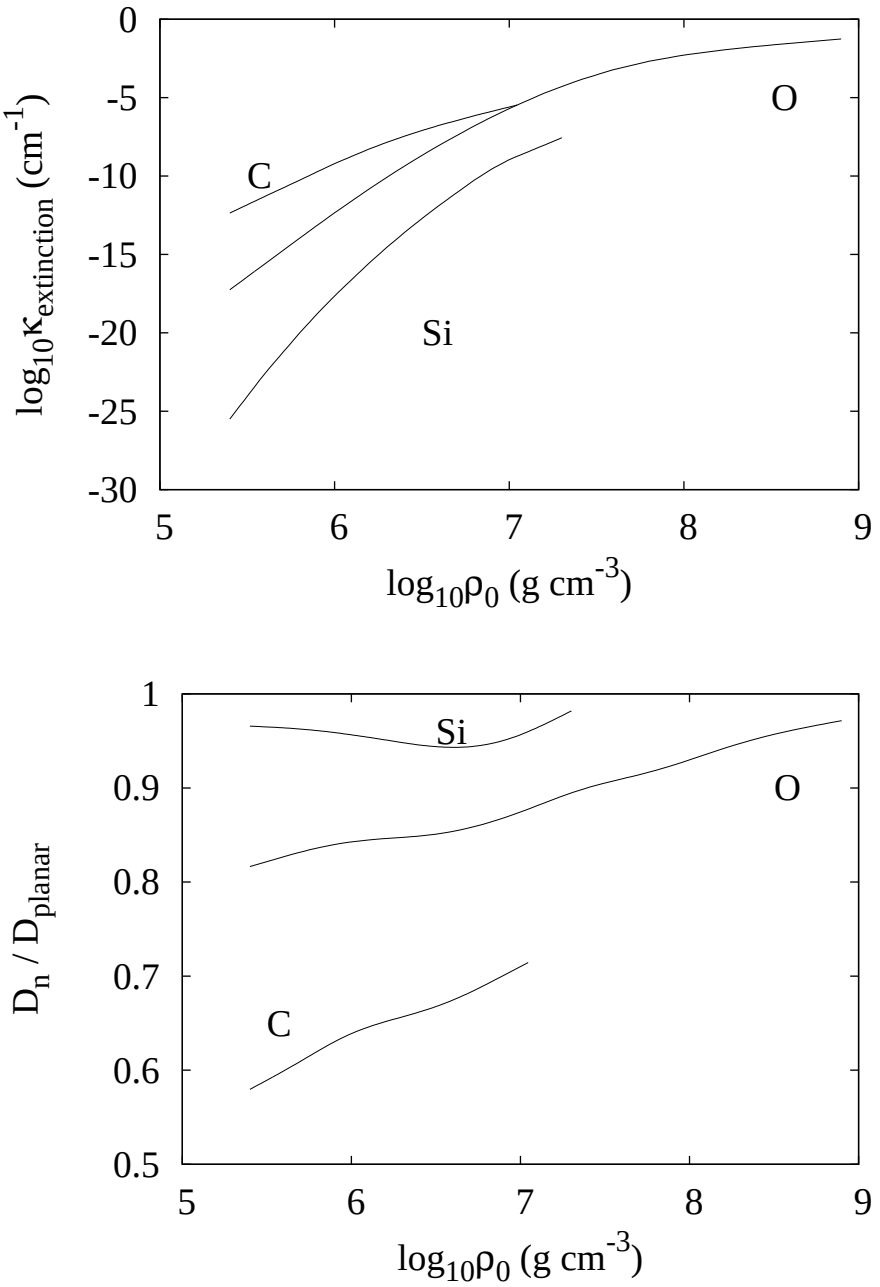

Figure 2.11: Extinction curvature (top) and $D_n/D_{\rm planar}$ (bottom) at the turning point of each $D_n - \kappa$ solution branch for curved C-O detonations, as a function of initial density.

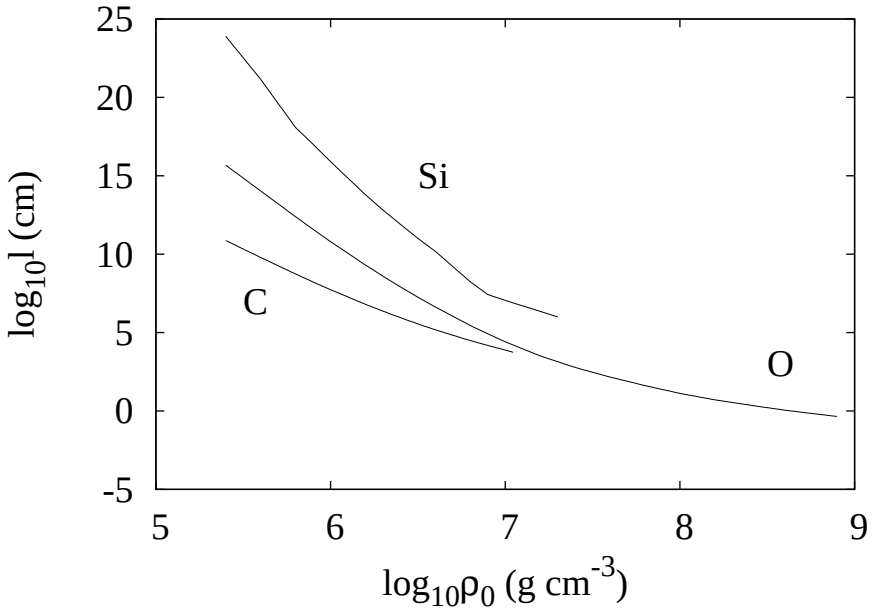

Figure 2.12: Effective reaction length (distance from shock to sonic point) at the turning point of each $D_n - \kappa$ solution branch for curved C-O detonations, as a function of initial density.

whether the results are consistent with the slowly varying assumption of the theory, i.e. are the effective reaction zone lengths less than the density scale height.

The $D_n - \kappa$ curves for He are found to consist only of a single branch at all densities. Figure 2.13 (top) shows a typical $D_n - \kappa$ curve for He, corresponding to an initial density of 10^6 g cm^{-3} (the results for other densities are found to be qualitatively similar) with its effective reaction length (bottom). Figure 2.14 (top) also shows the extinction curvature of the He detonations as a function of initial density. Lower densities have smaller extinction curvatures due to increasing reaction lengths. Again in SNe Ia, detonation fronts with radii of curvatures greater than the characteristic size of the star are unlikely to be encountered. For He, the extinction curvature is less than 10^{-8} cm^{-1} in regions where the density is less than about 2×10^5 g cm^{-3}. Thus a detonation would not propagate very far into such a low density before becoming extinguished and this has important implications for SN Ia models involving the detonation of low density He shells. However, figure 2.14 (bottom) shows that detonations can be sustained in He with larger velocity drops from the planar value compared to those in C-O. Indeed, the speeds at the extinction point in figure 2.14 (bottom) are all below half that of their planar value. The effective reaction zone lengths of He also increase rapidly as the density decreases (figure 2.15). The driving length at the extinction point becomes larger

than 10^8 cm at a density of 1.5×10^5 g cm^{-3} and hence again it will be necessary to check the validity of DSD theory when applied to SNe Ia in regions with densities lower than this.

When the curvature is sufficiently high and the final extinction point is reached (C or O for pathological C-O detonations and the end of the single branch in He), the detonation front is extinguished and the shock wave travels inertly at almost the frozen sound speed. The frozen sound speed in various densities for both C-O and He is shown in figure 2.16. There is a small difference between the two at low densities with the He sound speed being higher. As the density increases, the sound speed increases and the difference between the two becomes less but never zero.

2.5 Summary

The relevant theory behind both curved and planar detonations has been discussed. A simple example showing how to obtain $D_n - \kappa$ curves for an ideal gas to use in a DSD subgrid modelling version has been demonstrated. This has then been discussed in the more complex scenario of detonation waves in SNe Ia. The main features of C-O detonation in SNe Ia are the three burning stages of C, O and then finally Si. The end of O burning is known as nuclear statistical quasi-equilibrium (NSQE) and the end of Si burning as nuclear statistical equilibrium (NSE).

One can form a preliminary conjecture from the results discussed in this section: if the reactions were unable to proceed to NSE for some reason, i.e. curvature of the front becoming too great or the effective detonation reaction length becoming comparable to the radius of the star, then the intermediate mass elements C, O or Si would remain, instead of being transformed to Ni. Features related to the $D_n - \kappa$ curves such as the effective reaction length and speeds at turning points have also been shown. The decrease in speed and effective reaction lengths for low densities is greater than that of high densities. It would therefore be expected that low density models (i.e. sub-Chandrasekhar) would be more affected by the inclusion of these effects. Overall there would be greater intermediate mass element production and lower expansion velocities compared to the planar detonation speed assumption.

Finally, the models to be investigated are mainly in two dimensions and need a suitable front tracking algorithm. There are a variety of methods for tracking fronts in two or three

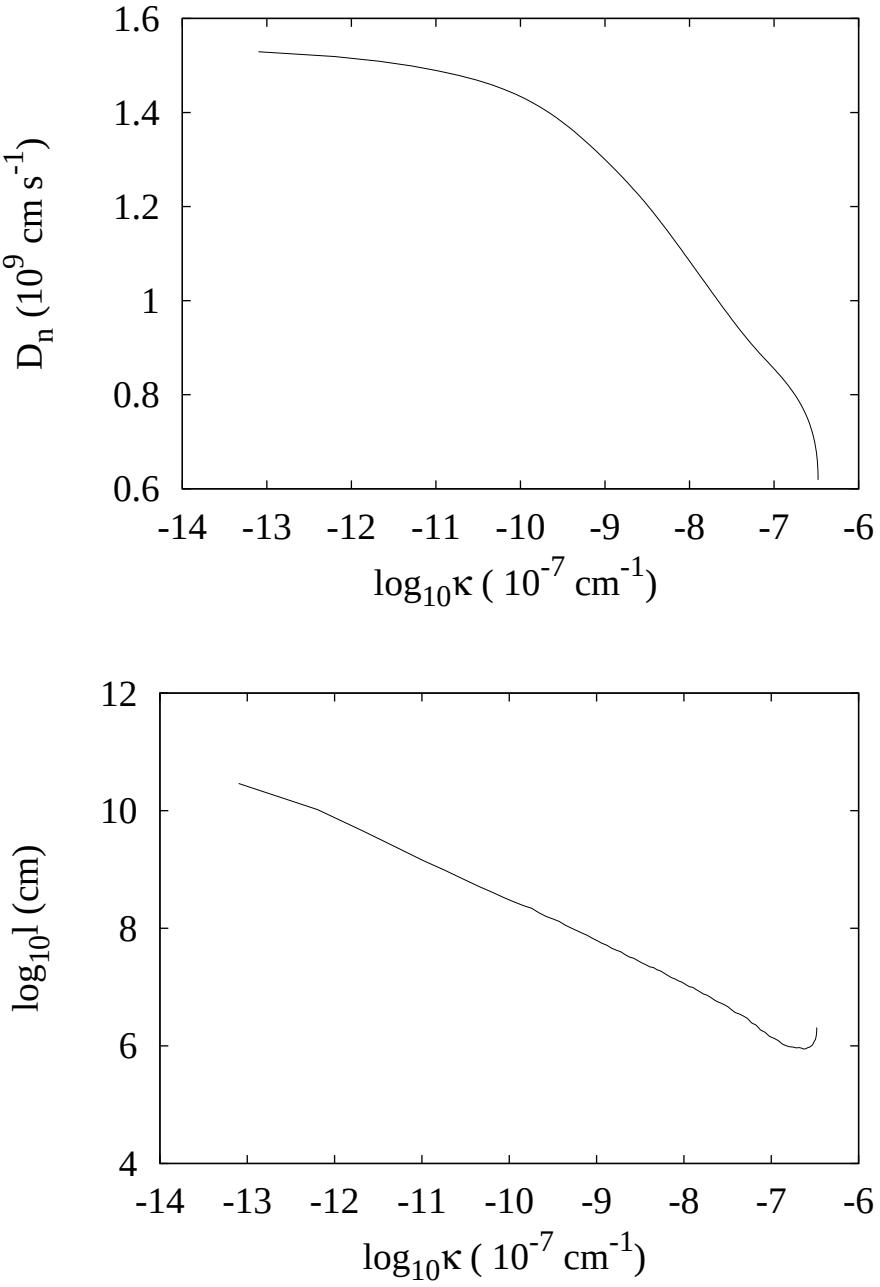

Figure 2.13: (Top) $D_n - \kappa$ curve and (bottom) corresponding driving reaction lengths (distance from shock to sonic point) for curved He detonations with initial density 10^6 g cm^{-3}.

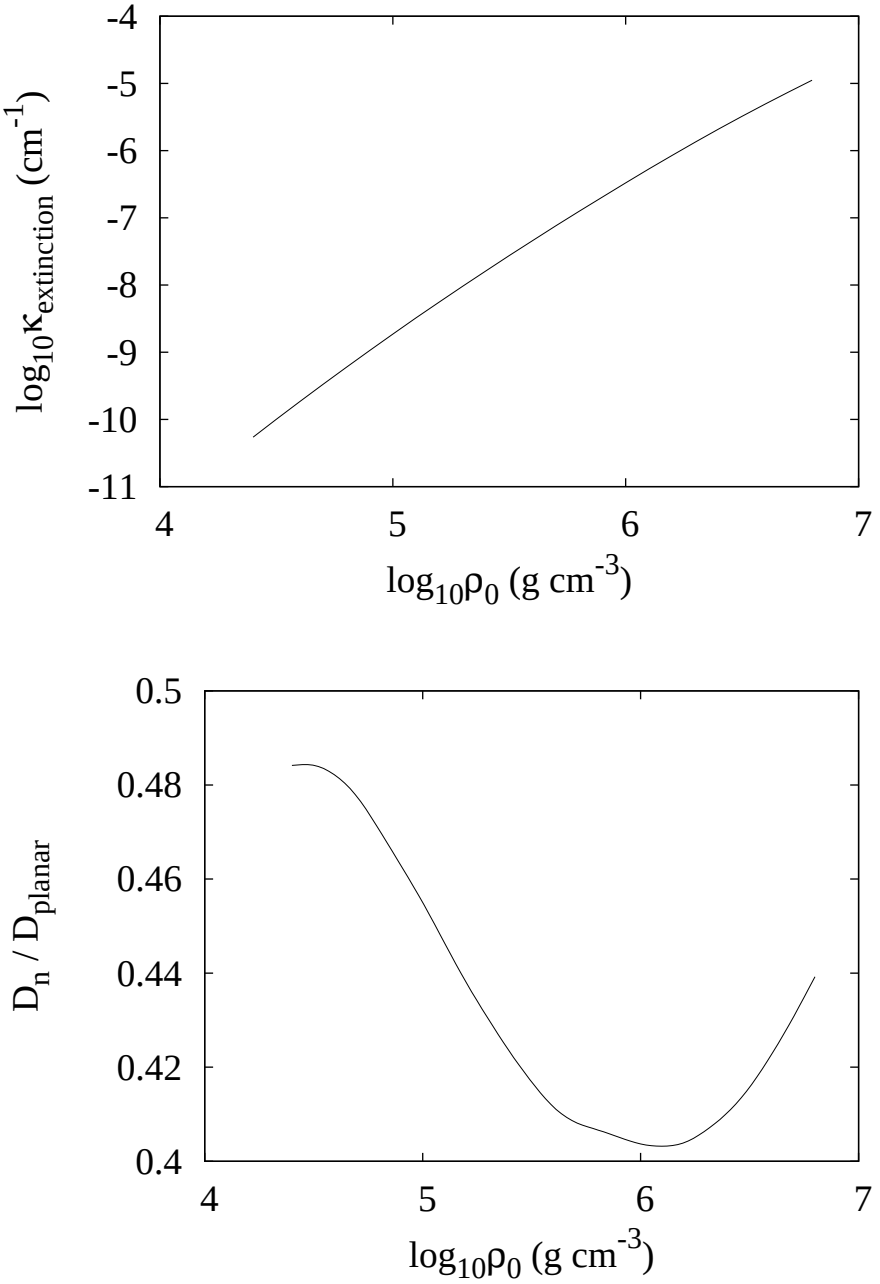

Figure 2.14: Top: Extinction curvatures and bottom: $D_n/D_{\rm planar}$ at the turning point of the $D_n - \kappa$ solution for curved He detonations, as a function of initial density.

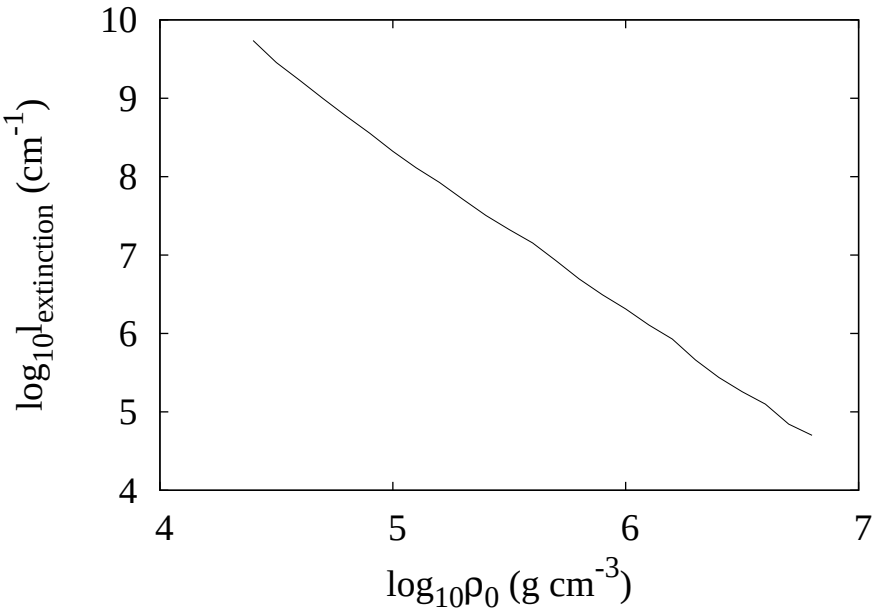

Figure 2.15: Effective reaction length (distance from shock to sonic point) at the turning point of each $D_n - \kappa$ solution branch for curved He detonations, as a function of initial density.

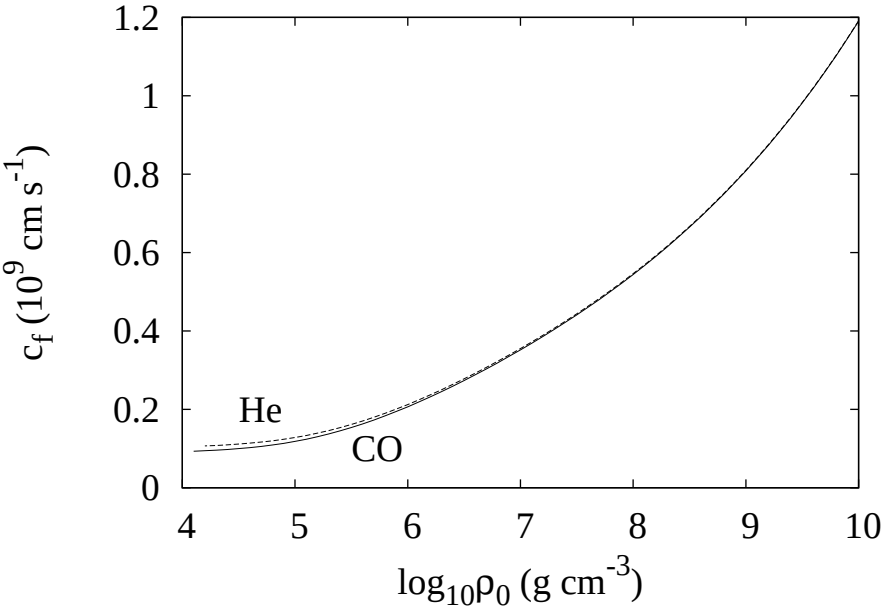

Figure 2.16: Frozen sound speeds in C-O and He.

dimensions. The next chapter discusses one of them and its implementation.

Chapter 3

The Level Set Method

3.1 Introduction

A suitable method is needed to investigate the effects of curvature on the front dynamics of detonations in SNe Ia. There are issues involved in the general motion of a front. These can be topological such as the merging or breaking of the front. Cusps can form on the front due to an interface separating two different regions e.g. the detonation front with He and C-O (Wiggins and Falle 1997).

Sethian (1999) discusses some traditional techniques for tracking front evolution moving with speed $F = 1 - \epsilon\kappa$, where ϵ is a constant, e.g. discrete parametisation of a curve with marker particle techniques. However, oscillations in the solutions can develop and when corners or cusps form, markers must be removed and information is lost. When there is no influence of curvature (which acts like a smoothing or viscous term) and thus the solution is not necessarily differentiable, markers do not know about entropy conditions and weak solutions due to tracking a Lagrangian formulation. Two fronts merging would also require the removal of markers and in higher dimensions this can be complex. Wiggins and Falle (1997) used the method of geometric optics to overcome some of these problems in their subgrid model. However, their method does not take into account detonation speeds with curvature dependence.

Taking the above problems into account, it is evident there is a requirement for a numerical method which accounts for discontinuous solutions and topological changes. Level set methods are based on the theory of curve and surface evolution and the link between hyperbolic

conservation laws and front propagation. A time-dependent, Eulerian initial value partial differential equation represents the position of the front and how it evolves under a speed $F = F_{\text{prop}} + F_{\text{curv}}$, where the first term is the propagation speed and the second term the curvature dependent speed. This equation is a Hamilton-Jacobi equation and Sethian shows the link between equations of this form and hyperbolic conservation laws, thus allowing the numerical methods for the latter to be applied to front propagation. Curvature and topological changes of the front are handled naturally by this method.

The level set method is described in this chapter and its general numerical implementation. It is then tested. This is then adapted specifically for SNe Ia problems and again tested and certain parameters of the problem justified. The surface evolution equation in DSD is $D_n = D_{\text{planar}} - \alpha(\kappa)$ which fits in well with the analysis of F and level sets. Aslam, Bdzil and Stewart (1996) were the first to use level sets with DSD in detonation propagation.

3.2 Derivation

The level set method involves embedding the surface of interest in a field one space dimension higher. This field, ψ, is then evolved and the surface of interest within this field evolves accordingly, handling convergence, divergence etc. of the front easily. This ψ consists of level curves ψ =const. If the level curve $\psi = 0$ is identified as the front and inside the front $\psi < 0$ and outside $\psi > 0$, then ψ is the signed distance function to the front. The front is then found within the surface at the end of each time step. As a simple example take a front initially at $x = 5$, then $\psi(t = 0) = x - 5$.

To derive the equation used to evolve ψ, then as each level curve $\psi(x, y, z, t)$ =constant, the total derivative is

$$\frac{\partial \psi}{\partial t} + \frac{\partial \psi}{\partial x}\frac{dx}{dt} + \frac{\partial \psi}{\partial y}\frac{dy}{dt} + \frac{\partial \psi}{\partial z}\frac{dz}{dt} = 0. \tag{3.1}$$

As dx/dt etc. are components of the surface velocity $\mathbf{D}$, then

$$\frac{\partial \psi}{\partial t} + \nabla\psi \cdot \mathbf{D}(\rho_0, \kappa) = 0. \tag{3.2}$$

The front unit normal $\hat{\mathbf{n}}$ in the direction of outwards propagation is given by

$$\hat{\mathbf{n}} = \frac{\nabla\psi}{|\nabla\psi|}, \tag{3.3}$$

and the curvature by

$$\kappa \quad = \quad \nabla \cdot \hat{\mathbf{n}}. \tag{3.4}$$

Since $\mathbf{D} \cdot \hat{\mathbf{n}} = D_n$ and using equation (3.3), then (3.2) becomes

$$\frac{\partial\psi}{\partial t} + D_n(\rho_0, \kappa)\,|\nabla\psi| = 0. \tag{3.5}$$

3.3 Numerical Implementation

Next the numerical method for solving (3.5) is described following Sethian (1999) and Aslam, Bdzil and Stewart (1996). The level set equation is first expanded as there is a hyperbolic and parabolic component. As $D_n = D_{\text{planar}} - \alpha(\kappa)$, then

$$\frac{\partial\psi}{\partial t} + D_{\text{planar}}\,|\nabla\psi| - \alpha(\kappa)\,|\nabla\psi| = 0. \tag{3.6}$$

The second term is hyperbolic and the third term is parabolic. Osher and Sethian (1988) show this for the one dimensional case of a graph. This equation in one dimension, where $\psi(x,t)$ is the height function at time t, for a linear $D_n = D_{\text{planar}} - \alpha\kappa$, is

$$\psi_t + D_{\text{planar}}\sqrt{1+\psi_x^2} = \alpha\frac{\psi_{xx}}{1+\psi_x^2}. \tag{3.7}$$

Differentiating both sides with respect to x and defining $u = \psi_x$, then

$$u_t + D_{\text{planar}}\left[\sqrt{1+u^2}\right]_x = \alpha\left[\frac{u_x}{1+u_x^2}\right]_x. \tag{3.8}$$

If $u = v_0 + \delta v + O(\delta^2)$, where v_0 is a constant and δ is small, then substituting this into the above equation and differentiating gives

$$\delta v_t + \frac{\delta D_{\text{planar}} v_0 v_x}{\sqrt{1+(v_0+\delta v)^2}} = \alpha\frac{\delta v_{xx}}{1+(v_0+\delta v)^2} + O(\delta^2). \tag{3.9}$$

The terms on the denominator can be expanded for small δ as

$$\frac{1}{\sqrt{1+(v_0+\delta v)^2}} = \frac{1}{\sqrt{1+v_0^2}} - \frac{v_0 v}{(1+v_0^2)^{3/2}}\delta + O(\delta^2), \tag{3.10}$$

$$\frac{1}{1+(v_0+\delta v)^2} = \frac{1}{1+v_0^2} - \frac{2v_0 v}{(1+v_0^2)^2}\delta + O(\delta^2). \tag{3.11}$$

Then to order δ

$$v_t + \frac{D_{\text{planar}} v_0 v_x}{\sqrt{1+v_0^2}} = \alpha \frac{v_{xx}}{1+v_0^2}. \tag{3.12}$$

Let $D' = D_{\text{planar}} v_0/\sqrt{1+v_0^2}$ and $\alpha' = \alpha/(1+v_0^2)$, then

$$v_t + D' v_x = \alpha' v_{xx}, \tag{3.13}$$

i.e. the second term represents waves travelling at speed D' and the right-hand side is a viscous term.

When α is non-zero, the viscosity term smooths the solution and as α approaches zero, discontinuities can form. An entropy condition is required for the correct viscosity limit, i.e. when time is increasing, characteristics flow into a discontinuity. For Hamilton-Jacobi equations in two dimensions one could try $u = \psi_x$ and $v = \psi_y$, but then u and v are related through mixed partials. Instead a viscous term is added directly to the right hand side of the Hamilton-Jacobi equation for two dimensions (e.g. $\alpha(\kappa)\,|\nabla\psi|$). This resulting equation behaves the same as the viscous conservation law where the solution is smooth for a non-zero right hand side and also gives the correct entropy solution in the limit of zero right hand side.

3.3.1 Interior Differencing

First the interior differencing is considered for an expanding front. The first term is calculated by first-order forward Euler differencing

$$\frac{\partial \psi}{\partial t} = \frac{\psi_{i,j}^{n+1} - \psi_{i,j}^{n}}{\Delta t}, \tag{3.14}$$

where i and j represent the x and y nodes respectively, Δt is the time step and n the time index. The second term in (3.6) requires a numerical treatment applicable to hyperbolic PDEs. This requires the approximations to the upwind derivatives, i.e. the numerical stencil contains the mathematical domain of dependence. The forward and backwards difference operators are defined as

$$D_x^+\psi_{i,j}^n = \frac{\psi_{i+1,j}^n - \psi_{i,j}^n}{\Delta}, \quad D_x^-\psi_{i,j}^n = \frac{\psi_{i,j}^n - \psi_{i-1,j}^n}{\Delta},$$

$$D_y^+\psi_{i,j}^n = \frac{\psi_{i,j+1}^n - \psi_{i,j}^n}{\Delta}, \quad D_y^-\psi_{i,j}^n = \frac{\psi_{i,j}^n - \psi_{i,j-1}^n}{\Delta}, \tag{3.15}$$

where $\Delta = \Delta x = \Delta y$ is the mesh spacing. This leads to the upwind first order calculation for the second term based on the Engquist-Osher numerical flux as

$$\begin{aligned} |\nabla\psi| &= \Big\{\min\left[D_x^+\psi_{i,j}^n, 0\right]^2 + \max\left[D_x^-\psi_{i,j}^n, 0\right]^2 \\ &\quad + \min\left[D_y^+\psi_{i,j}^n, 0\right]^2 + \max\left[D_y^-\psi_{i,j}^n, 0\right]^2\Big\}^{1/2}. \end{aligned}$$

The min and max functions here ensure the chosen derivative always looks upwind (the direction from which information is flowing). Looking at the derivatives in the x direction, two possible approximations to the derivatives exist. These are the forwards ($D_x^+\psi_{i,j}^n$) or backwards ($D_x^-\psi_{i,j}^n$) differences. If the derivative is positive, the front is moving in the positive x direction. The value $\psi_{i-1,j}^n$ must be used as information is flowing from the negative x direction. The min function is zero and the max is the backwards derivative. Similarly, if the derivative is negative, then the front is moving in the negative x direction. This requires the value at $\psi_{i+1,j}^n$ as information is coming from the positive x direction. In this case the min function is the forwards derivative and the max is zero.

The first order approximation is monotone (a non-decreasing function of all its arguments) and has the advantages that no spurious oscillations may develop and takes into account entropy solutions. Unfortunately it is limited to first order and any discontinuities may be smeared out. However, it forms a basis for a higher accuracy approximation. The second-order spatial calculation is

$$|\nabla\psi| = \left\{\min(A,0)^2 + \max(B,0)^2 + \min(C,0)^2 + \max(D,0)^2\right\}^{1/2}, \tag{3.16}$$

where

$$\begin{aligned}
A &= D_x^+\psi_{i,j}^n - \frac{\Delta}{2}\min\text{mod}(D_x^- D_x^+\psi_{i,j}^n,\ D_x^+ D_x^+\psi_{i,j}^n),\\
B &= D_x^-\psi_{i,j}^n - \frac{\Delta}{2}\min\text{mod}(D_x^- D_x^-\psi_{i,j}^n,\ D_x^+ D_x^-\psi_{i,j}^n),\\
C &= D_y^+\psi_{i,j}^n - \frac{\Delta}{2}\min\text{mod}(D_y^- D_y^+\psi_{i,j}^n,\ D_y^+ D_y^+\psi_{i,j}^n),\\
D &= D_y^-\psi_{i,j}^n - \frac{\Delta}{2}\min\text{mod}(D_y^- D_y^-\psi_{i,j}^n,\ D_y^+ D_y^-\psi_{i,j}^n).
\end{aligned}$$

The derivatives $D_x^- D_x^+\psi_{i,j}^n$ and $D_x^+ D_x^+\psi_{i,j}^n$ work out to be the central and forward difference calculations respectively to the second derivatives etc. The function min mod is defined as

$$\min\text{mod}(a,b) = \begin{cases} a, & \text{if } |a| \le |b|, ab > 0.\\ b, & \text{if } |b| < |a|, ab > 0\ \cdot\\ 0, & \text{otherwise.}\end{cases} \tag{3.17}$$

The second order hyperbolic scheme uses what is known as essentially non-oscillatory (ENO) interpolation (Osher and Sethian 1988; Sethian 1999; Osher and Fedkiw 2003). ENO was developed to overcome the numerical difficulties of nonlinear conservation laws with high accuracy. This means the approximation to $\psi_{i,j}^n$ is non-oscillatory, even if discontinuous. High-order polynomial interpolation is not used across a discontinuity to avoid oscillations of the solution. First order interpolation is the same as first order differencing and second order interpolation is the same as second order differencing. Looking at A for example, the first term is using the forward difference at nodes (i,j) and $(i+1,\ j)$. To construct the second derivative with these nodes, either the node at $(i-1,j)$ can be used or $(i+2,j)$. The first choice results in the central difference and the latter results in the forward difference of the second derivative. The smallest in magnitude of the second derivative is chosen, therefore limiting oscillations. If a discontinuity is detected it returns zero and reverts to first order. This method can be extended to higher accuracy by performing similar for the third derivatives

and fourth derivatives etc.

Lastly, the third term which depends upon curvature is parabolic. This parabolic contribution 'behaves' like a nonlinear heat equation and information propagates in both directions. The most straightforward approach is to calculate $|\nabla\psi|$ by central differences and substituting them for ψ_x etc. in equation (3.6). Similarly, in the expression for κ, central differences are used in the expression for mean curvature. Osher and Sethian (1988) discuss why central differences should be used with an example. A circle moving with speed $F = -\kappa$ will consist of concentric level curves within ψ. When the radii of these circles is small, i.e. near the centre, the curvature will be large. The parabolic term in equation (3.6) has multiplication and division by $(\psi_x^2 + \psi_y^2)^{1/2}$. Near the origin this is close to zero. Large errors will result if the approximations to ψ_x and ψ_y in $|\nabla\psi|$ and κ are not the same and therefore central differences are used.

3.3.2 Boundary Conditions

There are two types of boundary conditions relevant to the problem. These are symmetric (perfectly reflecting) and non-reflecting (inflow/outflow). The second order scheme requires two ghost nodes per boundary. At the end of each time step calculation, for the symmetric boundary condition the two interior nodes nearest to the boundary are simply reflected to the exterior, e.g. $\psi^n_{-2,j} = \psi^n_{2,j}$ and $\psi^n_{-1,j} = \psi^n_{1,j}$ for $\psi^n_{0,\,j}$ at $x = 0$. Quadratic extrapolation is used for the non-reflecting condition, or equivalently, the second derivative is constant along the normal on the boundary, e.g. $\psi^n_{-1,\,j} = 3\psi^n_{0,\,j} - 3\psi^n_{1,\,j} + \psi^n_{2,\,j}$ as the approximation to the third derivative is then zero (Aslam, Bdzil and Stewart 1996).

3.3.3 Initial Condition

The value of ψ at $t = 0$ represents the initial front locus and as mentioned is positive in unburnt material, negative in burnt material and zero at the front location. For an ignition centred at (x_1, y_1) with initial radius r_0

$$\psi(\,x,\,y,\,t=0) = \sqrt{(x-x_1)^2 + (y-y_1)^2} - r_0. \tag{3.18}$$

3.3.4 Time Step

Next a suitable time step needs to be determined. A Von Neumann analysis is used on the first order numerical stencil by first considering the level set equation being only hyperbolic and then only parabolic on a uniform grid. Although what follows is for the first order differencing, the numerical stencil reduces to first order in discontinuous regions. Assume the solution is

$$\psi = G(t)\exp[i(k_m x + k_n y)], \tag{3.19}$$

where $G(t)$ is the amplitude, $k_m = m\pi/L_x$ $(m = 1, 2, ...,)$ and $k_n = n\pi/L_y$ $(n = 1, 2, ...,)$ are the wave numbers and L_x and L_y represent the lengths of the domains in the x and y directions respectively. The error can grow exponentially with time, so assume $G(t) = \exp(at)$, where a is a constant. The necessary and sufficient condition for the error to be bounded is if $|G| \leq 1$. Considering first the hyperbolic part, the level set equation is

$$\psi_t = -D_{\text{planar}} \left|\nabla\psi\right|, \tag{3.20}$$

and the approximation to the solution at the nodes becomes

$$\begin{aligned}
\psi_{i,j}^n &= \exp[(at + i(k_m x + k_n y)], && (3.21)\\
\psi_{i+1,j}^n &= \exp[at + i(k_m(x + \Delta) + k_n y))], && (3.22)\\
\psi_{i-1,j}^n &= \exp[at + i(k_m(x - \Delta) + k_n y))], && (3.23)\\
\psi_{i,j+1}^n &= \exp[at + i(k_m x + k_n(y + \Delta))], && (3.24)\\
\psi_{i,j-1}^n &= \exp[at + i(k_m x + k_n(y - \Delta))], && (3.25)\\
\psi_{i,j}^{n+1} &= \exp[a(t + \Delta t) + i(k_m x + k_n y)]. && (3.26)
\end{aligned}$$

All possible forms of upwinding must be considered. Usually either a backwards or forwards difference will be selected. However, when there is a discontinuity in ψ, both the forwards and backwards difference will be selected for the x or y directions or even both, depending upon the nature of the discontinuity. Considering both directions in x and y and substituting in the approximation to the solution at the nodes and simplifying, the numerical stencil becomes

$$\begin{aligned}\exp(a\Delta t) &= 1 - \frac{D_{\text{planar}}\Delta t}{\Delta}\Big\{[\exp(ik_m\Delta) - 1]^2 + [1 - \exp(-ik_m\Delta)]^2 \\ &\quad + [\exp(ik_n\Delta) - 1]^2 + [1 - \exp(-ik_n\Delta)]^2\Big\}^{1/2}.\end{aligned}$$

Expanding the squares and using $2\cos\theta = \exp(i\theta) + \exp(-i\theta)$ and simplifying, then

$$\begin{aligned}\exp(a\Delta t) &= 1 - \frac{D_{\text{planar}}\Delta t}{\Delta}\{2\cos(2k_m\Delta) - 4\cos(k_m\Delta) + 4 \\ &\quad + 2\cos(2k_n\Delta) - 4\cos(k_n\Delta)\}^{1/2}.\end{aligned}$$

This equation needs to be ≤ 1 in magnitude for all k_m, k_n, and Δ for the errors to not grow with time. The terms $2\cos(2\theta) - 4\cos(\theta)$ has a maximum value of 6 at odd integer multiples of π. Therefore

$$\left|1 - \frac{4D_{\text{planar}}\Delta t}{\Delta}\right| \leq 1, \tag{3.27}$$

holds if

$$\frac{2D_{\text{planar}}\Delta t}{\Delta} \leq 1. \tag{3.28}$$

Now considering just the parabolic part, for a linear $D_n = -\alpha\kappa$, α here is a positive constant, this is

$$\psi_t = \alpha\frac{\psi_{xx}\psi_y^2 - 2\psi_{xy}\psi_x\psi_y + \psi_{yy}\psi_x^2}{\psi_x^2 + \psi_y^2}. \tag{3.29}$$

This can be rewritten as

$$\psi_t = \alpha(a^2\psi_{xx} - 2ab\psi_{xy} + b^2\psi_{yy}), \tag{3.30}$$

where

$$a^2 = \frac{\psi_y^2}{\psi_x^2 + \psi_y^2}, \quad b^2 = \frac{\psi_x^2}{\psi_x^2 + \psi_y^2}, \tag{3.31}$$

and $a^2 + b^2 = 1$. Similar to before, substituting in the appropriate approximations at the nodes for central differencing leads to

$$\begin{aligned}\exp(a\Delta t) &= 1 + \frac{\alpha\Delta t}{\Delta^2}\left\{a^2\left[\exp(ik_m\Delta) - 2 + \exp(-ik_m\Delta)\right] - ab\left[\exp(i(k_m + k_n)\Delta)\right.\right. \\ &\quad + \exp(-i(k_m + k_n)\Delta) - \exp(i(k_m - k_n)\Delta) - \exp(-i(k_m - k_n)\Delta)\left.\right]/2 \\ &\quad \left. + b^2\left[\exp(ik_n\Delta) - 2 + \exp(-ik_n\Delta)\right]\right\}.\end{aligned}$$

This goes to

$$\begin{aligned}\exp(a\Delta t) &= 1 + \frac{\alpha\Delta t}{\Delta^2}\left\{2a^2\left[\cos(k_m\Delta) - 1\right]\right. \\ &\quad - ab\left[\cos((k_m + k_n)\Delta) - \cos((k_m - k_n)\Delta)\right]/2 \\ &\quad \left. + 2b^2\left[\cos(k_n\Delta) - 1\right]\right\}.\end{aligned}$$

As $2\sin(\theta/2) = 1 - \cos(\theta)$ and using the angle sum and difference identity, then

$$\exp(a\Delta t) = 1 - \frac{2\alpha\Delta t}{\Delta^2}\left[2a^2\sin^2(k_m\Delta/2) - \frac{ab}{2}\sin(k_m\Delta)\sin(k_n\Delta) + 2b^2\sin^2(k_n\Delta/2)\right]. \quad (3.32)$$

The bracket term will be largest when $\sin^2 = 1$, i.e. half multiples of π. However, any integer multiple of π makes the middle term in the brackets zero. As $a^2 + b^2 = 1$, then

$$\left|1 - \frac{4\alpha\Delta t}{\Delta^2}\right| \leq 1, \quad (3.33)$$

and this holds for

$$\frac{2\left|\alpha\right|\Delta t}{\Delta^2} \leq 1. \quad (3.34)$$

The time step restriction for the full level set equation in two dimensions with a linear D_n is

$$\frac{2D_{\text{planar}}\Delta t}{\Delta} + \frac{2\left|\alpha\right|\Delta t}{\Delta^2} \leq 1. \quad (3.35)$$

If the D_n is nonlinear, then the constant $|\alpha|$ term is replaced by $\max(|\partial\alpha/\partial\kappa|)$ and then

$$\Delta t \leq \frac{\Delta^2}{2(D_{\text{planar}}\Delta + \max\left(|\partial\alpha/\partial\kappa|\right))}. \tag{3.36}$$

3.3.5 Burn Table Creation

Saving ψ after every time step would be impractical. As $D_n > 0$ always, then from equation (3.5) $\psi_t = -D_n\,|\nabla\psi| \leq 0$. In other words ψ_t is always decreasing monotonically. Positive ψ decreases as the front approaches it and negative ψ decreases as the front moves away. A more practical way is to create what is known as a burn table, t^b. This is an array where each node contains the time when the $\psi = 0$ contour arrived. The sign of the old and new $\psi_{i,j}$ can be compared at the end of the time step. If the sign has changed then this means the front has passed the node. Linear interpolation in time is performed between the points for that node.

3.3.6 Test Problem

Second order convergence of the scheme is next shown as in Aslam, Bdzil and Stewart (1996) to check everything is set up correctly. Even though the truncation error due to the differencing of the time step is $\mathrm{O}(\Delta t)$, second order convergence will be achieved, as from equation (3.36) it can be seen $\Delta t \propto \Delta^2$ as $\Delta \to 0$.

The test problem from Aslam, Bdzil and Stewart (1996) is an expanding quarter circle with a numerical domain of $0 \leq x \leq 1$ and $0 \leq y \leq 1$. The circle is centred at the origin and has an initial radius of $r_0 = 0.2$. The boundary conditions are symmetric (reflective) at $x = 0$ and $y = 0$, and non-reflective (outwards flow) at $x = 1$ and $y = 1$. The speed chosen is given by $D_n = 1 - 0.1\kappa$. The problem is really one-dimensional where $\kappa = 1/r$. As $dr/dt = D_n$ then the speed function can simply be integrated to give

$$t^b_{\text{exact}}(x, y) = \sqrt{x^2 + y^2} - 0.2 + 0.1\ln(10\sqrt{x^2 + y^2} - 1), \tag{3.37}$$

where $\sqrt{x^2 + y^2} \geq 0.2$. The error is given by the L_1norm

$$E_1 = \sum_{i,\,j} \left| t^b_{\text{exact}} - t^b \right| \Delta^2, \tag{3.38}$$

and the time step is chosen to be 0.8 of the maximum allowed by equation (3.36). The numerical order of accuracy, R^c, is given by the gradient of the line in figure 3.2, i.e.

$$R^c = \frac{\ln(E_\Delta / E_{\Delta/2})}{\ln 2}. \tag{3.39}$$

The same results as Aslam, Bdzil and Stewart (1996) are achieved and second-order convergence is demonstrated (figures 3.1 and 3.2, table 3.1).

3.4 Implementation for SNe Ia with DSD

The modification and implementation of the level set method for SN Ia problems is next described. The coordinate system is axisymmetric cylindrical (r, z). The relationship between cartesian and cylindrical coordinates is

$$r = \sqrt{x^2 + y^2}, \tag{3.40}$$

$$\theta = \arctan\left(\frac{y}{x}\right), \tag{3.41}$$

$$z = z, \tag{3.42}$$

and

$$x = r\cos\theta, \tag{3.43}$$

$$y = r\sin\theta, \tag{3.44}$$

$$z = z. \tag{3.45}$$

Using the chain rule, the derivatives become

$$\frac{\partial}{\partial x} = \cos\theta\frac{\partial}{\partial r} - \frac{\sin\theta}{r}\frac{\partial}{\partial\theta}, \tag{3.46}$$

$$\frac{\partial}{\partial y} = \sin\theta\frac{\partial}{\partial r} + \frac{\cos\theta}{r}\frac{\partial}{\partial\theta}, \tag{3.47}$$

$$\frac{\partial}{\partial z} = \frac{\partial}{\partial z}. \tag{3.48}$$

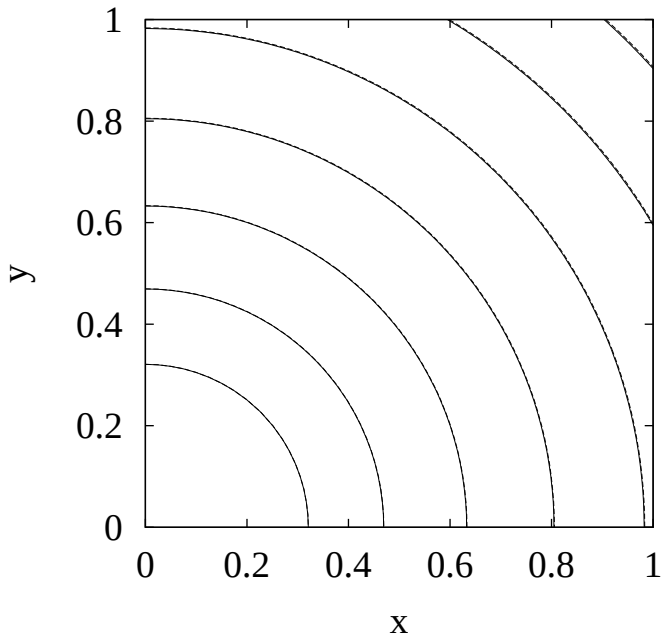

Figure 3.1: Solutions t^b_{exact} (solid line) and t^b for $\Delta = 1/40$ (dashed line).

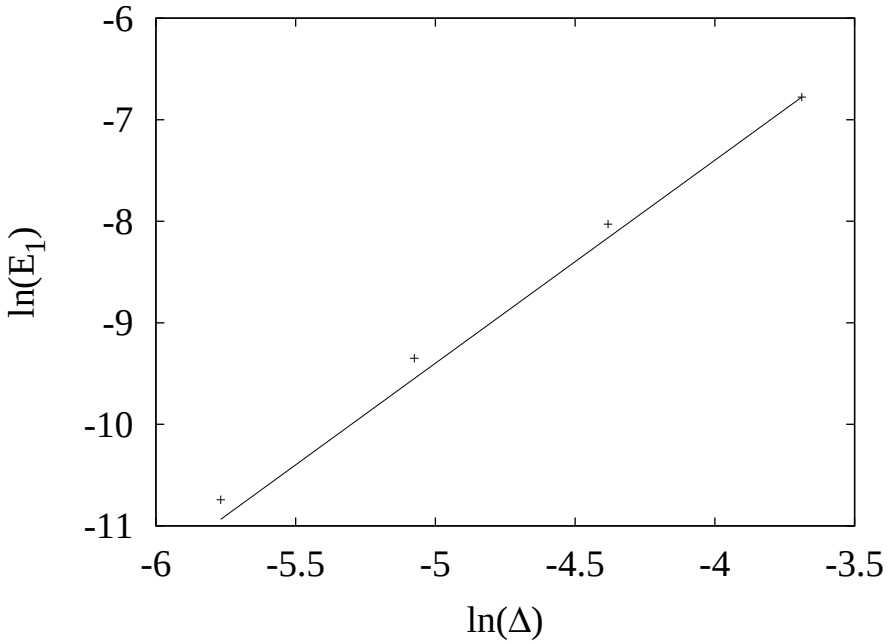

Figure 3.2: Numerical error as a function of step size for the test problem. The line through the point $\Delta = 1/40$ has a slope of 2.

Δ	E_1	R_c
1/40	1.14×10^{-3}	
1/80	3.26×10^{-4}	1.81
1/160	8.70×10^{-5}	1.91
1/320	2.16×10^{-5}	2.01

Table 3.1: Error and numerical accuracy for the test problem.

The unit vectors are related through

$$\hat{\mathbf{x}} = \cos\theta\hat{\mathbf{r}} - \sin\theta\hat{\boldsymbol{\theta}}, \tag{3.49}$$

$$\hat{\mathbf{y}} = \sin\theta\hat{\mathbf{r}} + \cos\theta\hat{\boldsymbol{\theta}}, \tag{3.50}$$

$$\hat{\mathbf{z}} = \hat{\mathbf{z}}. \tag{3.51}$$

Substitution into the laplacian yields

$$\nabla = \frac{\partial}{\partial r}\hat{\mathbf{r}} + \frac{1}{r}\frac{\partial}{\partial\theta}\hat{\boldsymbol{\theta}} + \frac{\partial}{\partial z}\hat{\mathbf{z}}. \tag{3.52}$$

As the coordinate system is axisymmetric there is no θ dependence ($\partial/\partial\theta = 0$), then

$$|\nabla\psi| = \left(\psi_r^2 + \psi_z^2\right)^{1/2}. \tag{3.53}$$

The second derivatives are obtained from

$$\frac{\partial^2}{\partial x^2} = \left(\cos\theta\frac{\partial}{\partial r} - \frac{\sin\theta}{r}\frac{\partial}{\partial\theta}\right)\left(\cos\theta\frac{\partial}{\partial r} - \frac{\sin\theta}{r}\frac{\partial}{\partial\theta}\right), \tag{3.54}$$

$$\frac{\partial^2}{\partial y^2} = \left(\sin\theta\frac{\partial}{\partial r} + \frac{\cos\theta}{r}\frac{\partial}{\partial\theta}\right)\left(\sin\theta\frac{\partial}{\partial r} + \frac{\cos\theta}{r}\frac{\partial}{\partial\theta}\right), \tag{3.55}$$

$$\frac{\partial^2}{\partial z^2} = \frac{\partial^2}{\partial z^2}, \tag{3.56}$$

then

$$\nabla^2 = \frac{\partial^2}{\partial r^2} + \frac{1}{r}\frac{\partial}{\partial r} + \frac{1}{r^2}\frac{\partial^2}{\partial\theta} + \frac{\partial}{\partial z^2}. \tag{3.57}$$

The mean curvature in this coordinate system then becomes

$$\kappa = \frac{\psi_{rr}\psi_z^2 - 2\psi_r\psi_{rz}\psi_z + \psi_r^2\psi_{zz}}{\left(\psi_r^2 + \psi_z^2\right)^{3/2}} + \frac{\psi_r}{r\sqrt{\psi_r^2 + \psi_z^2}}. \tag{3.58}$$

The forms of the previous equations are simply transformed by $x \to r$ and $y \to z$ and the curvature has an extra term which is also calculated through central differences.

The density is specified at each node from either linearly interpolated data or a polynomial

fit depending upon the model and labelled as either C-O or He. Any node which has a density below that of the data range, the density is set to the minimum density data value (for C-O and for He). The lowest density values for which there are data are $\log_{10}\rho_0 = 4.5$ and 5.4 g cm^{-3} for He and C-O respectively. This will affect the planar detonation speed assumption but not the DSD version as at the low densities the extinction curvature is small and the front will be extinguished. The density drops very rapidly at the edge of the star i.e. Fink et al.'s (2010) model before the He detonation. The density drops by six orders of magnitude over a distance of about 8×10^6 cm. As the density is then known at each node, a value for the planar speed (figure 2.5), sound speeds (figure 2.16) and extinction curvature when the front is completely extinguished is known (figures 2.12 and 2.14). The curvature of ψ can be worked out from equation (3.58) with central differences and then the curvature and density are known at this point allowing α to be found out from bilinear interpolation on a surface consisting of $D_n - \kappa$ curves. As the $D_n - \kappa$ curves terminate at various final extinction curvatures depending upon density, to make interpolation easier, curvature is scaled with the extinction curvature, so $\bar{\kappa} = \kappa/\kappa_{\text{extinction}}$. If the curvature of ψ is negative, then the planar speed is used and $\alpha = 0$.

Reflective boundary conditions are employed along the z-axis and outwards flow for the three other boundaries. Care must be taken along the z axis with the second term in equation (3.58) as $r = 0$. The boundary condition here is reflective and therefore $\psi_r = 0$ as well. To consider the limit, $\psi_r \sim r\psi_{rr}$ when r is small, thus

$$\lim_{r\to 0} \frac{\psi_r}{r\sqrt{\psi_r^2 + \psi_z^2}} = \frac{\psi_{rr}}{|\psi_z|}. \tag{3.59}$$

If a Von Neumann analysis is performed just for the parabolic part of the level set equation along the z-axis, then firstly the level set equation with a linear D_n simplifies to

$$\psi_t = 2\alpha\psi_{rr}. \tag{3.60}$$

This goes to

$$\exp(a\Delta t) = 1 + \frac{2\alpha\Delta t}{\Delta^2}\left[\exp(ik_m\Delta) - 2 + \exp(-ik_m\Delta)\right], \tag{3.61}$$

which simplifies to

$$\exp(at) = 1 + \frac{4\alpha\Delta t}{\Delta^2}\left[\cos(k_m\Delta) - 1\right], \tag{3.62}$$

and then

$$\exp(a\Delta t) = 1 - \frac{8\alpha\Delta t}{\Delta^2}\sin^2(k_m\Delta/2). \tag{3.63}$$

As

$$\left|1 - \frac{8\alpha\Delta t}{\Delta^2}\sin^2(k_m\Delta/2)\right| \leq 1, \tag{3.64}$$

then this is satisfied if

$$\frac{4\left|\alpha\right|\Delta t}{\Delta^2} \leq 1. \tag{3.65}$$

This is the three-dimensional time step restriction given in Aslam, Bdzil and Stewart (1996). This is expected as the curvature represents mean curvature in three-dimensional axisymmetric cylindrical coordinates. Therefore, the complete time step restriction will depend on the two-dimensional restriction for the hyperbolic part (as simply $x \rightarrow r$ and $y \rightarrow z$), and the three-dimensional restriction for the parabolic part, i.e. for a nonlinear D_n

$$\frac{2D_{\text{planar}}\Delta t}{\Delta} + \frac{4\max\left(\left|\partial\alpha/\partial\kappa\right|\right)\Delta t}{\Delta^2} \leq 1, \tag{3.66}$$

or

$$\Delta t \leq \frac{\Delta^2}{2\left[D_{\text{planar}}\Delta + 2\max\left(\left|\partial\alpha/\partial\kappa\right|\right)\right]}. \tag{3.67}$$

3.4.1 Speed Function

Three $D_n - \kappa$ curves for various densities were shown in chapter 2. The lower density curves have large absolute values for the gradient of α. The time step is dependent on the gradient of D_n. Taking $\log\rho_0 = 6.0$ for C-O as an example, then $\max(|\partial\alpha/\partial\kappa|) = 2.26 \times 10^{26}$ cm^2 s^{-1}. Looking at equation (3.67), either the mesh step size must be very large or the time step very small. In the former the resolution would be inadequate, whereas the latter would be impractical. A typical white dwarf radius is $O(10^8)$ cm, then with a value of $\Delta = 10^6$ cm

for 101 points from 0 to 10^8 cm gives the time step restriction as $\Delta t \leq 1.1 \times 10^{-15}$ s for $\log_{10} \rho_0 = 6.0$ in C-O. This occurs however when the curvature is $O(10^{-17})$ cm^{-1}, requiring a radius of curvature far greater than that of a typical white dwarf. The front would propagate at the sound speed (as an inert shock) and hence is only hyperbolic. The time step restriction for $\log_{10} \rho_0 = 9.0$ with the same Δ is $\Delta t \leq 3.8 \times 10^{-4}$ s . There is also the problem of when the sonic point moves from one branch to another for certain densities and branches. There is a sudden drop in the original curves (e.g moving from O to C burning) and formally this is an infinite gradient. As points on ψ move across branches on the $D_n - \kappa$ curves this can cause instability and destroy the solution.

Overcoming this problem is accomplished by refitting the curves at points where the gradient exceeds a certain value. A limit can be chosen on Δt, called $\Delta t_{\max}$, and for a specified Δ a limit on $|\partial\alpha/\partial\kappa|$ is obtained. Starting at the data point at the extinction curvature and working backwards to the planar speed, the gradient at each point is compared to this limit. If found to be greater than this limit the point is refit making the gradient here equal to the limit. Although the low densities will be smoothed more, for the lowest densities this is not an issue. The extinction curvature will be smaller than the detonation front curvature ($O(10^{-8})$ cm^{-1}) and here only the sound speed is relevant. It is important therefore to ensure the region of curvature relevant to the problem is smoothed as little as possible for the densities where the detonation is not extinguished. The main disadvantage of smoothing can be seen in figure 3.3. If the curvature is negative and then the planar speed is assumed, this will be less than its actual value. The larger $\Delta t_{\max} = 10^{-3}$ s has smoothed the curve too much. The curvature region of interest (where the shock is expected to be a detonation, not inert) and planar speed are below their original values. For $\Delta t_{\max} = 10^{-6}$ s the difference between the actual value and the smoothed planar speed is only approximately 4 per cent. The curve is not smoothed for curvatures greater than $\log_{10} \kappa = -10$ cm^{-1}. A small artificial transition region can be seen between C and O burning.

3.4.2 Post Processing

When the burn table is obtained, post processing can be undertaken to obtain the reaction lengths and sonic point locations. The curvature of the burn table field is the same as the curvature of the front at that location and is obtained from $\kappa = \nabla(\nabla t^b / |\nabla t^b|)$. Then as

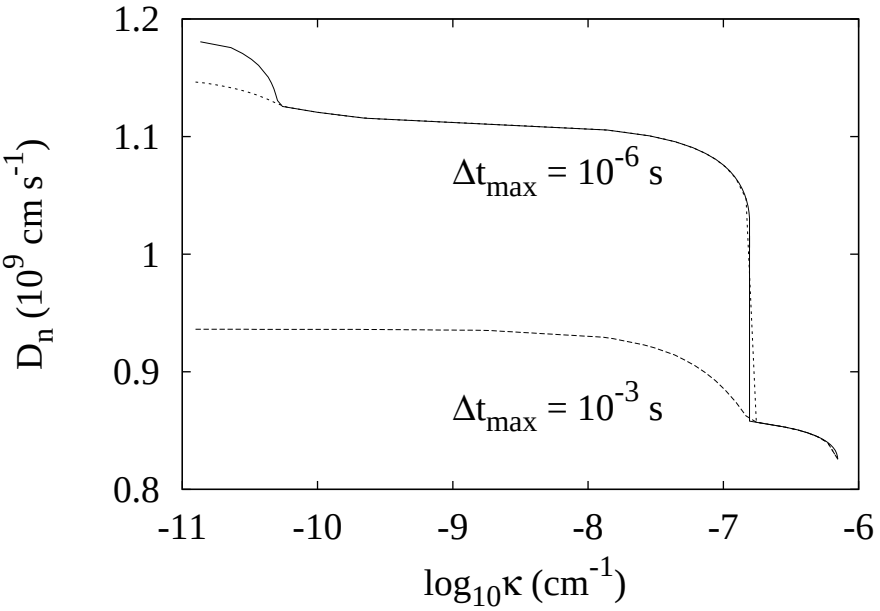

Figure 3.3: $D_n - \kappa$ curve for C-O $\log_{10}\rho_0 = 6.6$ illustrating the effect of smoothing for two values of $\Delta t_{\max}$ with $\Delta = 10^6$ cm. The solid line represents the unsmoothed curve.

curvature and density are known at each node, the reaction lengths, sonic point locations and detonation speeds can be found through bilinear interpolation of data.

3.4.3 Test Problem

The above criteria allows a suitable Δ to be chosen, fixed and then a suitable $\Delta t_{\max}$ chosen. Smaller values of Δ are preferred but this will impose an impractical Δt. The values of $\Delta = 10^7$, 5×10^6 and 2.5×10^6 cm are chosen, which for a domain of 10^8 cm give 11, 21 and 41 nodes respectively . Next, a suitable Δt needs to be chosen. There are two points to consider as previously described:-

- If there is negative curvature and the planar speed is assumed, then the smoothed planar speed must not deviate too much from its original value. It is preferable however to keep it close to its original value.

- The region of the curve of interest must not be smoothed. The curvatures expected to be encountered will be 10^{-8} to 10^{-9} cm^{-1} as the radius of the star is $O(10^8)$ cm.

Addressing the first point, negative curvature will be encountered in the C-O of Case A near the interface and in the He shell at the south pole of Fink et al.'s Model 2. The minimum C-O

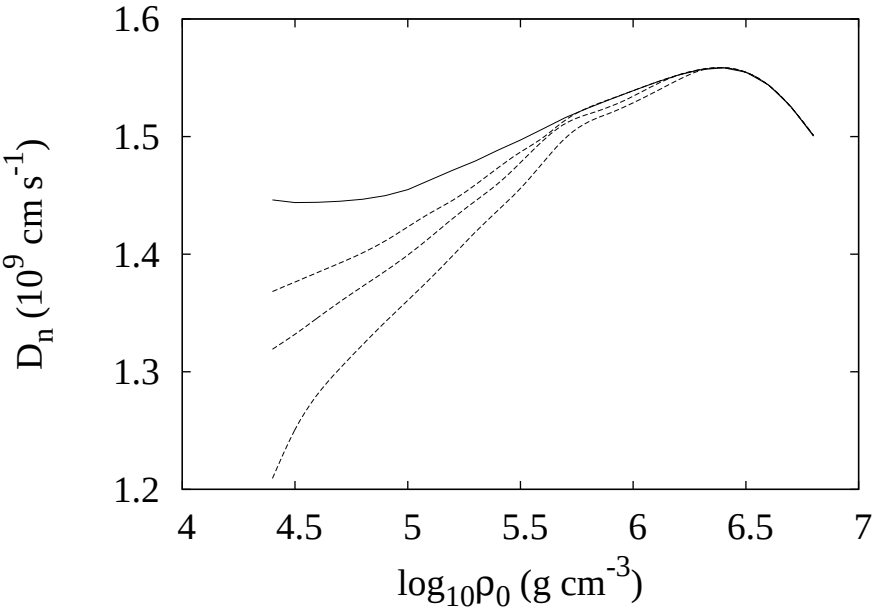

Figure 3.4: Smoothed planar speeds in He. The solid line is the actual values. The dashed lines represent the smoothed values with $\Delta t_{\max} = 10^{-7}$ s. The lowest is for $\Delta = 2.5 \times 10^6$ cm, the middle $\Delta = 5 \times 10^6$ cm and the top is $\Delta = 10^7$ cm.

density in Case A is $\log_{10} \rho_0 = 6.53$ g cm^{-3}. Using a $\Delta t_{\max} = 10^{-7}$ s, with $\Delta = 2.5 \times 10^6$ cm, the planar speed of $\log_{10} \rho_0 = 6.5$ g cm^{-3} is only 6 per cent below its actual value. Figure 3.4 shows the He planar speeds with the same $\Delta t_{\max}$. Although the planar speed is considerably less than its actual value at low densities, the detonation will be extinct. The extinction curvature for $\log_{10} \rho_0 = 5.3$ g cm^{-3} is 10^{-8} cm^{-1}. The second point is satisfied with this same value.

A test problem is described next to make sure the level set method has been adapted correctly for DSD implementation in SNe Ia and to choose a suitable value of Δ. Wiggins (1993) fits a polynomial to the density profile of Case A. The test problem will be based on the polynomial of Case A. The polynomial is

$$\log_{10} \rho_0 = a r_8^2 + b r_8 + c, \tag{3.68}$$

where $a = -1.1133 \times 10^{-1}$, $b = -0.125$ and $c = 8.02$ and $r_8 = r/10^8$ and the interface is at 3.136×10^8 cm. Case A is originally detonated off centre. However, to obtain a solution to which the DSD version can be compared, Case A will be detonated centrally with an initial radius of 4×10^7 cm. This initial radius was chosen to ensure minimal error associated with

an initial front of comparable size to the mesh size (see next subsection). This allows a known 'exact' solution to be obtained through numerical integration of $dR_s/dt = D_n(\rho_0, \kappa)$ with $\kappa = 2/R_s$. This solution does not require the $D_n - \kappa$ curves to be smoothed and is useful with which to compare. The integration is computed until the front becomes extinct.

The result of the centrally detonated test problem with one of the Δs is shown in figure 3.5. There is very good agreement for the lowest Δ, especially at an earlier time. The agreement between the numerical and exact solutions is even better for smaller Δs. Case A is next detonated off-centre as in Wiggins and Falle (1997) to check off-centre detonation. This solution can not be compared with an analytical or similar solution. However, the solutions can be compared between themselves. The detonation is a point on the z axis at $z = 3.165 \times 10^8$ cm. These results are shown in figure 3.6. The cusp is smoothed for the largest Δ (10^7 cm, dashed line), especially for $t = 0.24$ s compared to the smaller Δs. Although the agreement with the larger Δ is reasonable at an early time, it does fall behind as time progresses. The two smallest Δs agreement, especially when the detonation is not extinct, is very good. The larger of the two only falls behind at a later time when the detonation is extinct and is not important to the results. The suitable values to use therefore will be $\Delta = 5 \times 10^6$ cm.

3.4.4 Ignition Kernel

The starting spot is known as the ignition kernel. It seems unlikely a detonation will start from a point in SNe Ia. The curvature would be too large. It therefore seems hot spots are more likely to form and then ignite. Seitenzahl et al. (2009) investigated the critical sizes of hot spots which could lead to a detonation. These critical radii depend upon the density and background temperature. Higher densities have smaller critical radii because the reaction rate is related to the number density of the reactants. The reactants burn faster and the length scales are shorter. Increasing the temperature also reduces the critical radii due to the faster reaction rates. These critical radii have larger values of curvature, which by the $D_n - \kappa$ curves, should be extinct. However, the $D_n - \kappa$ curves are solutions to a quasi-steady problem. When a detonation initially forms it is unsteady. One must therefore consider time dependence at the time of detonation formation. DSD can take into account time dependence at higher order (Bdzil and Aslam 2000). The question of the hot spot and detonation formation is beyond the scope of this thesis. The focus is on the qualitative affects between the planar assumption

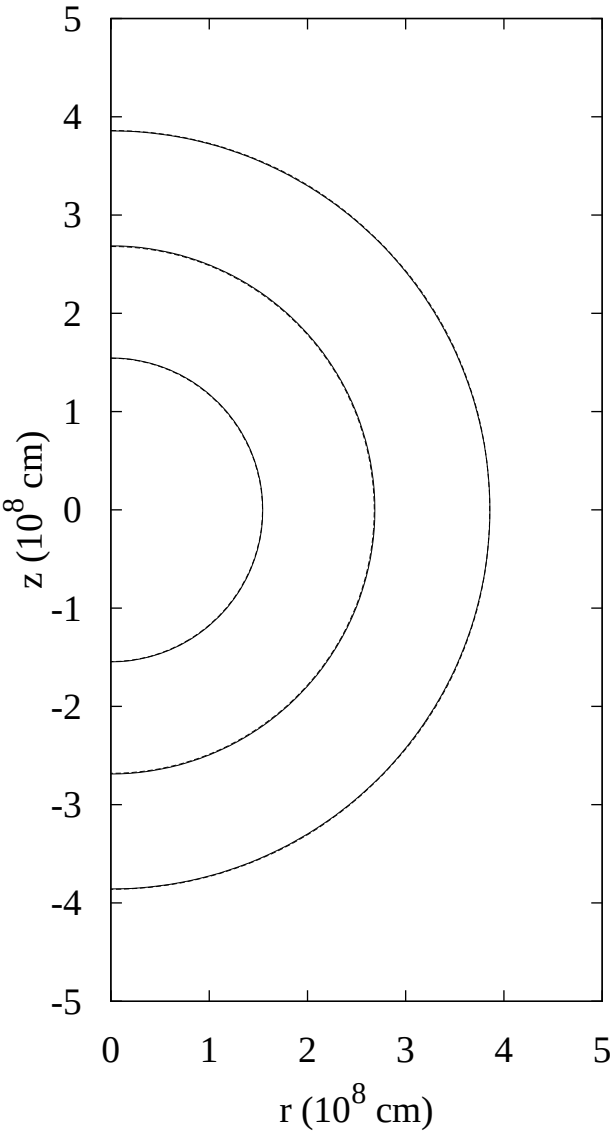

Figure 3.5: Case A centrally ignited test problem for the level set method with SNe Ia. The times are at 0.1, 0.2 and 0.3 s. The solid line represents the exact solution, the dashed line for $\Delta = 10^7$ cm.

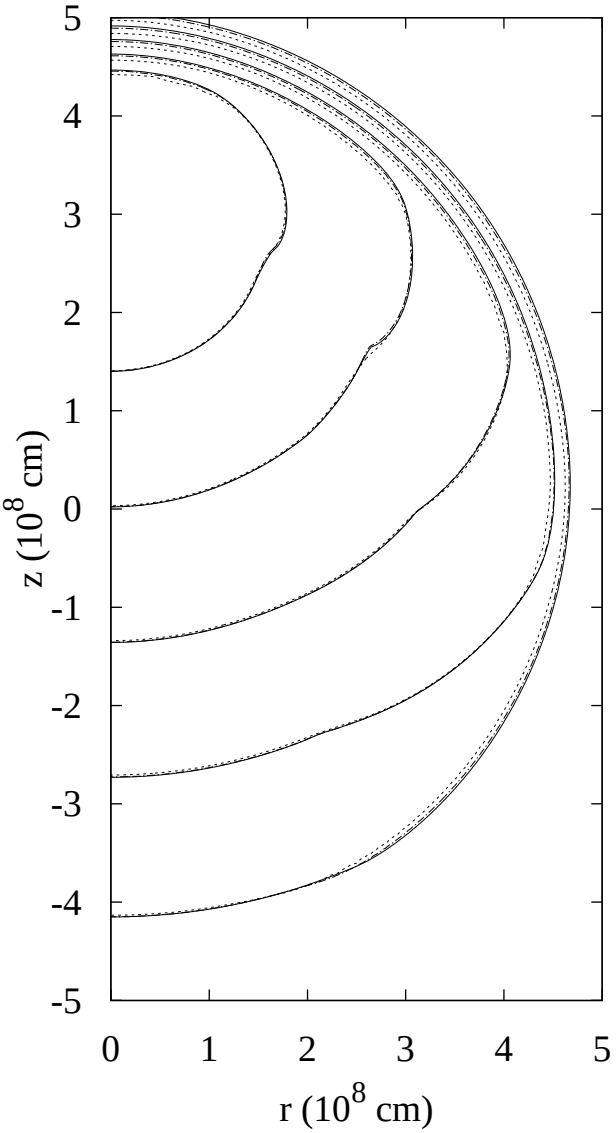

Figure 3.6: Case A off-centre ignited test problem for the level set method with SNe Ia. The times are 0.12, 0.24, 0.36, 0.48 and 0.6 s. The values $\Delta = 10^7$, 5×10^6 and 2.5×10^6 cm are represented by dashed, dot-dashed and solid lines respectively.

and taking into account curvature. The radius of the hot spot will be four times that of the resolution, i.e. 2×10^7 cm. A minimum of four nodes within the radius of the initial front is used to model terrestrial explosives (Hodgson 2013). If the initial hot spot is comparable to the mesh size, i.e. one cell, the initial front is a diamond shape, not circular. This can cause large errors with comparison to an analytical solution.

3.5 Summary

The level set method has been introduced and explained. The numerical implementation of the method was described and then applied to a simple test problem. This was then adapted for SNe Ia and DSD. Finally, it should be noted that while only one-dimensional (spherically symmetric) and two-dimensional (axisymmetric, single point initiation) will be considered in the next chapter, SN Ia scenarios from the literature, DSD methods and their level set implementations are specifically constructed to be readily extendible to three dimensions and to naturally account for multiple wavefronts from multiple initiation sources, the interactions and merging of disconnected fronts, etc. (Bdzil and Stewart 2007).

Chapter 4

Application and Results

The level set method is applied to various SN Ia detonation scenarios in this chapter. In each case the front dynamics are computed first by assuming that the detonation propagates at the local planar detonation speed e.g. Wiggins and Falle (1997). Henceforth this is referred to as the PDS model. This is then compared with detonation shock dynamics propagation according to the $D_n - \kappa$ assumptions (referred to as the DSD model). The purpose here is to investigate the qualitative changes in the predictions of SN Ia detonation models when curvature effects are taken in to account. These results have also been published in Dunkley, Sharpe and Falle (2013) with a different Δ, $\Delta t_{\max}$ and initial starting front size.

The detonation speeds in the DSD model will be compared to the PDS through the velocity deficit, v_d, defined as

$$v_d = 1 - (D_n - c_f)/(D_{\text{planar}} - c_f). \tag{4.1}$$

When the front is close to the planar speed, the velocity deficit will be near zero and 1 when extinguished (the front is travelling at the frozen sound speed). This planar speed refers to the actual planar speed, rather than the one that may be reduced due to the smoothing discussed in the previous chapter. There is an artificial transition region as well due to smoothing between the speed at the extinction curvature and the sound speed. However, the velocity deficit will be set to 1 if in a node the curvature is greater than the extinction curvature.

A useful characteristic of the star with which to compare the reaction lengths is the density scale height, L_ρ, defined as

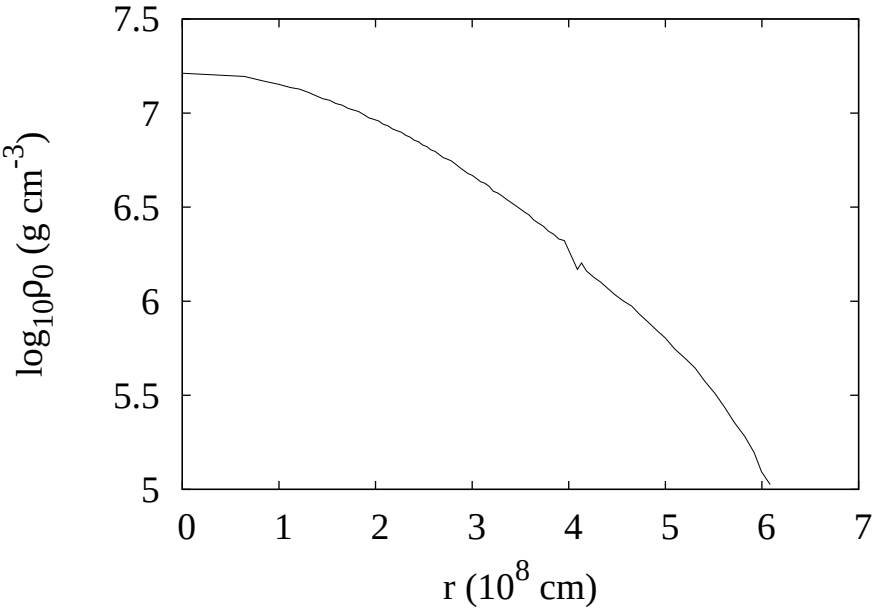

Figure 4.1: Density profile for Woosley and Weaver's (1994) Model 2 prior to ignition of the first stage off-centre He detonation.

$$L_\rho = \rho / \left| \nabla \rho \right| . \tag{4.2}$$

This will be compared to the reaction lengths in the form $\log_{10}(L/L_\rho)$ where L is the effective distance (or reaction length) between the sonic point and front ($l_{\rm planar}$ for the PDS and l for DSD). If the reaction lengths become greater than the density scale height then this becomes greater than 0. The sonic point locations will also be compared.

4.1 Spherically Symmetric Models

4.1.1 Woosley and Weaver's Model 2

Firstly one of Woosley and Weaver's (1994) one-dimensional (spherically symmetric) models is investigated. They discuss a case (referred to as Model 2 in their paper) in particular detail. Model 2 consists of a 0.7 $M_\odot$ white dwarf which accretes 0.2 $M_\odot$ of He. A He detonation starts at the base of the accreted He ($r = 3.95 \times 10^8$ cm) and propagates outwards. The density just before the helium ignites is shown in figure 4.1. In this model the He detonation

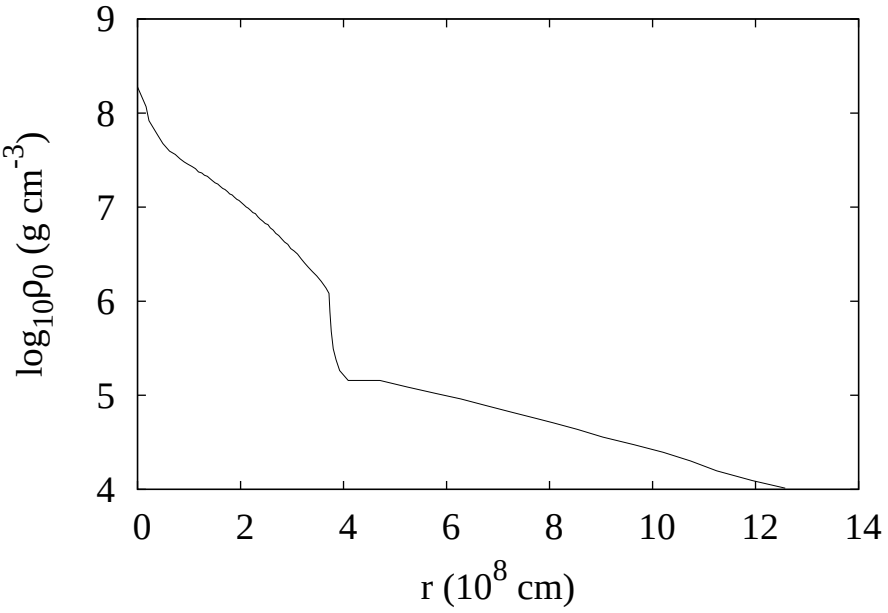

Figure 4.2: Density profile for Woosley and Weaver's (1994) Model 2 at the time of central ignition of the second stage C-O detonation.

is initiated simultaneously at every point of the base in the He shell. The He detonation also results in an inert shock which travels inwards towards the core, compressing the C-O matter. This inert shock converges in the C-O at the centre and the resulting density profile is shown in figure 4.2. The C-O then ignites centrally, resulting in a detonation propagating outwards.

In the spherically symmetric case, the shock radius, R_s, is related to the detonation speed, D_n, in the shock normal (radial) direction, x, by

$$\frac{dR_s}{dx} = D_n(\rho_0, \kappa), \tag{4.3}$$

while the front curvature is simply $\kappa = 2/R_s$ (for the PDS case the detonation speed is simply $D_{\rm planar}(\rho_0)$). Equation 4.3 can be solved by an appropriate numerical integration. Given the front position, the density is determined from the density profile in Woosley and Weaver (1994) (figures 4.1 and 4.2). Woosley and Weaver give their densities as a function of the interior mass, M, in units of the solar mass, $M = m/M_\odot$, where m is the mass in grams. As $\rho = dm/dV$ and $dV = 4\pi r^2 dr$ from the equation for the volume of a sphere, then this gives

$$M_{\odot} dM = 4\pi\rho r^2 dr. \tag{4.4}$$

This equation can be rearranged and integrated which leads to

$$r = \left(\frac{3M_{\odot}}{4\pi} \int_0^M \frac{1}{\rho(M')} dM' \right)^{1/3}. \tag{4.5}$$

4.1.1.1 He Detonation

The results are shown in figures 4.3 to 4.5 for the first stage He detonation. Both solutions diverge from one another almost at the start as the front propagates (figure 4.3). As the detonation progresses and the curvature of the shock decreases (increasing R_s), the lower densities ahead of the detonation cause the effects of curvature to rapidly increase. Consequently the difference between the speeds of the two versions is significant (figure 4.4). Assuming planar propagation in the PDS model results in He detonation reaction lengths which are always orders of magnitude greater then the density scale height (figure 4.5) which is inconsistent. The planar speed assumption necessitates complete burning, yet the reactions would also not complete in the time scale required. However, note that the quasi-steady, quasi-one-dimensional assumptions of DSD are almost entirely self-consistent in this case. Curvature of the shock front affects the sonic point significantly, driving it inwards, so that the length of the subsonic driving zone remains mostly below the density scale height. Although the reaction lengths become comparable to the density scale height just before the front is extinguished, this happens at the end and is only transient. The detonation front is extinguished at $R_s = 5.99 \times 10^8$ cm ($\log_{10} \rho_0 = 5.1$ g cm^{-3}).

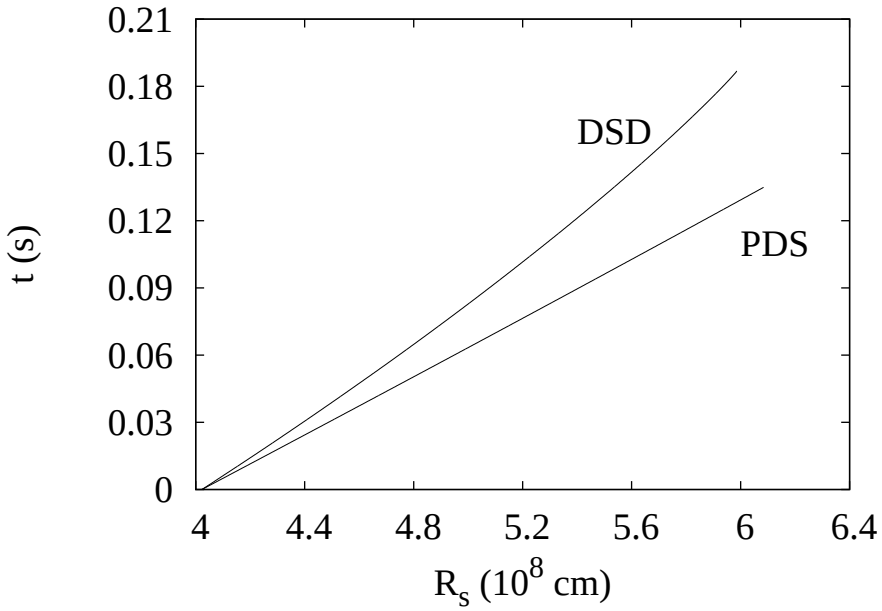

Figure 4.3: Model 2 He detonation: Detonation time as a function of shock radius.

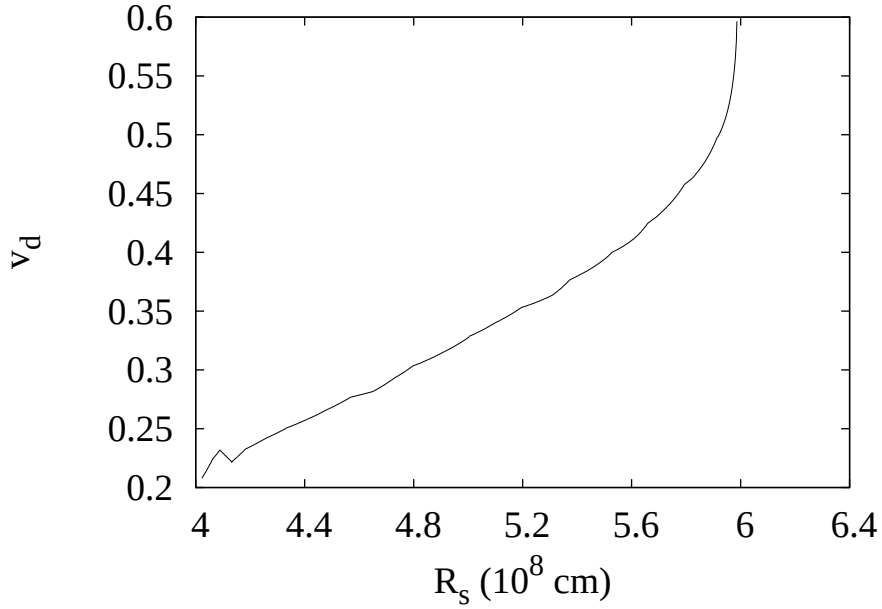

Figure 4.4: Model 2 He detonation: Velocity deficit as a function of shock radius.

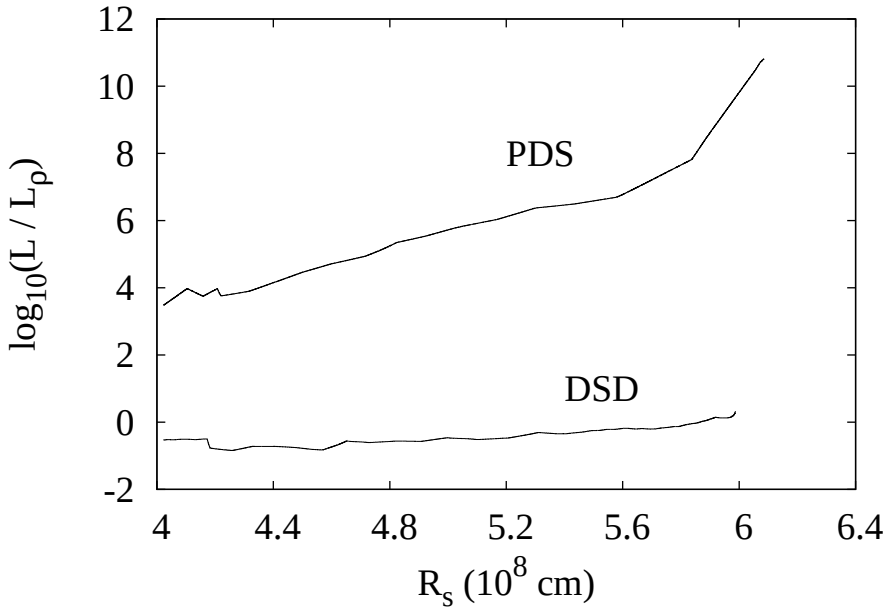

Figure 4.5: Model 2 He detonation: Driving reaction length (distance between the front and sonic point) over the density scale height as a function of shock radius.

4.1.1.2 C-O Detonation

For the second stage of Model 2, the C-O detonation is followed from ignition at the centre up to where the C-O ends and the burnt products of the He detonation start at $r = 3.72 \times 10^8$ cm (figure 4.2, here $t = 0$ s is now the time of central ignition). The conditions up to the point of the C-O detonation were created by a hydrodynamic evolution induced by the He detonation stage and realistically the fuel would be moving. However, since the detonation propagation is very high for most of its propagation in the core (i.e. approximately five times or more than the sound speed) the hydrodynamics state ahead of the detonation can be considered to be frozen. Furthermore, the flow velocities ahead of the front will be less than the detonation speed so that again this effect can be neglected to leading order. The contribution of flow velocities to the level set speed function if desired, can be solved with simple upwind schemes (Sethian 1999).

The results for this stage are shown in figures 4.6 to 4.8. Curvature effects are not significant around the centre as the density is relatively high, hence initially the PDS and DSD models give similar results. The sonic point is at the end of oxygen burning (i.e. on the O branch) due to the wave being pathological. The detonation is no longer pathological at

0.11 s ($R_s = 1.41 \times 10^8$ cm, $\log_{10} \rho_0 = 7.30$ g cm^{-3}) and the sonic point jumps to the end of Si burning as the curvature is low in relation to the extinction curvature for the densities encountered there. However, this is only a brief period and the sonic point transitions back to the O branch solution at 0.12 s ($R_s = 1.63 \times 10^8$ cm, $\log_{10} \rho_0 = 7.21$ g cm^{-3}) as curvature effects start to become more important. The detonation speed in DSD becomes noticeably less than that of the PDS since the PDS sonic point then remains at the end of Si burning. The turning point of the O branch is subsequently reached at 0.24 s ($R_s = 2.95 \times 10^8$ cm, $\log_{10} \rho_0 = 6.58$ g cm^{-3}), beyond which the solution drops down to the branch corresponding to the sonic point at the end of C burning. The DSD version does not reach the interface of the C-O with the burnt products of the first stage. The curvature induced detonation extinction point corresponding to the turning point of the C branch is encountered just before the arrival at the interface at 0.32 s ($R_s = 3.58 \times 10^8$ cm, $\log_{10} \rho_0 = 6.20$ g cm^{-3}). The entire C-O core is detonated in the PDS model as there is no extinction mechanism. In fact, the PDS model becomes inconsistent at around 0.21 s ($R_s = 2.5 \times 10^8$ cm, $\log_{10} \rho_0 = 6.82$ g cm^{-3}) due to the planar detonation reaction length scales required for complete burning under the PDS assumption becoming greater than the density scale height (figure 4.8). The DSD model remains more self-consistent however, since curvature induces the driving zone length to remain smaller than the density scale height. The maximum value the reaction length attains is 6.2×10^6 cm, located just before the front is extinguished, which is far below the value of the density scale height ($L_\rho = 3.6 \times 10^8$ cm).

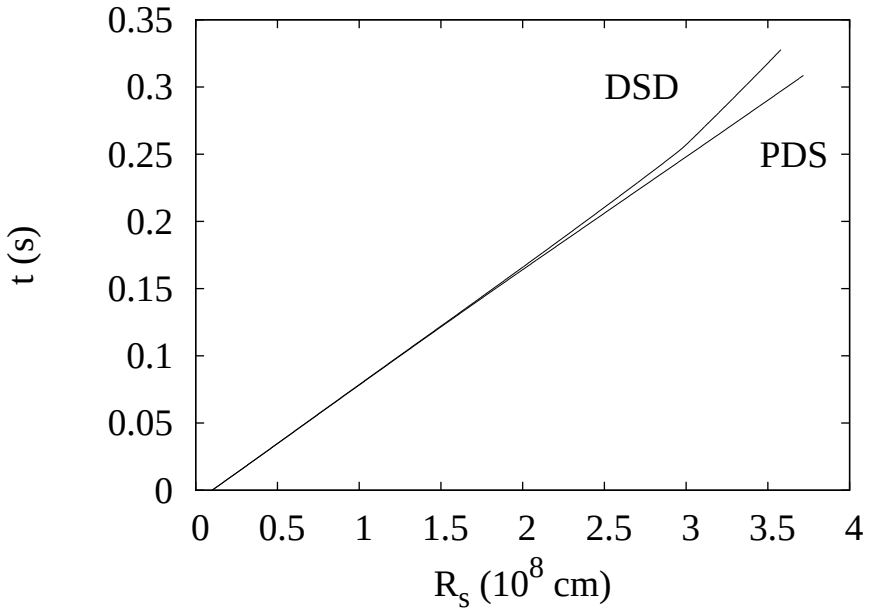

Figure 4.6: Model 2 C-O detonation: Detonation shock radius as a function of time.

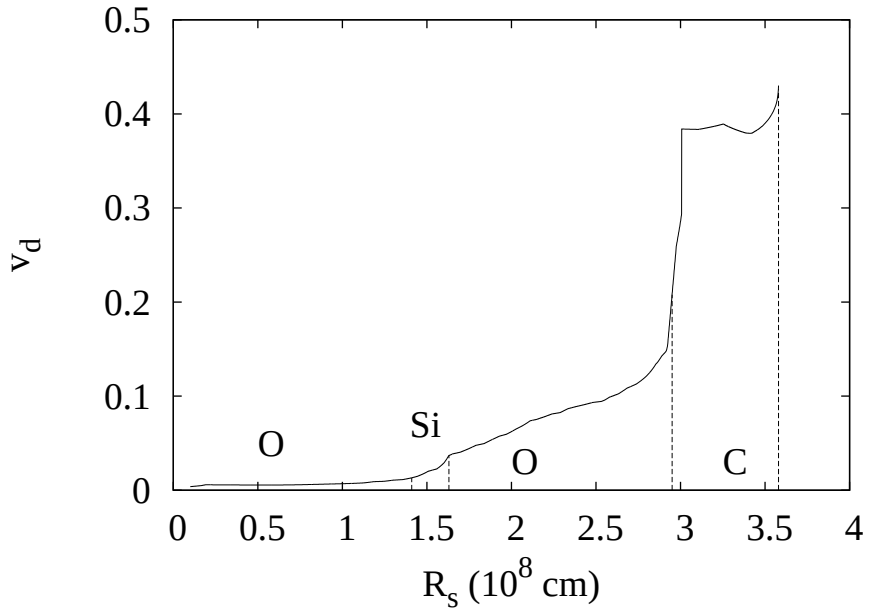

Figure 4.7: Model 2 C-O detonation: Velocity deficit as a function of shock radius. DSD regimes of propagation are marked by dashed lines where Si, O and C refer to the $D_n - \kappa$ solution branch in C-O.

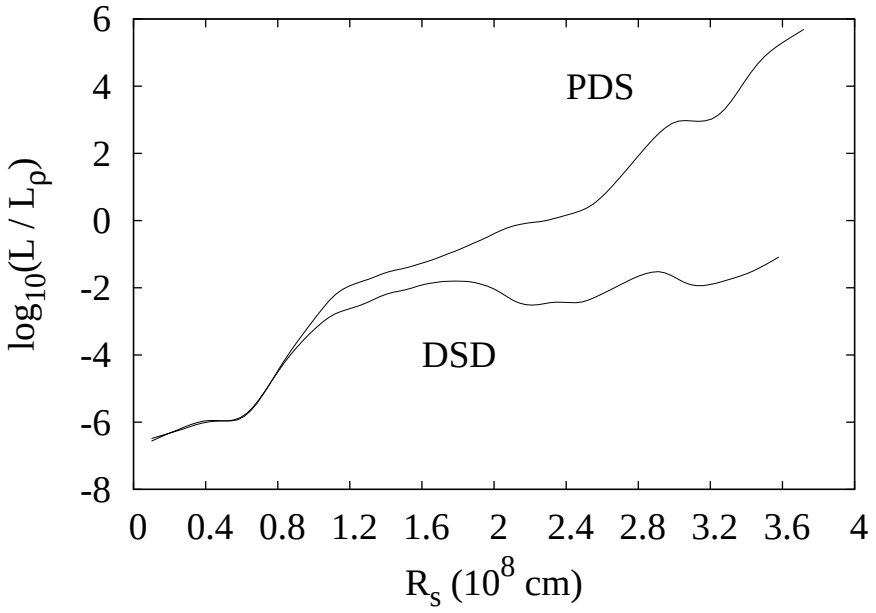

Figure 4.8: Model 2 C-O detonation: Driving reaction length (distance between the front and sonic point) over the the density scale height as a function of shock radius.

4.2 Off-centre Models

This section considers the effects of curvature on two-dimensional (axisymmetric) models.

4.2.1 Nomoto's Case A

Case A was investigated by Nomoto (1982b) in one dimension as a spherically symmetric model (similar to the previous model). He accretes onto the C-O core and eventually a He shell flash occurs, forming a detonation wave. Figure 4.9 shows the density profile of the white dwarf at the time of ignition. This is the polynomial from the end of chapter 3, fitted by Wiggins (1993). Nomoto (1982b) investigates Case A and finds it produces a detonation wave at the base of the He shell. This He detonation propagates outwards, which, unlike Woosley and Weaver's (1994) Model 2 above, simultaneously drives a detonation wave in the C-O core. This is known as a double-detonation model due to the two detonation waves. A two-dimensional version of Case A, corresponding to a point ignition source rather than ignition of the entire base of the shell, was subsequently investigated by Wiggins and Falle (1997). They used a subgrid model involving geometric optics to pre-compute the evolution of the detonation waves under the PDS assumption. The detonation is ignited at $r = 3.17 \times 10^8$

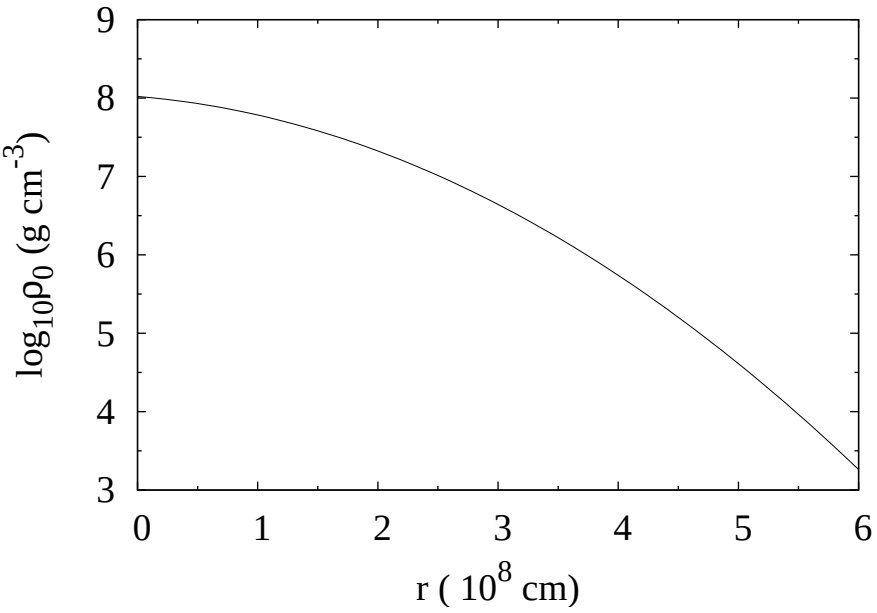

Figure 4.9: Density profile for Case A.

cm, just above the interface at $r = 3.14 \times 10^8$ cm ($\log_{10} \rho_0 = 6.51$ g cm^{-3}), in this case. They found that two cusps form on the wavefront in the core due to the faster driving He detonation and suggest that these cusps may have important implications for nucleosynthesis.

The level set evolution of the double detonation Case A model is similar to Wiggins and Falle's (1997) geometric optics construction results, i.e. in which the detonation wavefront has two cusps (figure 4.10) . The He detonation is faster than the detonation in the C-O, leading to a cusp forming by the interface. The other is interior to the core and is a consequence of the dependence of the planar detonation speed on the local density. It takes 0.51 s for the C-O core to be completely detonated. Figure 4.11 shows the DSD version of the evolution when curvature effects are taken in to account. Curvature acts to smooth cusps or corners due to its parabolic (smoothing) nature (Sethian 1999). The transit time of the detonation through the core of 0.54 s is only slightly longer than that of the planar case, since the detonation speed is close to the planar values in a large part of the core.

Figure 4.12 shows the velocity deficit. The speed in the centre of the core is very close to that of the PDS version (the black region). The speed is less than the PDS version in the outer regions of the core as curvature effects are more dominant at lower densities. The speed is near the PDS version close to the negative curvature region due to the curvature being small due to the (smoothed) cusp and hence is travelling at the planar speed adjacent to the interface. The curved detonation speeds in the relatively low density He shell are significantly

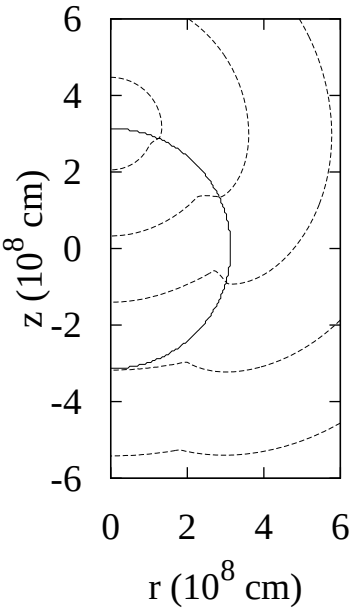

Figure 4.10: Case A: Wave front at times 0.06, 0.21, 0.36, 0.51, and 0.66 s (dashed lines), according to the PDS. The solid line is the interface.

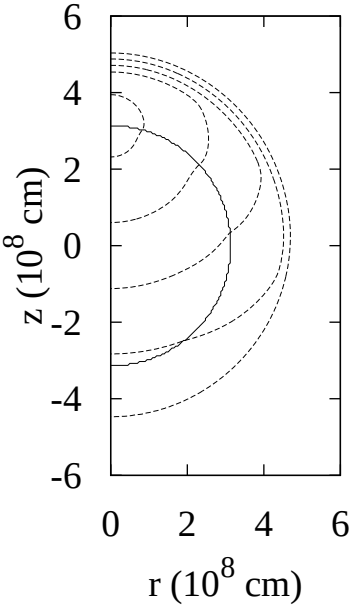

Figure 4.11: Case A: Wave front at times 0.06, 0.21, 0.36, 0.51, and 0.66 s (dashed lines), according to DSD. The solid line is the interface.

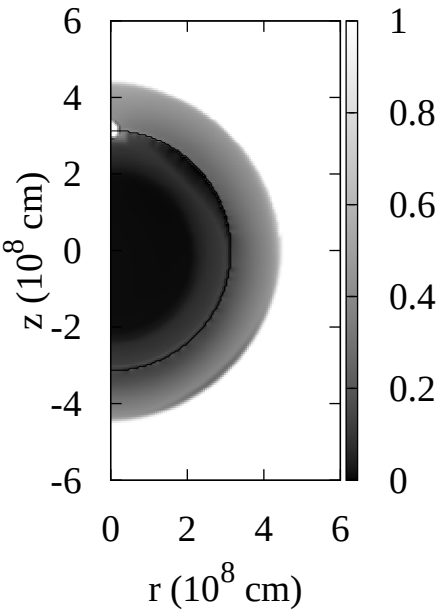

Figure 4.12: Case A: Greyscale of the velocity deficit. The solid line is the interface.

below the planar values, hence the He detonation's driving effect is not as strong compared to the planar case. Indeed, the curvature is sufficiently high in the outer parts (above a radius of about 4.4×10^8 cm, corresponding to $\log_{10} \rho_o = 5.32$ g cm^{-3}) of the He shell to extinguish the detonation completely.

Figure 4.13 shows the $D_n - \kappa$ solution branch on which the detonation front propagates. Near the ignition 'point', the front curvature is very large and the densities are relatively low, there is a small transition region where the solution lies on the C branch. In the inner regions of the core nearer the centre the detonation travels close to the planar configuration due to the relatively high densities. Since for these densities the planar wave is pathological, here the solution evolves on the O branch (sonic point near the end of oxygen burning). Further out from the centre of the star, there is a narrow region around the centre corresponding to the planar wave solution becoming near CJ. In this region curvature effects are still relatively weak such that the sonic point remains near the end of Si burning (the evolution is governed by the Si branch dynamics). This region is broader towards the south pole of the star as the curvature is less here than at the region towards the north pole. However, moving further out, as the densities become lower, curvature effects rapidly become more important and

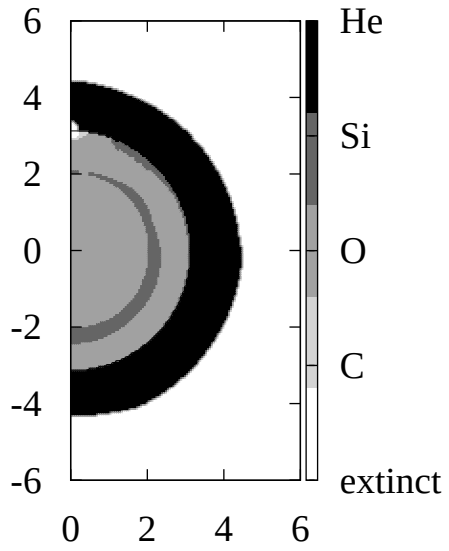

Figure 4.13: Case A: DSD regimes of propagation: C, O and Si refer to the solution branch of the $D_n - \kappa$ evolution in C-O, He refers to a propagating curved detonation in the shell and Extinct refers to the outer shell region where curvature has quenched the He detonation. The interface between the C-O core and He shell is represented by the solid line.

are sufficient to drive the solution beyond the turning point of the Si branch, back onto the O branch. Hence in this region the detonation speed and structure become significantly different from the planar wave. Finally, adjacent to the interface in the northern hemisphere, the curvature becomes negative due to the He detonation initially driving the core detonation at the interface. In this narrow region, as the curvature decreases to zero, the solution again is driven back up to the Si branch. However, the He detonation driving effect diminishes as it travels around the core and becomes more curved and hence decelerates. The curvature of the C-O detonation near the interface becomes positive and sufficiently high that it is driven off the Si branch in this region as it travels. This region of negative curvature becomes thinner.

In the core, the planar driving reaction zone lengths are less than the density scale height for densities higher than $\log_{10} \rho_0 = 7$ g cm^{-3}, corresponding to the distance of 2.5×10^8cm or less from the centre of the star (figure 4.14). The dark region in the centre of figure 4.14 is due the wave being pathological. The reaction zone lengths are very small compared to the density scale height. Further out than this, the driving zone length of the planar detonation becomes

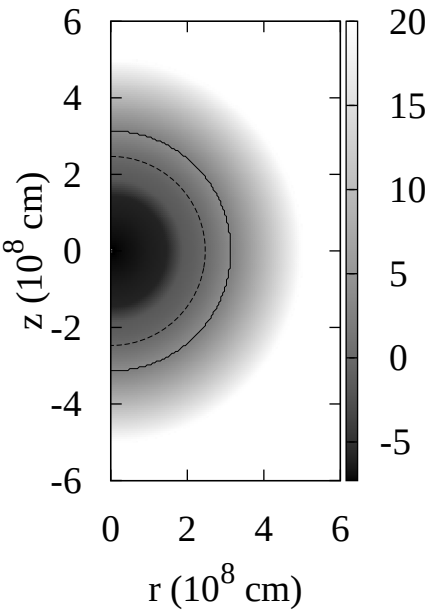

Figure 4.14: Case A: Effective reaction length compared to the density scale height with a contour of zero (dashed line) for the PDS version. The solid line is the interface.

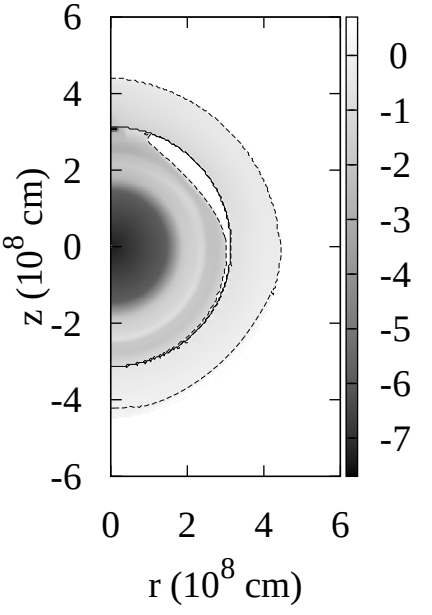

Figure 4.15: Case A: Effective reaction length compared to the density scale height with a contour of zero (dashed line) for the DSD version. The solid line is the interface.

larger than the density scale height, and hence the assumption of complete burning breaks down. Therefore in this region the PDS model is not consistent. Indeed, in the core just before the interface, these lengths are some three orders of magnitude greater than the density scale height. The planar version also breaks down completely in the He. The reaction lengths are always larger than the density scale height (for the lowest densities the He detonation length is more than 18 orders of magnitude greater than the density scale height). However, in the core, apart from the narrow region adjacent to the interface labelled Si in figure 4.13 in the DSD version, the driving reaction zone lengths of the curved waves are always much less than the density scale height and hence the DSD model is self-consistent here (figure 4.15). In the narrow region mentioned above, due to the negative and near zero curvatures, this is likely to be unsteady, in particular where the curvature is negative at the interface, and hence a full time-dependent simulation will be required to determine the details of this part of the solution. However, since this region is small, it is not expected to have a large effect. The DSD driving reaction lengths in the He are less than the density scale height until near the end of the detonation propagation. This is due to the reaction lengths of the lower density He being longer along with the decreasing curvature. However, this region where the reaction lengths are greater than the density gradient is towards the end of the detonation propagation. As before in the C-O for negative curvature, this would require a full time-dependent simulation. The largest values here are under ten orders of magnitude greater than the density scale height.

4.2.2 Fink et al.'s Model 2

The next case considered is by Fink et al. (2010). They investigated whether a He detonation can later trigger a detonation in the C-O core in sub-Chandrasekhar mass white dwarf explosions. They also used level set methods to compute the propagation of the detonations in both He and C-O, under the PDS assumption. They considered one case (Model 2) in detail. In this model, the He is ignited at a point just above the base of the He envelope (at $z = 4.64 \times 10^8$ cm). Initially only the He detonated and the wave propagated around the core and drove a shock wave into it. The shock front converged inside the core at an off-centre point. Fink et al. found this convergence results in ignition of the C-O at this point, producing a detonation which propagated outwards and consumed the C-O. The density profiles of

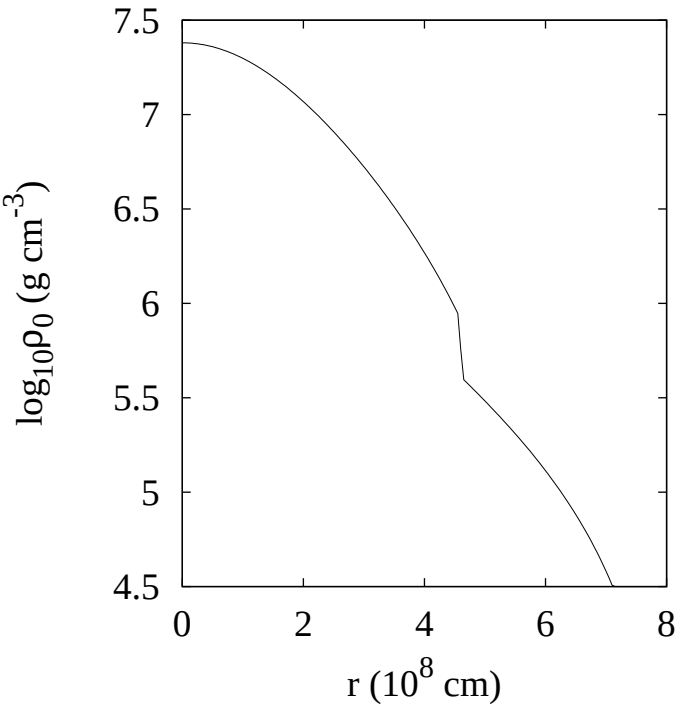

Figure 4.16: Density profile for Fink et al.'s model 2 before the first stage He detonation

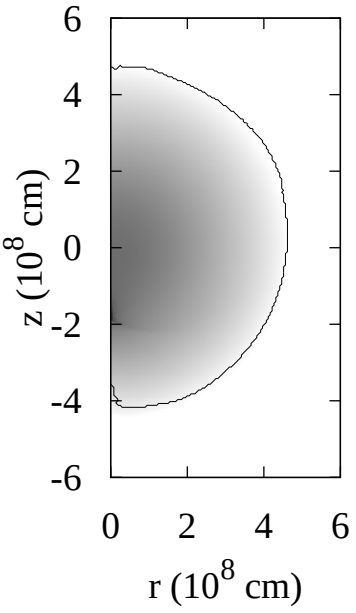

Figure 4.17: Density profile for Fink et al.'s model 2 before second stage C-O detonation. The scale goes from $\log_{10} \rho_o = 5.57$ g cm^{-3}, the minimum value in the core (white) to $\log_{10} = 8.13$ g cm^{-3} (black), the maximum. The solid line represents the interface.

the star at the time of ignition of the He and C-O detonations are shown in figures 4.16 and 4.17 respectively (Fink 2011).

4.2.2.1 He Detonation Stage

Figures 4.18 and 4.19 compare the wavefront arrival times for the PDS and DSD versions respectively, for the He detonation stage of Model 2. In the evolution according to the PDS model, there is a cusp on the interface and the detonation front takes 1.9 s for the He wave to propagate all the way around the core and converge on the axis of symmetry on the opposite side of the core to the point of ignition ($z = -2.22 \times 10^8$ cm). In contrast, the DSD version takes 2.64 s to converge on the z axis at $z = -4.3 \times 10^8$ cm, indicating the significant effects of curvature in this case. The He detonation wave is sensitive to curvature in the low densities encountered in the shell and hence travels much slower than its planar version. Further out in the He envelope, due to low density it takes only a relatively small curvature to drive the detonation to extinction. In this region therefore the He does not detonate. The ignition kernel at $t = 0$ was the same for both the PDS and DSD cases, but figures 4.20 to 4.21 show that near the point of ignition, the front propagates as an inert wave and can only turn in to a detonation when the curvature becomes sufficiently small for the DSD case. In other words a larger ignition kernel is required. Even then when the front ignites, the detonation region is confined to a thin strip adjacent to the interface with the core, becoming wider as the front travels and the curvature decreases. When the front becomes a detonation, some of the nodes adjacent to the interface are unresolved due to the cusp on the interface of the inert core and this results in incorrect high curvatures. Using a smaller Δ (and Δt) is impractical. However, this is secondary to the important results of the qualitative differences between the DSD and PDS results and this numerical error disappears as the detonation progresses and the front is smoothed in this region. It is reasonable to label these nodes as He for the DSD regimes of propagation (instead of the incorrect extinct) and obtain v_d and the reaction lengths from averaging correct adjacent values. Note that in the PDS case, there is no mechanism for extinguishing the detonation and hence the entire shell is predicted to detonate and hence this is qualitatively incorrect.

The planar reactions lengths in this model vary from 10^{15} to 10^{28} cm, i.e. many orders of magnitude larger than the density scale height of the star. The assumption of planar

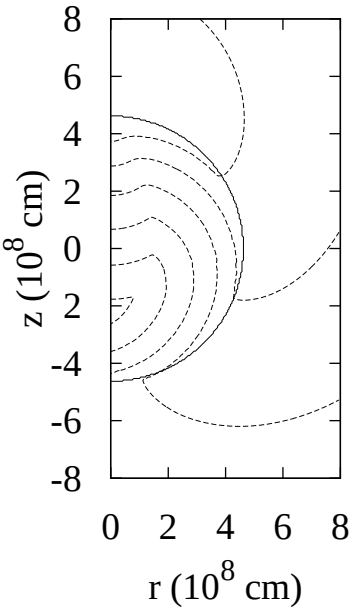

Figure 4.18: Model 2 He detonation: wavefront at times 0.3 , 0.6, 0.9, 1.2, 1.5 and 1.8 s (dashed lines), according to the PDS. The interface between the C-O core and He shell is represented by the solid line.

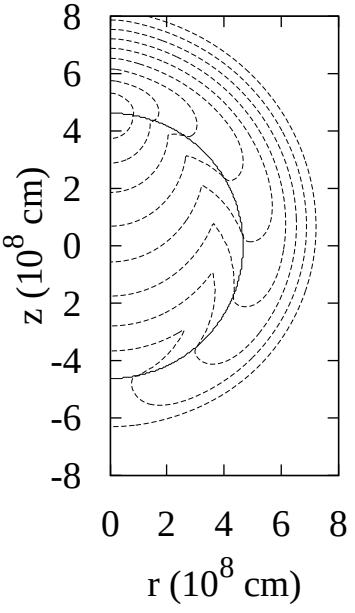

Figure 4.19: Model 2 He detonation: wavefront at times 0.3 ,0.6, 0.9, 1.2, 1.5, 1.8, 2.1, 2.4 and 2.7 s (dashed lines), according to DSD. The interface between the C-O core and He shell is represented by the solid line.

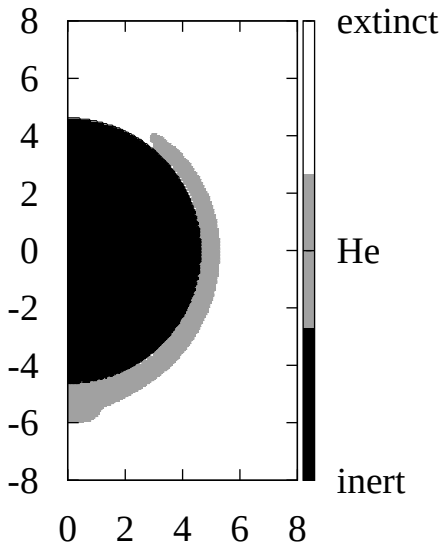

Figure 4.20: Model 2 He detonation: DSD regimes of propagation. He refers to the propagating curved detonation the shell, inert refers to the inert core and extinct refers to the outer shell region where curvature has quenched the He detonation. The interface between the C-O core and He shell is represented by a solid line.

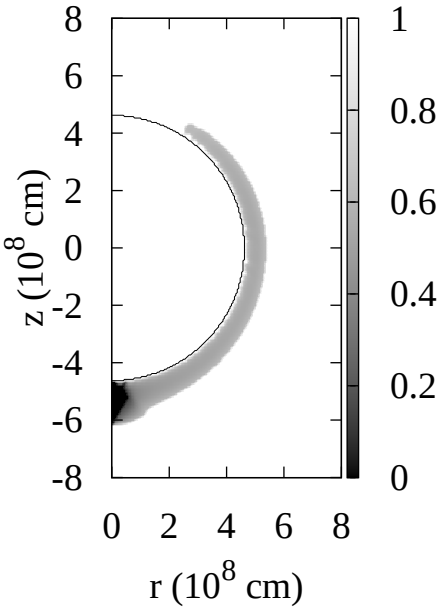

Figure 4.21: Model 2 He detonation: Greyscale of the velocity deficit. The solid line is the interface. The black region around the south pole shows where the curvature is negative and the speed is set to its planar values.

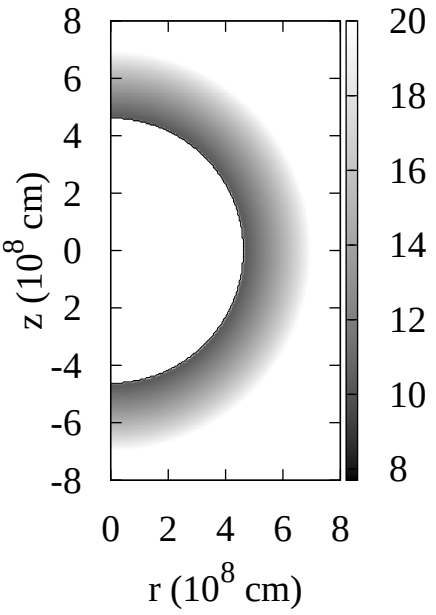

Figure 4.22: Model 2 He detonation: Effective reaction length compared to the density scale height for the PDS version. The interface between the C-O core and He shell is represented by a solid line

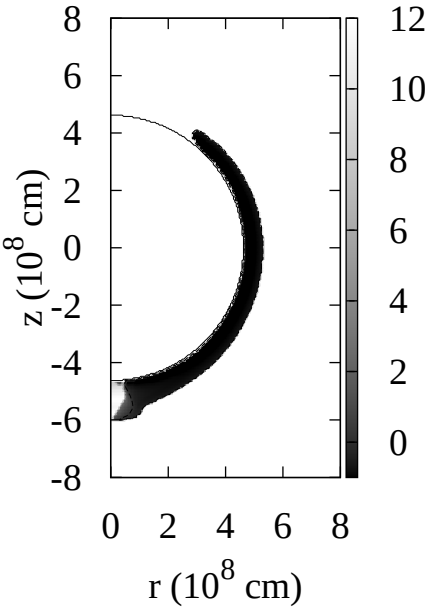

Figure 4.23: Model 2 He detonation: Effective reaction length compared to the density scale height with a contour of zero (dashed line) for the DSD version. The interface between the C-O core and He shell is represented by a solid. line

detonation propagation is completely invalid at any point of the evolution for this case (figure 4.22). However, taking into account curvature, for the part of the He shell which detonates according to the DSD model, the driving zone length scales are typically 10^5 to 10^7 cm. These scales are much less than the density scale height (figure 4.23). The DSD assumptions break down however, near the end of the detonation of the shell due to the total curvature of the front becoming negative – note that due to axi-symmetry the front is converging or imploding towards the axis and hence the cylindrical component of curvature becomes increasingly large and negative. DSD breaks down for negative curvatures (Bdzil and Stewart 2007) and hence PDS evolution has been assumed when $\kappa < 0$. This final stage of the evolution requires a full time-dependent simulation to resolve. However, as it is only a relatively small part of the evolution near the end, it should not affect the conclusions.

4.2.2.2 C-O Detonation Stage

Next the C-O detonation phase of Fink et al.'s (2010) Model 2 is considered. It should be noted however, as seen above, taking into account curvature the He precursor detonation propagation is qualitatively different to that predicted by the PDS as employed in Fink et al. (2010). This may dramatically affect the compression and expansion waves driven into the C-O core by the He detonation, and hence the core detonation ignition and evolution will take place under quite different conditions than in Fink et al.'s C-O configuration. While they find the C-O detonation stage is initiated due to sufficient compression in the core, the lower He DSD detonation speeds may not lead to C-O ignition. However, to compute the core structure at the time of ignition (if this occurs) will require a coupled hydrodynamic evolution of the core with the curved He detonation front evolution, which is beyond the current work. Hence here the consequences of curvature effects on the core detonation for Fink et al.'s (2010) original model are considered and compared with the PDS results. Figures 4.24 and 4.25 show the wavefront arrival times for both the PDS and DSD versions, respectively. It takes 0.6 s in the PDS version for the wave to travel through the entire C-O core. Due to the low densities, curvature is found to extinguish the detonation entirely in a significant band of material adjacent to the boundary with the detonated He envelope material for the DSD version. The entire detonation is extinct by 0.52 s in this version and the front subsequently propagates through the remaining core as an inert wave.

Close to the centre of the star, the wavefront is close to its planar speed due to curvature effects being least important at the relatively higher densities found there, as seen in the velocity deficit (figure 4.27). In this region the sonic point is located at the end of oxygen burning (figure 4.26). As the detonation moves out to lower densities, the underlying wave becomes close to CJ and the curvature is not sufficient to drive the solution onto the O branch. Thus there is a narrow 'horse-shoe' shaped region of Si branch evolution with the speeds close to the planar assumption. Moving out further, the densities and curvatures become such that the solution is driven back onto the O branch and the speed drops. Further out still, there is a significant band where the solution is driven onto the C branch and the speed drops even more, before the wave finally becomes completely extinguished in the outer regions of the core, as described above.

While the driving reaction lengths increase dramatically for the PDS version as one moves outwards to lower densities, becoming larger than the density scale height at a radius of about $2.3 - 2.6 \times 10^8$ cm from the centre (figure 4.28), the DSD theory remains more self-consistent (figure 4.29). The curvature keeps the driving zone reaction lengths much smaller than the density scale height, especially as the extinction curvatures are approached. Even when the sonic point is near the end of Si burning, the driving reaction lengths are approximately 10 to 100 times less than the density scale height.

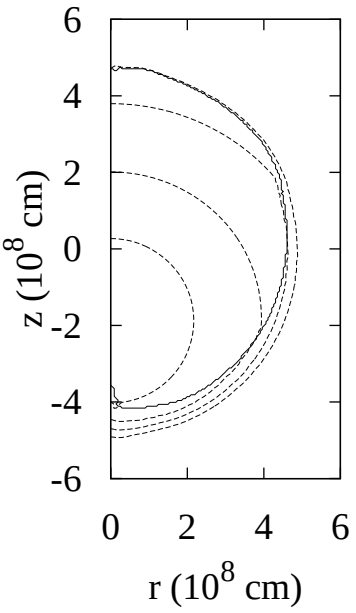

Figure 4.24: Model 2 C-O detonation : Wave front at times 0.15, 0.30, 0.45 and 0.6 s (dashed lines), according to the PDS model. The solid line is the interface.

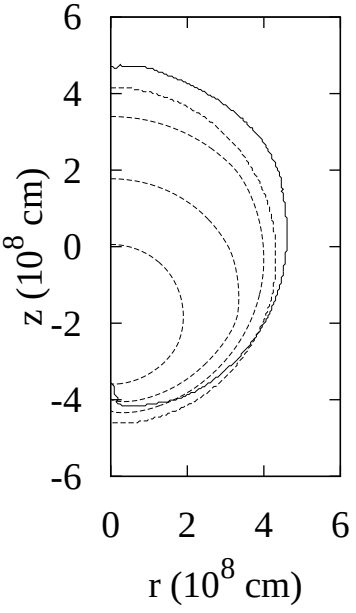

Figure 4.25: Model 2 C-O detonation stage results with wave front at times 0.15, 0.30, 0.45 and 0.6 s (dashed lines), according to the DSD model. The solid line is the interface.

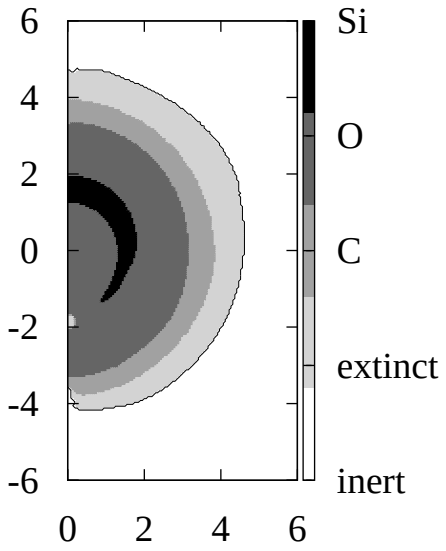

Figure 4.26: Model 2 C-O detonation: DSD regimes of propagation. C, O and Si refer to the solution branch of the $D_n - \kappa$ evolution in C-O, Extinct refers to regions where the curvature has quenched the C-O detonation. The interface between the C-O core and products of the He detonation is represented by the solid line

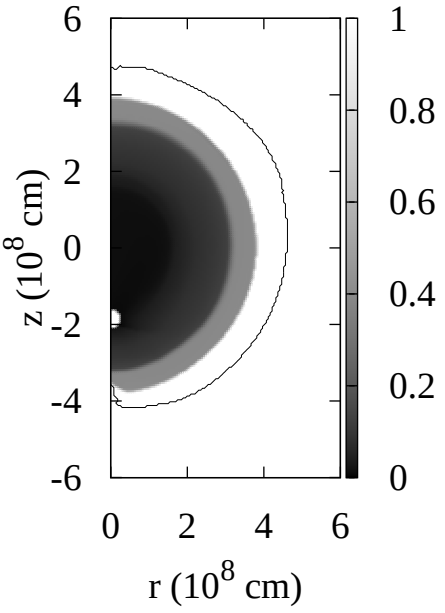

Figure 4.27: Model 2 C-O detonation: Velocity deficit. The interface between the C-O core and products of the He detonation is represented by the solid line.

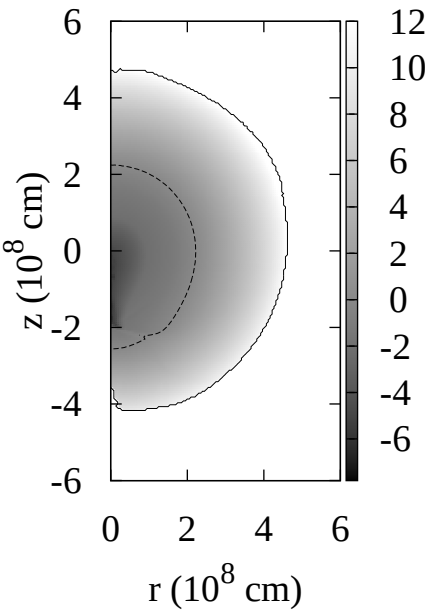

Figure 4.28: Model 2 C-O detonation: Effective reaction length compared to the density scale height with a contour of zero (dashed line) for the PDS version. The solid line is the interface.

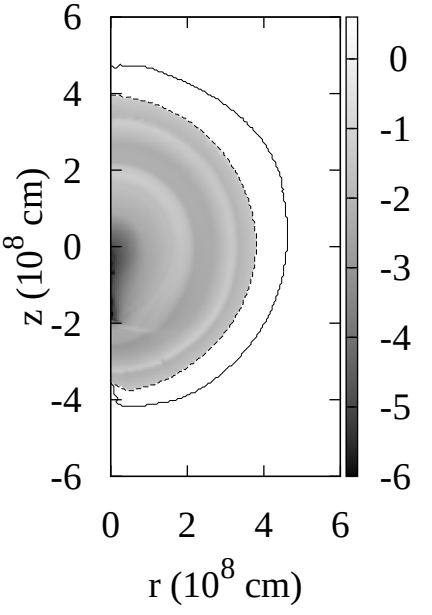

Figure 4.29: Model 2 C-O detonation: Effective reaction length compared to the density scale height with a contour of zero (dashed line) for the PDS version. The solid line is the interface.

4.2.3 Plewa's Y12 Delayed Detonation Model

Curvature of the front extinguishes the detonation for low densities, stopping these regions from detonating. The models above show that as the density decreases, curvature effects become increasingly important and the difference between the DSD and PDS versions become greater. The reaction lengths also increase and in the case of the PDS version, quite early on these can become comparable to the density scale height. In the DSD version, curvature keeps the reaction lengths shorter. The final case to be investigated is a very low density delayed detonation model of Plewa (2007). Plewa (2007) investigated detonating failed deflagration models, where an explosion happens after a quenched off-centre deflagration. Initially the star is burnt in a region around the centre during the deflagration phase. The majority of the energy goes into expanding the star. Small isolated shock-dominated regions are formed and prolonged compression leads to a detonation. One of Plewa's models in the paper, Y12, which ignites at a single point on the z-axis at $z = -2.55 \times 10^8$ cm, is considered here. There is a central area of C-O almost completely surrounded by the burnt material from the failed deflagration. There are pockets of C-O within this burnt material. Further out there is C-O material not ignited by the deflagration. Although there is a He shell surrounding the mixture of C-O and burnt material, it is far out (at a radius of the order of 10^9 cm) and the detonation front is extinct before this. Figure 4.30 shows the density field of the relevant region at the time of detonation ignition along with the material type in figure 4.31 (Plewa 2012).

Figures 4.32 and 4.33 compare the wave front evolution according to the PDS and DSD, respectively. Similar to before, the detonation propagates through the entire computational domain since there is no extinction limit in the PDS model. Initially for the DSD version, the wave propagates as a full detonation. The downwards propagating part of the detonation in figure 4.33 first reaches the burnt material at 0.1 s, at the point where the burnt material protrudes into the C-O at $r = 4 \times 10^7$, $z = -3.64 \times 10^8$ cm. All of the wave front in the central C-O region above a height of $z = -1.72 \times 10^8$ cm reaches the burnt (inert) material surrounding the central C-O as a detonation. On the z axis, the wavefront reaches this burnt material at 0.35 s. As the wavefront then passes through the burnt material, it emerges on the axis at 0.91 s as a C branch detonation with some other pockets similar to this one nearby. although this may be unlikely in practice. The extinction (or more appropriately, ignition) curvature for a shock that is initially inert, is less than the extinction curvature of a detonation

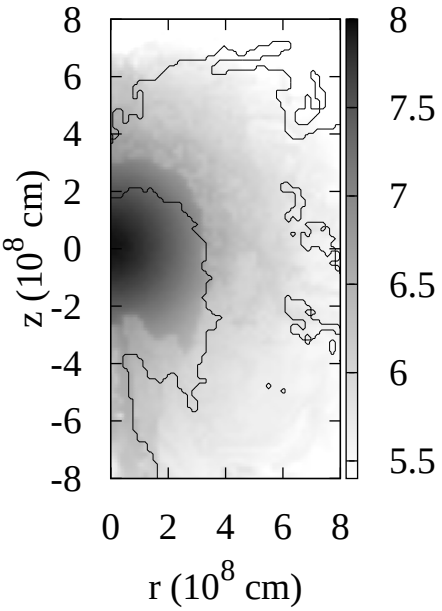

Figure 4.30: Density profile for Plewa's (2007) model. The interface between the unburnt C-O core and products of the C-O deflagration is represented by the solid line.

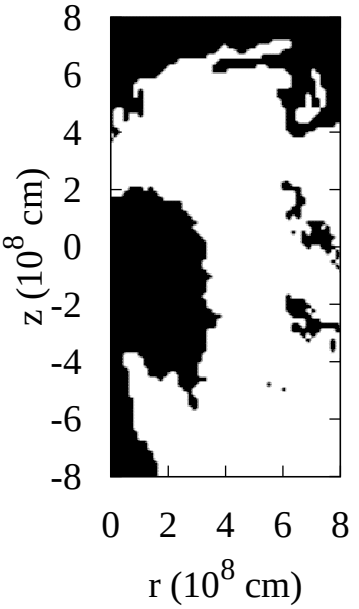

Figure 4.31: Material type for Plewa's (2007) model, where black is C-O, white is burnt.

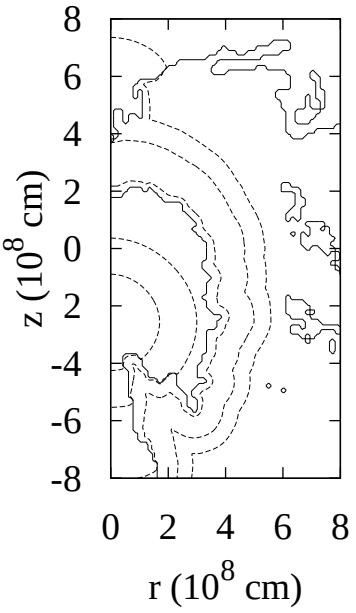

Figure 4.32: Y12 detonation: wave front at times 0.11, 0.22, 0.44, 0.88 and 1.21 s (dashed lines), according to the PDS. The interface between the C-O core and products of the C-O deflagration is represented by the solid line.

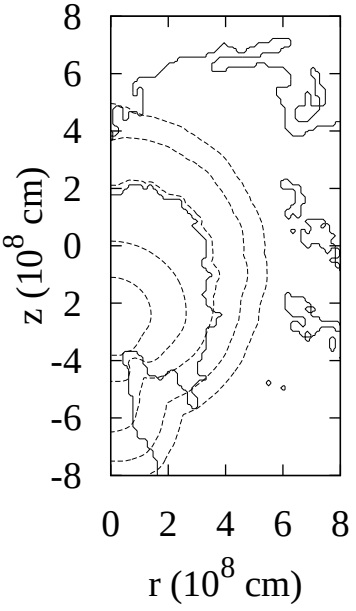

Figure 4.33: Y12 detonation: wave front at times 0.11, 0.22, 0.44, 0.88 and 1.21 s (dashed lines), according to DSD. The interface between the C-O core and products of the C-O deflagration is represented by the solid line.

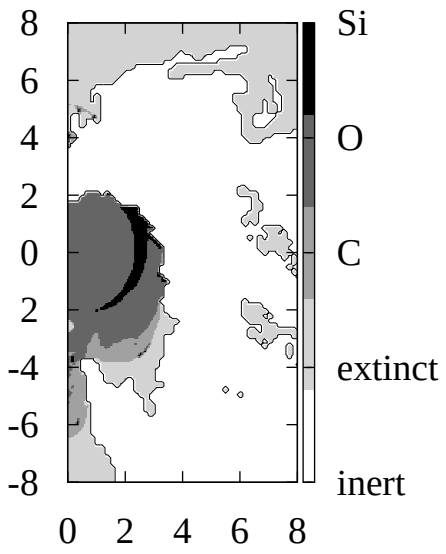

Figure 4.34: Y12: DSD regimes of propagation. The interface between the C-O core and products of the C-O deflagration is represented by the solid line.

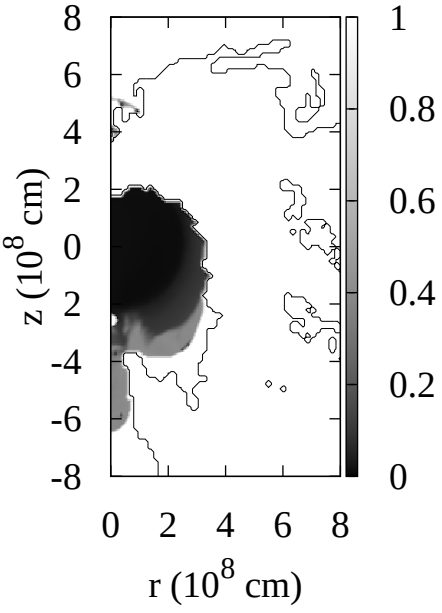

Figure 4.35: Y12: Velocity deficit. The interface between the C-O core and products of the C-O deflagration is represented by the solid line.

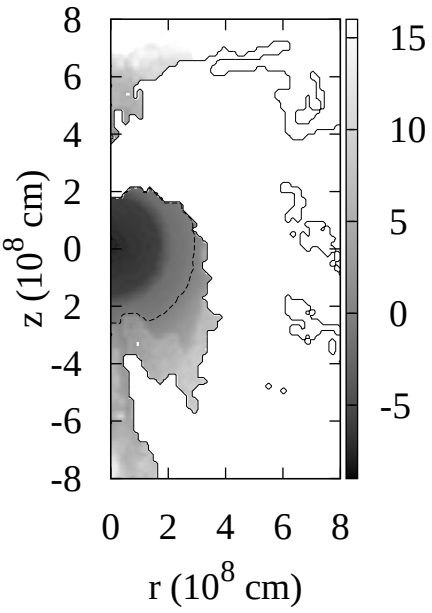

Figure 4.36: Y12 detonation: Effective reaction length compared to the density scale height with a contour of zero(dashed line) for the PDS version.. The solid line is the interface.

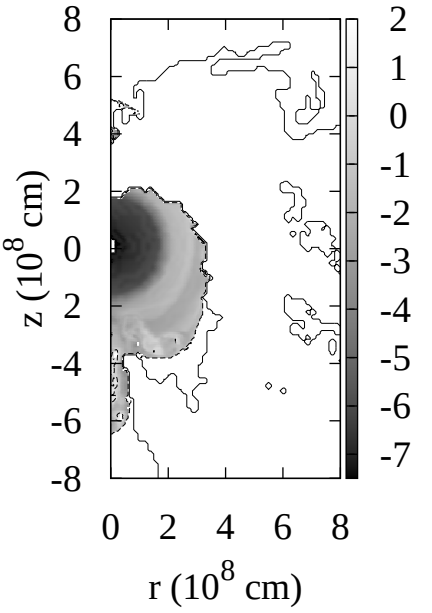

Figure 4.37: Y12 detonation: Effective reaction length compared to the density scale height with a contour of zero (dashed line) for the PDS version. The solid line is the interface.

(see chapter 2, figure 2.2). The shock is also travelling at the sound speed and may be too weak to compress and ignite the C-O. Furthermore, the time required for carbon to reignite at low densities is greater than the timescale of the explosion (Domínguez and Khokhlov 2011). These areas would also require a time-dependent analysis. When the detonation front reignites, it is initially unsteady and thus DSD theory here is not applicable. No conclusions can be made about this region without a more rigorous analysis and these regions are small compared to the overall solution. The entire wavefront is extinguished by 1.25 s (including the small detonation pockets) and remains so. Thus in this case, when curvature effects are accounted for, only the small high density central pocket of C-O can be detonated and outside this zone, the low density material will not be burnt. This may profoundly affect the viability of such low density SN Ia models.

Figure 4.34 summarises the solution branch regimes of the evolution. There is an O burning region due to being pathological, surrounded by a Si burning region as before, with C burning further out. There are two pockets of Si burning in the O burning just before the detonation reaches the burnt material. There is also a pocket of C burning within the O burning near z axis and two pockets of O burning within the C burning.

In terms of reaction lengths, the PDS model is only self-consistent in the central high density regions, but becomes increasingly inconsistent as the density drops (the reaction lengths reach over 15 orders of magnitude larger than the density scale height of the C-O region in the lowest densities, figure 4.36). For the DSD case, the driving reaction lengths mostly remain below the size of the C-O region (figure 4.37). There are some regions where the reaction lengths exceed the density scale height near the z-axis between $z = -4 \times 10^8$ and -6×10^8 cm. However, these localised regions are secondary in terms of mass burnt. These regions also require a time-dependent simulation. The DSD analysis shows that the scales which need resolving are very small indeed compared to the size of the star.

4.3 Summary

Several models of SN Ia using DSD have been re-evaluated by properly accounting for the effects of the front curvature on detonation waves. This takes into account curvature induced detonation failure and the location of the sonic point. The results predicted by DSD were

compared to the assumption of propagation at the planar detonation speed. Curvature effects are important at low densities but at high densities the effects are only marginal. In these low density regions the detonation travels slower than the planar speed and consequently the wavefront arrival times are longer. The detonation may also be extinguished. The driving zone lengths are also many orders of magnitude shorter than the planar detonation wave and more consistent than assuming planar detonation, as the region before the sonic point has influence on the front dynamics. The planar detonation wave can become greater than the density height scale in the outer regions of the star. There are also implications for the nucleosynthesis which are discussed in the final chapter.

These results question the validity of the models presented and investigated in this chapter. In Fink et al's model, due to the low density in the He, the detonation did not ignite until the curvature of the front was sufficiently small (or equivalently, the detonation kernel was sufficiently large). This may suggest detonation within the C-O core to be more likely or greater mass (but still sub-Chandrasekhar mass e.g. Case A) white dwarfs. The higher densities are less sensitive to curvature and therefore the ignition kernel could be smaller. Fink et al's (2010) focus of their paper was to see if low mass He shells could ignite and induce detonations in the C-O through compressional heating They investigated a variety of low density shells and found they successfully detonated the core. However, when their model 2 ignited in this work, the detonation was confined to a narrow region adjacent to the core and with speeds lower than its planar values. Therefore, in contrast to Fink et al's paper, and given the previous point about the ignition kernel, the compression of the core may not be sufficient to induce a detonation and thus, low mass He shells may not induce detonations in the core. In the case of Plewa's (2007) model, due to the expansion of the star which resulted in lower densities, the majority of the material did not detonate. It seems unlikely such a model would be a plausible candidate for a type Ia explosion. There would be an overabundance of C, O and especially He as the detonation does not reach the shell. It is clear that for any future models, the possible effects of curvature need to be taken into consideration.

Chapter 5

Boundary Value Problem Adaption for Curvature Dependent Speeds

5.1 Introduction

The level set method by Sethian (1999), discussed in chapter 3 and used in chapter 4, evolves a surface ψ moving under speed F according to the equation

$$\frac{\partial \psi}{\partial t} + F\,|\nabla \psi| = 0. \tag{5.1}$$

He calls this the initial value problem (IVP). As seen previously, this surface can have a speed described spatially by the function F_0 and also by a function of its curvature, $\alpha(\kappa)$, in the form $F = F_0 - \alpha(\kappa)$. This means the level set equation consists of two parts, the hyperbolic part $F_0\,|\nabla \psi|$ and the parabolic part $-\alpha(\kappa)\,|\nabla \psi|$. Sethian details how to solve this equation using upwinding with forward and backwards differences for the hyperbolic part. The parabolic part requires central differencing. Solving the level set equation and seeing where ψ changes sign, the wavefront arrival time (or burntable), t^b, can be found via interpolation in time between these two points.

Using DSD and the IVP method, the wavefront propagation of curvature dependent speeds in SN Ie was investigated through a subgrid model and discussed in the previous chapter. Low densities and negative curvature require the use of a small time step or smoothing of the speed function. The latter is undesirable for when a more quantitative assessment is desired. The

other alternative is to make the computation more efficient. Speeding up the IVP can be accomplished by using the narrow band method (Adalsteinsson and Sethian 1994; Sethian 1999). The ψ field consists of an infinite number of level curves. There is only one physical level curve within the surface of interest, representing the front location, usually (but not always) the $\psi = 0$ level curve. An alternative to calculating the values at $\psi_{i,j}^{n+1}$ for all nodes in the domain is to consider only those near and on the level set - a narrow band. When the level curve of interest is near the edge of the narrow band, the calculation must be paused and a new band built around the level curve of interest. A process known as re-initialisation. This can contribute to the error as it may perturb the front from its actual position. A suitable width for the narrow band also needs to be decided. Too large and the problem is nearly back to its original form. Too small, and the process of re-initialisation dominates the computations.

A boundary value problem (BVP) is also described by Sethian (1999) for when the speed only depends on F_0. To obtain the burn table this way, one solves the equation

$$F \left| \nabla t^b \right| = 1. \tag{5.2}$$

Upwinding and finite differences are used again with the term on the left hand side. This is because initially only the nodes located on the initial front position are correct (and equal to zero). The nodes directly adjacent to these will then use the nodes on the initial front to converge to their correct value. If the nodes on the initial front position do not align with the front, then the signed distance function is constructed and propagated in a small neighbourhood adjacent to the initial front location using the IVP to find these node values. Using the definitions of A, B, C and D from chapter 3 with ψ replaced by t^b to approximate the left hand size, this gives

$$F_{i,j} \left[\begin{array}{ccc} \max(A,0)^2 & + & \max(B,0)^2 \\ +\max(C,0)^2 & + & \max(D,0)^2 \end{array} \right]^{1/2} = 1. \tag{5.3}$$

This results in nonlinear equations for t^b at each node. An estimate is used for t^b (e.g. the signed distance function) and then iterated until converged. A better estimate will result in fewer iterations required to reach convergence. A node has converged when

$$\left| F_{i,j} \left| \nabla t^b_{i,j} \right| - 1 \right| \leq \text{tol}, \tag{5.4}$$

where tol is a specified tolerance. However, this formulation is only valid when the front speed does not depend on curvature. It has been noted that this equation, 5.2, is a steady state form of

$$\frac{\partial t^b}{\partial t} + F \left| \nabla t^b \right| = 1. \tag{5.5}$$

This is similar to the level set equation, 5.1, with a source term of 1.

The aim of this chapter is to investigate solving the above equation numerically for fronts propagating under curvature dependent speeds and to compare this with the level set method/IVP. The error and number of node updates will be investigated and compared. Although the narrow band method offers an improvement in speed for the IVP, the approach detailed here is relatively straightforward.

5.2 Numerical Implementation

The numerical implementation is identical to that of chapter 3 in the approximation of the time derivative and the second term. Note however, time here is pseudo time, where the solution is marching towards the steady state. The speed function is again broken up into a hyperbolic and parabolic part. Central differencing is used for the parabolic part. The only difference with the numerical stencil is the addition of a Δt term on the right hand side, arising from the source term. Overall the setup is very similar to the IVP, except there is also no need to find when the level curve of interest crosses a node as the crossing time is being solved directly and the value of $t^b_{i,j}$ at the next 'time step' is inserted back into the t^b array.

5.2.1 Initial Conditions

An initial guess is needed for t^b with the correct values on the initial front position. An easy way to do this is to simply use the distance function. Then as before for the initial value problem, for an ignition centred at (x_1, y_1) with initial radius r_0

$$t^b(x,y) = \sqrt{(x-x_1)^2 + (y-y_1)^2} - r_0. \tag{5.6}$$

As mentioned previously, nodes may not coincide with the initial front location. The nodes also require two known values in the x and y directions due to the second derivatives arising from the second order corrections. The IVP can be used until the required number of nodes (two layers) on and by the initial front are found. These nodes are then fixed and never updated.

5.2.2 Fast Marching Method

Sethian (1999) introduces the Fast Marching Method (FMM) for the BVP. There is a causality relationship between the nodes and the FMM makes use of it. Iterating on nodes far away from the initial front when information has yet to reach the surrounding nodes is inefficient. One therefore works through the domain in an ordered way, using this causality relationship. To understand this, suppose there is a small band of trial values adjacent to accepted values. This could be the initial front location, as that is known to be correct. The FMM is as follows:-

- Consider one node that is known, surrounded by four trial values called A, B, C and D. These four values are updated using the upwind known node.
- The minimum of these new four values is selected. Say A is the smallest.
- A is frozen, update its downwind trial value neighbours, using this value of A.
- Select the next smallest value, say D.
- Freeze D, update its downwind trial value neighbours, and so on.

When there is a curvature dependent term in the speed function, then information is used from all adjacent nodes due to central differencing. A node can not be simply iterated on numerous times, then forgotten and the computation moved onto the next node. An adaptation is made here as follows:-

- Initialise t^b according to the distance function as usual.

- Sort the values for $t^b > 0$ into an array of increasing order so that the first value is the smallest. Say A, B ...,.
- Operate on the smallest value, A, then move onto the next value, B.
- Operate on B. If B is now smaller than A, move B to A's position and A to B's position in the array.
- Now operate on B, the first element in this array, and repeat.

The node values are kept in order as the domain is iterated through.

5.3 Test Problems

5.3.1 Expanding Quarter Circle

The same test problem in chapter 3 by Aslam, Bdzil and Stewart (1996) of an expanding circle in a quarter plane with domain $0 \leq x \leq 1$ and $0 \leq y \leq 1$ is used. Reflective boundary conditions are along the x and y axes and outwards flow/non-reflecting at the other two boundaries. The initial front at $t = 0$ is at $r_0 = 0.2$. The same time step for each Δ is the same as in the IVP solution from chapter 3. The analytical solution is

$$t^b_{\text{exact}} = \sqrt{x^2 + y^2} - 0.2 + 0.1 \log_{10} \left(\frac{\sqrt{x^2 + y^2} - 0.1}{0.1} \right). \tag{5.7}$$

The error, E_1, is calculated by using the L_1 norm again, given by

$$E_1 = \sum_{i,\,j} \left| t^b - t^b_{\text{exact}} \right| \Delta^2. \tag{5.8}$$

The solutions are computed until all nodes satisfy

$$\left| F_0 \left| \nabla t^b_{i,j} \right| - \alpha \kappa_{i,j} \left| \nabla t^b_{i,j} \right| - 1 \right| \leq \text{tol}, \tag{5.9}$$

where the first $\left| \nabla t^b_{i,j} \right|$ is obtained through appropriate upwinding and $\kappa_{i,j} \left| \nabla t^b_{i,j} \right|$ through central differencing. Various E_1s were calculated for the Δs in chapter 3 and they can be seen again in table 5.1. This table also lists the number of node updates until the front has crossed every node on the domain.

Δ	E_1	# IVP node updates	CPU time (s)
1/40	1.14×10^{-3}	1 235 535	11
1/80	3.16×10^{-4}	17 373 528	149
1/160	8.70×10^{-5}	259 391 447	2 227
1/320	2.16×10^{-5}	4 003 348 932	34 308

Table 5.1: The error for various Δs with the number of node updates required and the CPU time for the expanding quarter circle from the IVP.

Δ	10^{-2}	10^{-3}	10^{-4}	10^{-5}
1/40	0.075	0.072	0.072	0.072
1/80	0.074	0.073	0.071	0.071
1/160	0.080	0.079	0.077	0.077
1/320	0.11	0.11	0.11	0.11

Table 5.2: $E_1^{\text{BVP}}/E_1^{\text{IVP}}$ for various Δs with different tols for the expanding quarter circle from the BVP adaptation.

Δ	10^{-2}	10^{-3}	10^{-4}	10^{-5}
1/40	0.66	0.76	0.80	0.89
1/80	0.65	0.67	0.74	0.80
1/160	0.63	0.64	0.69	0.73
1/320	0.61	0.62	0.65	0.68

Table 5.3: # BVP node updates / # IVP node updates for various Δs with different tols for the expanding quarter circle from the BVP adaptation.

Δ	10^{-2}	10^{-3}	10^{-4}	10^{-5}
1/40	0.19	0.21	0.22	0.25
1/80	0.19	0.19	0.21	0.23
1/160	0.18	0.18	0.20	0.21
1/320	0.18	0.18	0.19	0.20

Table 5.4: BVP CPU time / IVP CPU time for various Δs with different tols for the expanding quarter circle from the BVP adaptation.

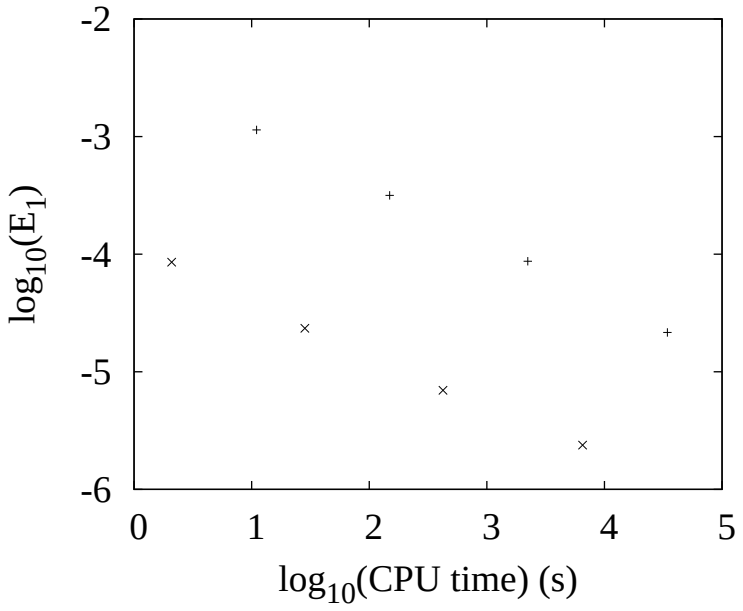

Figure 5.1: Error as a function of CPU time for the BVP adaptation (×) with tol = 10^{-2} and IVP (+) for the various Δs.

The results for the BVP adaptation are shown in tables 5.2, 5.3 and 5.4. Table 5.2 shows the ratio of the E_1 error between the BVP adaptation and IVP method for various Δs and tols. As the value of tol is decreased, the error becomes smaller for a fixed Δ, eventually reaching a value for which it does not change significantly. For larger values of Δ, smaller tols do not have much of an effect on the error, e.g. for $\Delta = 1/40$, the error does not change significantly for tol$\leq 10^{-3}$. When Δ is smaller, e.g. 1/320, then smaller tols affect the error, but again a value is reached for which the error no longer changes significantly. The error is always less than the IVP method The number of node updates is shown in table 5.3 by the number of BVP node updates divided by the number of IVP node updates. Smaller tol values increases the number of node updates required. The BVP adaptation is more efficient for smaller Δs. In addition to this, the CPU time in table 5.4 can be seen. The CPU time required is about one fifth of of the IVP method. This is also shown in figure 5.1 for both the IVP and BVP adaptation. Clearly the BVP adaptation is faster and with less error than the IVP method.

The speed of the BVP adaptation can be improved further by using a better initial guess than the distance function. A coarse grid with the distance function as the initial guess could be used, its values found, and then interpolated onto a finer grid. As the BVP adaptation

Δ	#BVP updates / # IVP updates	BVP CPU time / IVP CPU time
1/40	0.62	0.19
1/80	0.54	0.17
1/160	0.14	0.05

Table 5.5: Starting Δs for the $\Delta = 1/320$ problem with tol= 10^{-4} and the ratio of #BVP updates / #IVP updates.

is more efficient for finer resolution, how it can be made more efficient for $\Delta = 1/320$ is investigated next. A value of tol = 10^{-2} is used as the error is only slightly more than its converged (to two significant figures) version. The initial guesses to be used are the solutions with values $\Delta = 1/40$, 1/80, and 1/160. The results for these are found and then interpolated using bilinear interpolation onto a grid with $\Delta = 1/320$. The IVP method is used again to find the nodes in a region adjacent to the initial front position. The total number of node updates will consist of the sum for both the larger and smaller Δs.

The results are shown in table 5.5. All starting Δs show a considerable reduction in the number of node updates required. For the largest starting Δ, the time required is one fifth of the IVP time and this is similar in time to just using the distance function as an initial guess. Decreasing the starting Δ results in less node updates being needed and a reduction in the CPU time. When the starting Δ is half of the final value, the solution takes just 5 per cent of the IVP CPU time to be calculated.

5.3.2 Two Expanding and Merging Circles

One of the advantages with these methods of front propagation is the ease with which topological change of the front is handled. The next test case to demonstrate this is of two merging circles. There will be discontinuities and this test shows that, like the IVP, this adaptation can solve problems with initial discontinuities. One of the circles is centred at the origin, the other at $(1, 0)$. The left, right and bottom boundaries use reflective boundary conditions and the top boundary uses non-reflecting/outwards flow. For two circles located at (x_1, y_1) and (x_2, y_2), the initial guess for the distance function, given by

$$t^b(x, y) = \min\left(\sqrt{(x - x_1)^2 + (y - y_1)^2} - r_0, \quad \sqrt{(x - x_2)^2 - (y - y_1)^2} - r_0\right). \tag{5.10}$$

The same speed function $F = 1 - 0.1\kappa$ is used again. No analytical solution exists for this test due to the smoothing of the discontinuity along $x = 0.5$. Instead the BVP adaptation is compared to a higher resolution IVP solution ($\Delta = 1/640$).

A value of tol $= 10^{-2}$ is used in the BVP adaptation with $\Delta = 1/40$. The results for $\Delta = 1/40$ are shown in figures 5.2 for the BVP adaptation and the lower resolution IVP solution in 5.3. The error is most noticeable with both low resolution cases where the two expanding circles meet along $x = 0.5$ and both the BVP adaptation and IVP have this problem. Both solutions are in good agreement away from this point. Finally a solution is computed using an initial $\Delta = 1/160$ and then interpolated onto a grid for $\Delta = 1/320$. The solution is also computed using the IVP for comparison in the number of node updates. The IVP requires 2 808 588 537 node updates and the BVP adaptation requires 610 260 384 updates, i.e. the BVP adaptation only requires 22 per cent of the updates the IVP needs and the result is shown in figure 5.4. Both the higher resolution IVP and BVP adaptation solution are indistinguishable from one another.

5.4 Summary

The narrow band method is designed to increase the computational efficiency of the IVP. This is however relatively more complicated compared to the new method investigated and discussed here. Adalsteinsson and Sethian (1994) discuss the narrow band method in detail and its technical implementation. The level curve of interest must remain inside the band (or tube as they call it). Derivatives also need attention at the edge points of the tube. There can be stability problems and in that case the time step must be undone. There must also be an algorithm to detect when the level curve of interest is near the edge.

The BVP in its original form does not include speed functions that can have a curvature dependent component. In the case of speed functions which are just a function of space, one solves this method by iterating nonlinear equations for the numerical solution. What has been described here is an alternative way to solve this BVP. This also allows for curvature dependent speeds. It's implementation is very similar to the IVP but with the addition of a source term and solving directly for the burn table. The causality condition of the values at the nodes enables the computation to be more efficient in a straightforward way compared to

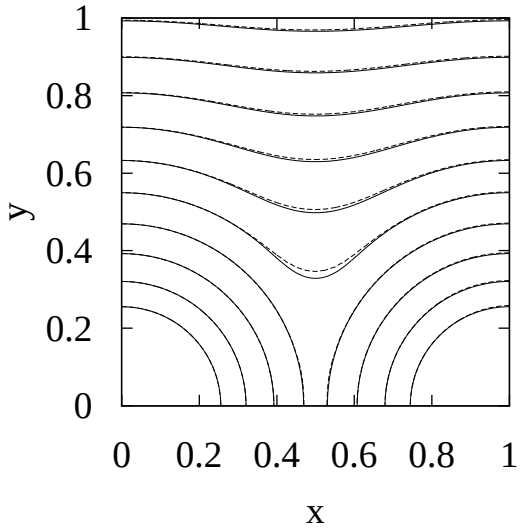

Figure 5.2: High resolution ($\Delta = 1/640$) IVP solution (solid lines) and BVP adaptation with $\Delta = 1/40$ (dashed lines) at t =0.1, 0.2, 0.3, 0.4, 0.5, 0.6, 0.7, 0.8, 0.9 and 1.0 s.

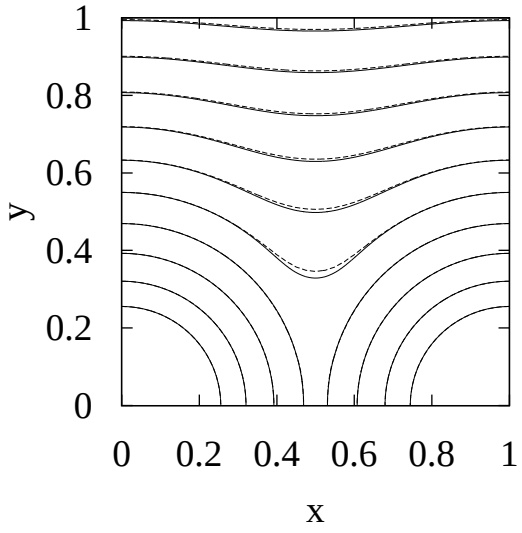

Figure 5.3: High resolution ($\Delta = 1/640$) IVP solution (solid lines) and lower resolution IVP solution with $\Delta = 1/40$ (dashed lines) at t =0.1, 0.2, 0.3, 0.4, 0.5, 0.6, 0.7, 0.8, 0.9 and 1.0 s.

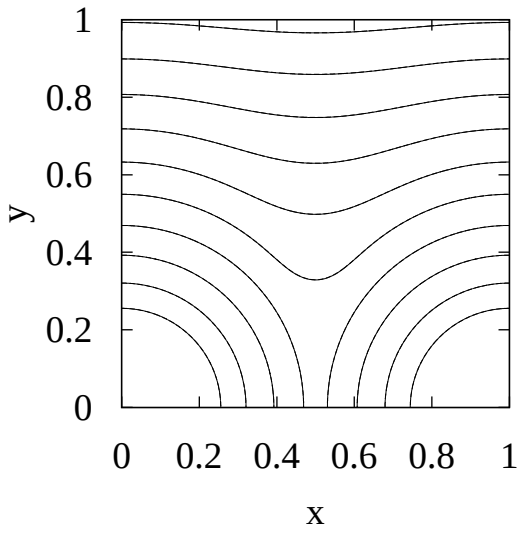

Figure 5.4: High resolution ($\Delta = 1/640$) IVP solution (solid lines) and BVP adaptation solution with a final $\Delta = 1/320$ (dashed lines) at t =0.1, 0.2, 0.3, 0.4, 0.5, 0.6, 0.7, 0.8, 0.9 and 1.0 s. The two solutions have good agreement.

the narrow band method. They are simply arranged in increasing order and then operated on with the ordering being kept as one works through the domain. Both the error and the number of node updates required was below that required for the IVP. The efficiency can be further improved by first computing the solution on a coarse grid, then interpolating this result onto a finer grid as an improved initial guess. This was found to dramatically reduce the number of computations needed for a fine grid.

This work is promising in allowing fronts to be tracked at a reduced cost with a relatively straightforward implementation. Of course more tests and analyses are required to ensure its robustness. Seeing if it can cope with complex speed functions and geometries such as the results presented in the previous chapter would aid this. Taking equation 5.5 in one dimension and setting $u = \partial t^b/\partial x$, similar to chapter 3, then it is obvious the same hyperbolic equation with a viscous term is obtained and thus complex topological change of the front should be handled easily through the link between viscous hyperbolic conservation laws and Hamilton-Jacobi equations (Sethian 1999; Osher and Fedkiw 2003). It is therefore expected for future tests with nonlinear speed functions and complex geometries, this BVP adaptation should be sucessful in both producing an accurate result and in less time. A typical detonation test

problem is that of the rate stick problem. The detonation propagates down a region confined on two opposite sides by an inert solid. The interaction of the front with the inert regions can have angled boundary conditions. Using Aslam, Bdzil and Stewart's (1996) approach, a rate stick problem has been solved with the BVP adaptation (Sharpe 2012). Thus this extension of the IVP carries over easily into the BVP adaptation.

It is possible that even more of a reduction in the number of node updates may be obtained. Throughout this chapter, updates have been performed on all nodes, except for those in a small neighbourhood on or adjacent to, the initial front position. If a node has satisfied the convergence criteria (equation 5.9), then it may be possible to no longer update it. This was attempted. However, it lead to unsatisfactory results. The error of a node oscillates for small tolerances with a decreasing trend, then eventually becomes stable and unchanging. Thus a converged node may not actually be converged based only upon equation 5.9. Nodes may have an error smaller than the specified tolerance on one time step, but not on the next. An initial attempt to overcome this was to only let a node be converged if its upwind neighbours were also converged. Unfortunately this did not solve the problem.

Another possible way in which the efficiency may be improved is using a narrow band similar to the IVP. In the original BVP formulation, as discussed, one can use the FMM. The narrow band here is just the immediate neighbours. This has been implemented to some degree in the adaptation, by working through the nodes in order as due to the addition of the curvature term, nodes have some dependence downwind. A narrow band a few nodes in width could be chosen. As nodes are converged, this narrow band of nodes to operate on moves outwards from the initial front position. Then the causality relationship of the nodes is taken into account and wasted computations on converged nodes are no longer performed. As previously discussed, in the IVP, the narrow band approach is relatively complicated and has its associated problems. However, such problems should not be present if applied here. There is no front to reinitialise and there is no need to take care with the edges of the narrow band due to boundary conditions and edge detection. If the convergence issue can be solved, along with more appropriate tests and a narrow band implementation, then this method is an improved alternative to the IVP.

Chapter 6

Conclusion

Modelling supernovae is a complicated task. The complex nature of the physics along with the high degree of assumptions in order to simplify models to make calculations feasible can lead to different results. There are many research areas within supernovae research. This ranges from how the progenitor is formed, how does it then evolve further to a state where it may explode, to the question of ignition (e.g. hot spots, their size, number, location). Even then, there is the question of whether it is a detonation, a deflagration or a combination of both, i.e. does a DDT occur. In the case of a DDT, there is uncertainty to the physics behind it. The observations e.g. light curves give the constraints on which a successful model must satisfy. Near maximum light there are bands corresponding to intermediate mass elements such as Si, but detonations seem unable to produce these in relevant abundances. However, they do give the correct energy and expansion speeds of the ejecta. Conversely, deflagrations give good intermediate mass element production but then the expansion speeds and energy are too low. Combining therefore both deflagrations and detonations into the delayed detonation model seems to give the best agreement.

Much of this research was originally for one-dimensional spherically symmetrical geometries. The increase in computing power has led to models being investigated in two and three dimensions, e.g. Wiggins and Falle (1997). The ignition has been treated as a point rather than a thin layer around the star which can lead to different results such as cusp formation. Variations on the detonation model where an inert shock passes through the core whilst a detonation consumes the He (Fink et al. 2010) have also been investigated to see if such models can help improve the argument for detonations. However, to date, the effects of curvature

have been overlooked. If pure detonation models are ruled out due to lack of intermediate mass element production, then including the effects of curvature could strengthen the case for detonations, especially pure detonation. Wheeler and Harkness (1990) realised that a 'dampening mechanism' would aid the case for detonations.

In this thesis detonation theory was discussed generally and how curvature affects ('dampens') the speeds. Detonations were then discussed in the context of SNe Ia due to Sharpe's (2001) work on obtaining the $D_n - \kappa$ relations for C-O white dwarfs. These curves have speeds lower than the planar assumption for non-zero curvature and are also branched, corresponding to the location of the sonic point and effective reaction length. Thus, when the sonic point is not at the end of Si burning (as in the planar assumption), then there is the possibility for incomplete burning where Si, O or even C may be present in the ejecta. This evidently gives support to the detonation argument as then the speeds will still be high compared to a deflagration and also giving better intermediate mass element production from incomplete burning downstream of the sonic point.

The alternative and less consistent argument for detonations is for a detonation to propagate to low densities when the planar reaction lengths become comparable to the radius of the star and density scale height. This is not consistent as the assumption of a planar detonation means what happens in the reaction zone before the sonic point (located at the end of the reaction zone for non-pathological densities) can 'communicate' with the front. To travel at planar speeds requires complete burning since all the energy released must happen before the sonic point. However, by assuming incomplete burning of a planar wave, then one would expect speeds less than the CJ values. Detonations with non-zero curvature travel at lower speeds than their CJ versions with an internal sonic point. This (effective) reaction zone can also be orders of magnitude smaller then the CJ version and therefore the star's radius and density height scale.

The important effects of curvature are starting to be realised in the context of SNe Ia. Moore, Townsley and Bildsten (2013) investigated the flow in detail for He with curvature, also including the effects of gravity, something which has been ignored in this thesis. They found gravity can lead to the detonation front having greater curvature. Similar to the conclusions here, in their work there is unburned He and more intermediate mass elements. They also discuss the implications on how the slower He detonation could affect ignition in the core.

Although the speeds are fast enough for the interior shock to converge, they are uncertain as to whether it could ignite the core.

Full star simulations are computationally prohibitive due to the range of length scales involved. The C burning stage can be just a few centimeters, where as the radius of the star is over 10^8 cm. DSD, usually used in modelling terrestrial explosives, was applied in a new context to investigate the effects of curvature and curvature induced failure. DSD methods are shock frame intrinsic solutions of the reactive flow equations, based on calculations of the fully coupled hydrodynamic-nuclear burning equations. The detonation front speeds and reactive flow are essentially decoupled and then a suitable front tracking algorithm is required. Sethian's (1999) level set method was chosen due to handling speed functions which depend upon curvature in the form $F = F_0 + F_{\text{curvature}}$. The assumption made here in DSD is that the subsonic zone which is resolved, is quasi-steady and quasi-one-dimensional and slowly varying. This is checked by comparing the driving zone lengths to the density height scale of the star. When the two are comparable, then the slowly varying assumption no longer holds as the detonation needs to adjust itself to the local conditions rapidly, i.e. the time taken for a particle to traverse the driving zone is then comparable to the time scale of change for the detonation wave.

Sharpe (2001) used a reduced $\alpha-$network of 13 species linked by 27 reactions to calculate the $D_n - \kappa$ curves. This is sufficient for a qualitative assessment. To calculate a range of $D_n - \kappa$ curves with a full reaction network for various densities would be costly. Although once complete, they would not need to be computed again and would be useful for a future quantitative investigation. Messoudi, Vidal and Busegnies (2007) calculated one curve for a network of 331 species and 3262 reactions for a density of 5×10^6 g cm^{-3} and compared this to a reduced network of 13 species and 18 reactions. The C branch extinction curvature is an order of magnitude higher and the detonation speeds are higher. The difference between a full and reduced network would be greater at low densities since at higher densities, the effects of curvature are not as important as the speed only drops a few per cent. Even at low densities however, if the extinction curvatures were increased an order of magnitude, low density regions would still fail to detonate. The differences would still be greatest between taking into account curvature and assuming planar propagation.

The results from the DSD were compared to those of the assumption of propagation at

the planar detonation speed. The effects of curvature are important at low densities, but only marginal at higher densities. In the low density regions the detonation travels slower than the planar speed. This can significantly affect the wavefont arrival times and the driving zone lengths. For low enough densities, the shock front decays rapidly to an inert acoustic wave and the detonation front is extinguished. When the density is low, the planar detonation wave driving zone becomes orders of magnitude greater than the density height scale (and the size of the star). Previously it was this feature which was used to aid detonations in producing intermediate mass elements but as outlined this is inconsistent. Taking into account curvature, typically the driving zone lengths are found to be smaller than the density height scale. Although in Case A and Y12 the driving zone lengths were found to be greater than the density height scale in some regions, these are small. Comparing to the density scale height is a consistency check on the leading order DSD solutions. If large regions of a star are found to have driving reaction zones comparable to this characteristic value, then even smaller scales need to be resolved. Unfortunately very high resolution is needed for results that are qualitatively correct (Kapila et al. 2007).

A more quantitative prediction of these results requires the detonation subgrid model to be coupled to the reactive hydrodynamic evolution. The density, temperature etc. behind the wavefront can then be calculated, therefore allowing radiation transport codes to be used to look at the resulting light curves (Hoeflich and Khokhlov 1996; Nugent et al. 1997). However, a number of conclusions can be made from the location of the sonic point and the detonation being extinguished with regards to the nucleosynthesis and intermediate mass element production. For low density regions, the sonic point will be near the end of C or O burning. As the overall reaction length is comparable to the radius of the star, the Si burning region behind the sonic point will be incomplete. Furthermore this supersonic Si burning region is longer for curved detonations than in their planar versions (Sharpe 2001). The thermonuclear reactions are highly sensitive on temperature (Fryxell et al. 1989), therefore the shock speeds and thus temperatures are lower in their curved versions. Consequently more Si would be expected compared to the planar assumption. If the detonation speed drops low enough due to curvature, then $\alpha-$freeze-out could occur (Fryxell et al. 1989). Sufficient intermediate mass elements may also be produced for higher density sub-Chandrasekhar models than previously considered. Sub-Chandrasekhar white dwarfs have a problem with high velocity Ni

and He in the outer ejecta (Nugent et al. 1997). The lower speeds and decreased iron group element production of curved detonations could help improve the case for sub-Chandrasekhar models. The most obvious effect of curvature is the detonation failing in the outer He density regions or the shell, resulting in unburned C-O and He fuel. In models where the whole star detonates, this could change the predictions of the nucleosynthesis. Observations would also indicate more C and/or He in the spectra. Although C is not typically observed in the spectra, Folatelli et al. (2012) have observed unburnt material, indicating that some SNe Ia may not detonate completely. It is important to note as well, the models presented here, when curvature is taken into account, may not be suitable progenitors for SNe Ia. In the more extreme case of the Y12 model, the majority of the star failed to detonate due to the expanded material and hence lower densities. Such considerations should be taken into account when considering suitable progenitors in the future.

A detonation can have a cellular structure (Fickett and Davis 1979). The boundaries of these cells change with time and propagate transversely. The front of the detonation (the leading shock) is intersected by some of the cell boundaries, causing it to wrinkle. These cells lead to inhomogeneous pressure, temperatures etc. behind the front. A detonation wave in C-O, which involves a C, O and Si burning stage, has three levels of detonation cells associated with each burning stage (Gamezo et al. 1999). The Si cells can become larger than the white dwarf below densities of 10^7 g cm^{-3}. There can also be unreacted pockets. The spectra can be affected due to not only unreacted pockets, but overreacted pockets as well. As the burning lengths are not resolved finely enough, these cells do not appear in full star simulations, giving different predictions to the nucleosynthesis. This again necessitates a subgrid model which can capture these effects, especially time dependence, and this requires higher order DSD.

References

Adalsteinsson D., Sethian J. A., 1994, *A Fast Level Set Method for Propagating Interfaces*, Journal of Computational Physics, 118, p269-277.

Arnett W. D., 1969, *A Possible Model of Supernovae: Detonation of* ^{12}C, Astrophysics and Space Science, 5, 2, p180-212.

Arnett D., Livne E., 1994a, *The Delayed-detonation Model of a Type Ia Supernovae. I. The Deflagration Phase*, The Astrophysical Journal, 427, p315-329.

Arnett D., Livne E., 1994b, *The Delayed-detonation Model of a Type Ia Supernovae. II. The Detonation Phase*, The Astrophysical Journal, 427, p330-341.

Arnett D., 1996, *Supernovae and Nucleosynthesis: An Investigation of the History of Matter, from the Big Bang to the Present,* Princeton University Press.

Aslam T. D., Bdzil J. B., Stewart D. S, 1996, *Level Set Methods Applied to Modeling Detonation Shock Dynamics*, Journal of Computational Physics, 126, p390-409.

Aslam T. D., Bdzil J. B., Hill L. G., 1998, *Extensions to DSD Theory: Analysis of PBX 9502 Rate Stick Data*, Eleventh International Detonation Symposium

Baade W., Zwicky F., 1934, *Remarks on Super-Novae and Cosmic Rays*, Physical Review, 46, p76-77.

Bdzil J. B., Aslam T. D., 2000, *Detonation Front Models: Theories and Methods*, Los Alamos National Laboratory, LA-UR-00-942.

Bdzil J. B., Stewart D. S., 2007, *The Dynamics of Detonation in Explosive Systems*, Annual Review of Fluid Mechanics, 39, p263-292.

Benz W., 1997, *Three-dimensional Simulations of Core Ignition in Sub-Chandrasekhar Mass Models*, Thermonuclear Supernovae, NATO ASI Series, Series C: Mathematical and Physical Sciences, Vol. 487, p457-474.

Ciaraldi-Schoolman F., Schmidt W., Niemeyer J. C., Roepke F. K., Hillebrandt W., 2009, *Turbulence in a Three-dimensional Deflagration Model for Type Ia Supernovae. I. Scaling Properties*, The Astrophysical Journal, 696, p1491-1497.

Colgate S. A., McKee C., 1969, *Early Supernova Luminosity*, The Astrophysical Journal, 157, p623-643

Domínguez I., Khokhlov A., 2011, *Incomplete Carbon-Oxygen Detonation in Type Ia Supernovae,* The Astrophysical Journal, 730, 87.

Dunkley S. D., Sharpe G. J., Falle S. A. E. G., *Detonation Shock Dynamics of Type Ia Supernovae*, Monthly Notices of the Royal Astronomical Society, 431, p3429-3443.

Fickett W., Davis W. C., 1979, *Detonation*, University of California Press, Berkeley and Los Angeles.

Filippenko A. V., 1997, *Type Ia Supernovae: Observation Overview*, Thermonuclear Supernovae, NATO ASI Series, Series C: Mathematical and Physical Sciences, Vol. 487, p1-32.

Fink M., Roepke F. K., Hillebrandt W., Seitenzahl I. R., Sim S. A., Kromer M., 2010, *Double-detonation Sub-Chandrasekhar Supernovae: Can Minimum Helium Shell Masses Detonate the Core?,* Astronomy & Astrophysics, 514, A53.

Fink M., 2011, *Model 2 data*, email.

Folatelli G., Phillips M. M., Morrell N., Tanaka M., Maeda K., Nomoto K., Stritzinger M., Burns C. R., Hamuy M., Mazzali P., Boldt. L., Campillay A., Contreras C., González S., Roth M., Salgado F., Freedman W. L., Madore B. F., Persson S. E., Suntzeff N. B., 2012, *Unburned Material in the Ejecta of Type Ia Supernovae*, The Astrophysical Journal, 745, 74.

Fryxell B. A., Mueller E., Arnett D. A., 1989, Technical Report, Hydrodynamics and Nuclear Burning, Max-Planck Institute for Physics and Astrophysics, Garching.

Gamezo V. N., Wheeler J. C., Khokhlov A. M., Oran E. S., 1999, *Multilevel Structure of Cellular Detonations in Type Ia Supernova*e, The Astrophysical Journal, 512, p827-842.

Gamezo V. N., Khokhlov A. M., Oran E. S., Chtchelkanova A. Y., Rosenberg R. O., 2003, *Thermonuclear Supernovae: Simulations of the Deflagration Stage and Their Implications*, Science 299, p77-81.

Garavini G., Folatelli G., Nobili S., Aldering G., Amanullah R., Antilogus P., Astier P., Blanc G., Bronder T., Burns M. S., Conley A., Deustua S. E., Doi M., Fabbro S., Fadeyev V., Gibbons R., Goldhaber G., Goobar A., Groom D. E., Hook I., Howell D. A., Kashikawa N., Kim A. G., Kowalski M., Kuznetsova N., Lee B. C., Lidman C., Mendex J., Morokuma T., Motohara K., Nugent P. E., Pain R., Perlmutter S., Quimby R., Raux J., Regnault N., Ruiz-Lapuente P., Sainton G., Schahmaneche K., Smith E., Spadafora A. L., Stanishev V., Thomas R. C., Walton N. A., Wang L., Wood-Vasey W. M., Yasuda N., 2007, *Quantitative Comparison Between Type Ia Supernova Spectra at Low and High Redshifts: A Case Study*, Astronomy and Astrophysics, 470, p411-424.

Garcia-Senz D., Woosley S. E., 1995, *Type Ia Supernovae: The Flame is Born*, The Astrophysical Journal, 454, p895-900.

Hillebrandt W., Niemeyer J. C., 2000, *Type Ia Supernova Explosion Models*, Annual Review of Astronomy and Astrophysics, 38, p191-230.

Hodgson A., 2013, *Discussion on the initial detonation front radius and level set initialisation,* email.

Hoeflich P., Khokhlov A. M., 1996, *Explosion Models for Type Ia Supernovae: A Comparison with Observed Light Curves, Distances,* H_0, *and* q_0, The Astrophysical Journal, 457, p500-528.

Hoyle F., Fowler W. A., 1960, *Nucleosynthesis in Supernovae*, The Astrophysical Journal, 132, p565-590.

Jeffery D., Sutherland P., 1985, *Deflagration of White Dwarfs as a Model for Type-I Supernovae*, Astrophysics and Space Science, 109, p277-285.

Kapila A. K., Schwendeman D. W., Bdzil J. B., Henshaw W. D., *A Study of Detonation Diffraction in the Ignition-and-growth Model*, Combustion Theory and Modelling, 11, p781-822.

Kepler S. O., Kleinman S. J., Nitta A., Koester D., Castanheria B. G., Giovannini O., Costa A. F. M., Althaus L., 2007, *White Dwarf Mass Distribution in the SDSS*, Monthly Notices of the Royal Astronomical Society, 375, p1315-1324.

Khokhlov A. M., 1989, *The Structure of Detonation Waves in Supernovae*, Monthly Notices of the Royal Astronomical Society, 239, p785-808.

Khokhlov A. M., 1991, *Delayed Detonation Model for Type Ia Supernovae*, Astronomy and Astrophysics, 245, p114-128.

Khokhlov A. M., Mueller E., Hoeflich P., 1993, *Light Curves of Type Ia Supernova Models with Different Explosion Mechanisms*, Astronomy and Astrophysics, 270, p223-248.

Khokhlov A. M., 1995, *Propagation of Turbulent Flames in Supernovae*, The Astrophysical Journal, 449, p695-713.

Laughlin G., Bodenheimer P., Adams F. C., 1997, *The End of the Main Sequence*, The Astrophysical Journal, 482, p420-432.

Lee J. H. S., 1977, *Initiation of Gaseous Detonation*, Annual Review of Physical Chemistry, 28, p75-104.

Livne E., Glasner A. S., 1991, *Numerical Simulations of Off-center Detonations in Helium Shells*, The Astrophysical Journal, 370, p272-281.

Messoudi A. E., Vidal P., Busegnies Y., 2007, *Low-velocity Regimes of Thermonuclear Detonations in Type-Ia Supernovae*, Comptes Rendus Mecanique, 335, p768-774.

Minkowski R., 1940, *Spectra of the Supernova in NGC 4725*, Publications of the Astronomical Society of the Pacific, 52, 307, p206.

Minkowski R., 1941, *Spectra of Supernovae*, Publications of the Astronomical Society of the Pacific, 53, 314, p224-225.

Moore K., Townsley D. M., Bildsten L., 2013, *The Effects of Curvature and Expansion on Helium Detonations on White Dwarf Surfaces*, The Astrophysical Journal, 776, 97.

Nieyemer J. C., Woosley S. E., 1997, *The Thermonuclear Explosion of Chandrasekhar Mass White Dwarfs*, The Astrophysical Journal, 475, p740-753.

Nomoto K., Sugimoto D., Neo S., 1976, *Carbon Deflagration Supernova, An Alternative to Carbon Detonation*, Astrophysics and Space Science, 39, L37-L42.

Nomoto K., 1982a, *Accreting White Dwarf Models for Type I Supernovae. I. Presupernova Evolution and Triggering Mechanisms*, The Astrophysical Journal, 253, p798-810.

Nomoto K., 1982b, *Accreting White Dwarf Models for Type I Supernovae. II. Off-center Detonation Supernovae*, The Astrophysical Journal, 257, p780-p792.

Nomoto K., Thielemann F. K., Yokoi K., 1984, *Accreting White Dwarf Models for Type I Supernovae. III. Carbon Deflagration Supernovae*, The Astrophysical Journal, 286, p644-658.

Nomoto K., Iben I. J., 1985, *Carbon Ignition in a Rapidly Accreting Degenerate Dwarf: A Clue to the Nature of the Merging Process in Close Binaries*, The Astrophysical Journal, 297, p531-537.

Nonaka A., Aspden A. J., Zingale M., Almgren A. S., Bell J. B., Woosley S. E., 2012, *High-Resolution Simulations of Convection Preceding Ignition in Type Ia Supernovae using Adaptive Mesh Refinement*, The Astrophysical Journal, 745, p73-95.

Nugent P., Baron E., Branch D., Fisher A., Hauschildt P. H., 1997, *Synthetic Spectra of Hydrodynamic Models of Type Ia Supernovae*, The Astrophysical Journal, 485, p812-819.

Nugent P. E., Sullivan M., Cenko S. B., Thomas R. C., Kasen D., Howell D. A., Bersier D., Bloom J. S., Kulkarni S. R., Kandrashoff M. T., Filippenko A. V., Silverman J. M., Marcy G. W., Howard A. W., Isaacson H. T., Maguire K., Suzuki N., Tarlton J. E., Pan Y., Bildsten L., Fulton B. J., Parrent J. T., Sand D., Podsiadlowski P., Bianco F. B., Dilday B., Graham M. L., Lyman J., James P., Kasliwal M. M., Law N. M., Quimby R. M., Hook I. M., Walker E. S., Mazzali P., Pian E., Ofek E. O., Gal-Yam A., Poznanski D., 2011, *Supernova SN 2011fe from an Exploding Carbon-Oxygen White Dwarf Star*, Nature, 480, p344-347.

Osher S., Sethian J. A., 1988, *Fronts Propagating with Curvature Dependent Speed: Algorithms Based on Hamilton-Jacobi Formulations*, Journal of Computational Physics, 79, p12-49.

Osher S., Fedkiw R., 2003, *Level Set Methods and Dynamic Implicit Surfaces,* Applied Mathematical Sciences, 153, Springer-Verlag New York Inc.

Paczyński B., 1972, *Carbon Ignition in Degenerate Stellar Cores*, Astrophysical Letters, 11, p53-55.

Piro A. L., Chang P., 2008, *Convection during the Late Stages of Simmering in Type Ia Supernovae*, The Astrophysical Journal, 678, p1158-1164.

Plewa T., 2007, *Detonating Failed Deflagration Model of Thermonuclear Supernovae. I. Explosion Dynamics*, The Astrophysical Journal, 657, p942-960.

Plewa T., 2012, *Y12 model data*, email.

Riess A. G., Filippenko A. V., Challis P., Clocchiatti A., Diercks A., Garnavich P. M., Gilliland R. L., Hogan C. J., Jha S., Kirshner R. P., Leibundgut B., Phillips M. M., Reiss D., Schmidt B. P., Schommer R. A., Smith R. C., Spyromilio J., Stubbs C., Suntzeff N. B., Tonry J., 1998, *Observational Evidence from Supernovae for an Accelerating Universe and a Cosmological Constant*, The Astronomical Journal, 116, p1009-1038.

Riess A. G., Filippenko A. V., Li W., Treffers R. R., Schmidt B. P., Qiu Y., Hu J., Armstrong M., Faranda C., Thouvenot E., Buil C., 1999, *The Rise Time of Nearby Type Ia Supernovae*, The Astronomical Journal, 118, p2675-2688.

Roepke F. K., Hillebrandt W., Schmidt W., Niemeyer J. C., Blinnikov S. I., Mazzali P. A., 2007, *A Three-dimensional Deflagration Model for Type Ia Supernovae Compared with Observations*, The Astrophysical Journal, 668, p1132-1139.

Roepke F. K., Woosley S. E., Hillebrandt W., 2007, *Off-center Ignition in Type Ia Supernovae. I. Initial Evolution and Implications for Delayed Detonation*, The Astrophysical Journal, 660, p1344-1356.

Ruiter A. J., Belczynski K., Fryer C., 2009, *Rates and Delay Times of Type Ia Supernovae*, The Astrophysical Journal, 699, p2026-2036.

Seitenzahl I. R., Meakin C. A., Townsley D. M., Lamb D. Q., Truran J. W., 2009, *Spontaneous Initiation of Detonations in White Dwarf Environments: Determination of Critical Sizes*, The Astrophysical Journal, 696, p515-527.

Sethian J. A., 1999, *Level Set Methods and Fast Marching Methods: Evolving Interfaces in Computational Geometry, Fluid Mechanics, Computer Vision, and Materials Science,* Cambridge University Press.

Sharp D. H., 1984, *An Overview of Rayleigh-Taylor Instability*, Physica D, 12, p3-18.

Sharpe G. J., 1999, *The Structure of Steady Detonation Waves in Type Ia Supernovae: Pathological Detonations in C-O Cores*, Monthly Notices of the Royal Astronomical Society, 310, p1039-1052.

Sharpe G. J., 2000a, *The Effect of Curvature on Pathological Detonations*, Combustion and Flame, 123, p68-81.

Sharpe G. J., 2000b, *The Structure of Planar and Curved Detonation Waves with Reversible Reactions*, Physics of Fluids, 12, p3007-3020.

Sharpe G. J., 2001, *The Effect of Curvature on Detonation Waves in Type Ia Supernova*, Monthly Notices of the Royal Astronomical Society, 322, p614-624.

Sharpe G. J., Braithwaite M., 2005, *Steady Non-ideal Detonations in Cylindrical Sticks of Explosives,* Journal of Engineering Mathematics, 53, p39-58.

Sharpe G. J., 2012, *Rate stick problem with the BVP adaptation solved in Matlab*, email.

Sim S. A., Roepke F. K., Hillebrandt W., Kromer M., Pakmor R., Fink M., Ruiter A. J., Seitenzahl I. R., 2010, *Detonations in Sub-Chandrasekhar-Mass C+O White Dwarfs,* The Astrophysical Journal Letters, 714, L52-L57.

Stehle M., Mazzali P. A., Benetti S., Hillebrandt W., 2005, *Abundance Stratification in Type Ia Supernovae - I. The case of SN 2002bo*, Monthly Notices of the Royal Astronomical Society, 360, p1231-1243.

Stewart D. S, 1998, *The Shock Dynamics of Multidimensional Condensed and Gas-phase Detonations*, Twenty-Seventh Symposium (International) on Combustion, The Combustion Institute, p2189-2205.

Stewart D. S, Yao J., 1998, *The Normal Detonation Shock Velocity-Curvature Relationship for Materials with Nonideal Equation of State and Multiple Turning Points*, Combustion and Flame, 113, p224-235.

Stritzinger M., Leibundgut B., Walch S., Contardo G., 2006, *Constraints on the Progenitor Systems of Type Ia Supernovae*, Astronomy and Astrophysics, 450, p241-251.

Timmes F. X., Arnett D., 1999, *The Accuracy, Consistency, and Speed of Five Equations of State for Stellar Hydrodynamics*, The Astrophysical Journal Supplement Series, 125, p277-294.

Townsley D. M., Jackson A. P., Calder A. C., Chamulak D. A., Brown E. F., Timmes F. X., 2009, *Evaluating Systematic Dependencies of Type Ia Supernovae: The Influence of Progenitor Ne Content on Dynamics*, The Astrophysical Journal, 701, 1582-1601.

Tutukov A. V., Yungel'son L. R., 1992, *Degenerate Dwarfs in Binary Systems*, Soviet Astronomy, 36, p266-274.

Webbink R. F., 1984, *Double White Dwarfs as Progenitors of R Coronae Borealis Stars and Type I Supernovae*, The Astrophysical Journal, 277, p355-360.

Wheeler J. C., Harkness R. P., 1990, *Type I Supernovae*, Reports on Progress in Physics, 53, 12, p1467-1557.

Woosley S. E., Weaver T. A., 1986, *The Physics of Supernova Explosions*, Annual Review of Astronomy and Astrophysics, 24, p205-253.

Woosley S. E., Weaver T. A., 1994, *Sub-Chandrasekhar Mass Models for Type Ia Supernovae*, The Astrophysical Journal, 423, p371-379.

Woosley S. E., 2007, *Type Ia Supernovae: Burning and Detonation in the Distributed Regime*, The Astrophysical Journal, 668, p1109-1117.

Wiggins D. J. R., 1993, *The Propagation of Nuclear Detonation Waves in Type I Supernovae*, Ph.D. thesis, Department of Applied Mathematical Studies, University of Leeds, UK.

Wiggins D. J. R., Falle S. A. E. G., 1997, *Two-dimensional Detonation Waves in Type Ia Supernovae*, Monthly Notices of the Royal Astronomical Society, 287, 3, p575-582.

Yao J., Stewart D. S., 1996, *On the Dynamics of Multi-dimensional Detonation*, Journal of Fluid Mechanics, 309, p225-275.

Zwicky F., 1938, *On Collapsed Neutron Stars*, The Astrophysical Journal, 88, p522-525.

Zwicky F., 1939, *On the Theory and Observation of Highly Collapsed Stars*, Physical Review, 55, p726-743.